Development of an Electrostatic Ion Beam Trap for Laser Spectroscopy of
Short-lived Radionuclides

I n a u g u r a l d i s s e r t a t i o n

zur

Erlangung des akademischen Grades eines

Doktors der Naturwissenschaften (Dr. rer. nat.)

der

Mathematisch-Naturwissenschaftlichen Fakultät

der

Universität Greifswald

vorgelegt von

Varvara Lagaki

geboren am 08.04.1990

in Athens, Greece

Athens, 11.05.2021

Dekan: Prof. Dr. Gerald Kerth

1. Gutachter: Prof. Dr. Lutz Schweikhard

2. Gutachter: Prof. Dr. Gerald Gwinner

Tag der Disputation: 28.04.2021

Contents

II

List of Figures

Nomenclature

Acronyms

CLS .... collinear laser spectroscopy

EIBT .... electrostatic ion beam trap

FWHM .... full width at half maximum

MR-ToF .... multi-reflection time-of-flight

PoP .... Proof-of-Principle

RF .... radio frequency

Symbols

ν .... frequency

A .... mass number

E .... energy

m .... mass

N .... revolution number

q .... ion charge

T .... revolution period

t .... flight time

v .... velocity

1 Introduction

Ever since its discovery more than a century ago, the atomic nucleus has been an intriguing object of study. Especially over the last decade, remarkable progress in experiment and theory have been made to understand the structure of atomic nuclei from first principles. In this context, the study of short-lived radionuclides is of special interest. For instance, the large asymmetry in the neutron-to-proton ratio in nuclides far away from stability may expose unexpected phenomena in the nuclear force. Thus, the most "exotic" nuclides, now available for experiments at modern radioactive ion beam (RIB) facilities, serve as critical benchmarks for state-of-the-art nuclear theory.

Among the many experimental approaches to study radioisotopes, collinear laser spectroscopy (CLS) is, due to its high accuracy and resolution, a powerful tool to measure nuclear ground state properties such as nuclear spins, electromagnetic moments and mean-square charge radii of short-lived radionuclides. In order to reveal the hyperfine spectrum which allows one to determine the aforementioned fundamental nuclear properties in the CLS technique, a narrow-band laser beam is overlapped with a beam of ions. When the wavelength of the laser beam matches the energy difference of the selected electronic transition, ions are excited. For the detection of the fluorescence light during the de-excitation of the laser-excited ions, photodectors are employed in an optical detection region (ODR). CLS can also extented to neutral atoms when a charge-exchange cell is placed in front of the ODR to neutralize incoming ions in collisions with alkali vapor.

To reach the high resolution in CLS, fast beams (E>30 keV) are used which provides an excellent spectral resolution approaching the natural linewidth of an optical transition. This is achieved because the Doppler width $\delta\nu_D$ is minimized according to $\delta\nu_D \propto \delta E/\sqrt{E}$ [1], where δE represents the energy spread of the ion beam.

Today, CLS is performed with bunched beams which are typically formed by accumulating a continuous ion beam in a buffer-gas-filled Paul trap. In addition to the cooling of the ion ensemble, this approach allows the reduction of the CLS background by gating the photon signal on the ion bunch's arrival in front of the photodetectors. Consequently, the photon background due to laser stray-light, which is integrated over tens of milliseconds for continuous beams, is limited to a few microseconds when the accumulated ion bunch passes the ODR. Nevertheless, the fluorescence-light detection typically limits the successful application of CLS to nuclides with yields of at least a few thousands ions/s, depending on the specific case and spectroscopic transition. In the context of nuclides with low productions yields, it is hence of disadvantage that the laser-ion interaction and observation time for fluorescence photons emitted by laser-excited ions is limited to a time scale of a few microseconds when the ions pass the ODR. In contrast, the half-lives of the radioactive nuclides studied at low-energy branches of RIB facilities range from milliseconds up to several seconds or longer.

To extend the reach of CLS to the most exotic nuclides with very low production yields,

more sensitive methods have to be developed. To this end, the Multi Ion Reflection Apparatus for CLS (MIRACLS) is currently under development at ISOLDE/CERN. This novel technique aims to combine the high resolution of conventional fluorescence based CLS with a high experimental sensitivity, enhanced by a factor of 30 to 600 depending on the mass and lifetime of the studied nuclide. By repetitively reflecting the ion beam between the two sets of electrostatic mirrors of a Multi-Reflection Time of Flight (MR-ToF) device, the laser beam probes the ion bunch during each revolution. Therefore, the observation time is extended and the experimental sensitivity is enhanced compared to conventional single-passage CLS.

As a first step of the project, a Proof-of-Principle (PoP) setup developed and built around an MR-ToF device originally built for other purpose [2] which was modified for the purpose of CLS [3, 4]. This setup has been utilised to successfully demonstrate the functionality of the MIRACLS concept. Moreover, its results have served as benchmark for the simulation approach which is used for the design of a dedicated 30 keV MR-ToF device [5]. This thesis introduces the MIRACLS concept and presents the Proof-of-Principle (PoP) setup. Moreover, the results for MIRACLS measurements in ions of stable magnesium and calcium isotopes are presented. This work has systematically characterized the performance of MIRACLS, especially in terms of its sensitivity enhancement and measurement accuracy.

2 Laser spectroscopy for nuclear structure research

2.1 Physics addressed by laser spectroscopy of short-lived radionuclides

Laser spectroscopy is a powerful tool to study properties of nuclear ground states and long lived isomers in radionuclides [6, 7]. To this end, measurements of the hyperfine structures and isotope shifts in the atomic spectra of radioactive nuclei provide unique insights into the electromagnetic moments of an atomic nucleus as well as into differences in mean square nuclear charge radii between different isotopes along an isotopic chain of a chemical element. These measurements can be performed with high precision and accuracy which allows the determination of the aforementioned observables in a nuclear-model independent way. In the application of laser spectroscopy at radioactive ion-beam (RIB) facilities such as ISOLDE at CERN [8, 9], the sensitivity can be defined as the minimum number of ions per second of a given nuclide, produced in a target and then delivered to experiment, which is still sufficient to carry out a successful measurement. The further one reaches out to nuclides far away from the valley of stability, the lower is typically the production yield and hence, the higher the demand on experimental sensitivity in order to investigate these most "exotic" nuclides.

2.1.1 Hyperfine structure

According to the Bohr-Rutherford model, the atom consists of an ensemble of electrons with an electrically negative charge which surrounds the atomic nucleus. The latter is very massive and constitutes an attractive force on the light electrons due to its positive electric charge . The energy of an atom, as a first approximation, can be extracted by coupling the total orbital momentum $\mathbf{L}$ and the spin angular momentum $\mathbf{S}$ of the electrons which are moving in the extended Coulomb field of a point-like nucleus of a charge $Z \cdot e$ to a new angular momentum $\mathbf{J} = \mathbf{L} + \mathbf{S}$ (spin-orbit coupling). This describes the atomic energy levels up to the fine structure. Taking into account that the atomic nucleus is in fact an object with a non-vanishing size and is not infinitely heavy leads to a shift in an isotope's fine structure levels. This manifests itself in the so-called isotope shift, i.e. a small isotope dependency of the transition between fine structure levels in a chemical element. Moreover, the atomic nucleus may possess in addition to its electric charge also a non-zero nuclear spin I as well as nuclear moments (magnetic and quadrupole moment). These result in an additional splitting of the atomic levels, the hyperfine splitting. More specifically, the electromagnetic interaction between the nuclear moments and the surrounding electron cloud causes the splitting of electronic fine-structure levels. This leads to the hyperfine structure which is observed in spectra

of neutral atoms, ions and molecules [10].

A nucleus with spin **I** has a nuclear magnetic moment $\boldsymbol{\mu}_I$ that relates to the nuclear spin **I** according to

$$\boldsymbol{\mu}_I = \frac{g_I \mu_N \mathbf{I}}{\hbar} \tag{2.1}$$

The interaction between the magnetic moment $\boldsymbol{\mu}_I$ and the magnetic flux density created by the atomic electrons $\boldsymbol{B}_e$ is depicted by the Hamiltonian

$$H_{HFS} = -\boldsymbol{\mu}_I \cdot \boldsymbol{B}_e \tag{2.2}$$

The coupling of the total electronic angular momentum **J** and the spin of the nucleus **I** results in a total angular momentum **F** which is the vector sum of the nuclear spin **I** and the electronic spin **J**, $\mathbf{F} = \mathbf{J} + \mathbf{I}$ ($| I - J | \leq F \leq I + J$) [10]. The magnitude of the hyperfine splitting is in the order of μeV compared to fine structure splitting which is in the order of meV.

The energy shift of an atomic level **F** due to the magnetic dipole interaction is given by

$$\Delta E_{dip} = \frac{A_J h}{2} [(F(F+1) - I(I+1) - J(J+1)] \tag{2.3}$$

where the (magnetic) hyperfine coupling constant is defined as

$$A_J = \frac{\mu B_J}{IJ} \tag{2.4}$$

It is worth to mention that from laser spectroscopy measurements the magnetic moment cannot be extracted in case of J=0 or I=0.

The interaction of the electric nuclear quadrupole moment Q_s with the electric field gradient $\frac{\partial^2 V}{\partial z^2}$, along the symmetry axis z produced by the electrons induces an additional energy shift:

$$\Delta E_{quad} = \frac{B}{4} \frac{(3/2)C(C+1) - 2I(I+1)J(J+1)}{I(2I-1)J(2J-1)} \tag{2.5}$$

where the hyperfine constant B is defined as:

$$B = eQ_s \frac{\partial^2 V}{\partial z^2} \tag{2.6}$$

Here Q_s is the spectroscopic quadrupole moment and, e is the electric charge. In the case of I < 1 or J < 1 the quadrupole splitting is zero. Combining the terms arising from the nuclear magnetic dipole and electric quadrupole moments, the energy shift for each atomic hyperfine level is given by [10]:

$$\Delta E_{HFS} = \Delta E_{dip} + \Delta E_{quad} \tag{2.7}$$

Thus, the hyperfine structure of spectral lines is a consequence of the interaction between the nuclei and their electron cloud and thus allows nuclear magnetic dipole moments and electric quadrupole moments to be determined.

The hyperfine structure of an atom can be studied, amongst others, via laser spectroscopy where an atom or an ion can resonantly be excited by a laser photon of the
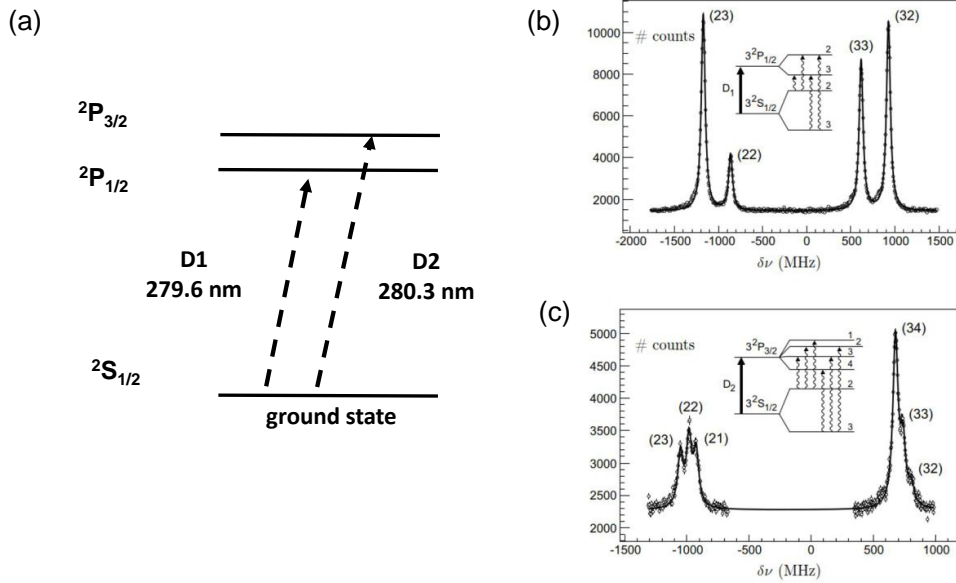
Figure 2.1: (a) Fine structure transition for single charged magnesium ions such as $^{24}Mg^+$ and $^{26}Mg^+$. For each transition, the wavelength is depicted [11]. (b) Hyperfine spectra of $^{25}Mg^+$ (I=5/2) in the D1 and (c) D2 line. The inserts illustrated the splitting of the energy states. Figure from [12].

appropriate wavelength and then subsequently decay into lower states by emission of a fluorescence photon [8].. By recording the number of photons as a function of the scanned laser frequency, the hyperfine spectrum (HFS) of the selected optical transition is revealed.

To provide an example, relevant for the experimental work in this thesis, in figure 2.1, the fine structure transition for D1 and D2 in singly charged magnesium ions such as $^{24}Mg^+$ and $^{26}Mg^+$ are illustrated. These ions species have been selected as a first test-cases in MIRACLS' proof-of-principle (PoP) experiment since they have no hyperfine splitting of the fine-structure levels due to their zero nuclear spin (I=0). As a result, it exhibits a closed two-state structure for the $3s^2S_{1/2} \rightarrow 3p^2P_{1/2}$ (D1) as well as $3s^2S_{1/2} \rightarrow 3p^2P_{3/2}$ (D2) transitions. Hence, a laser-excitation will always decay back into the initial ground state and no optical pumping to another (hyper-)fine structure state will take place. For $^{25}Mg^+$, the nuclear spin is I=3/2. This results in a hyperfine splitting of the ground and excited state which is reflected in the spectrum of the hyperfine structure as it is shown in figure 2.1 (b) and (c).

2.1.2 Isotope shift and charge radii

The isotope shift of an optical transition is one of the observables that can be obtained from laser spectroscopy, if the hyperfine spectrum of more than one isotope is measured. The isotope shift is defined as the difference in the fine structure transitions between of two different isotopes A and A' of the same chemical element. Due to the different number of neutrons of the involved isotopes, they have a different mass and the protons

are redistributed different inside the atomic nucleus. This slightly modifies the energy of the electrons and hence, gives rise to the observed isotope shift. The isotope shift can be expressed as [7]:

$$\delta\nu^{AA'} = \delta\nu_{MS}^{AA'} + \delta\nu_{FS}^{AA'} \tag{2.8}$$

where $\delta\nu_{MS}^{AA'}$, the mass shift relates to the change in reduced mass of the electron-nucleus system and $\delta\nu_{FS}^{AA'}$, the field shift, reflects the change of the charge distributions inside the nucleus. These contributions can be written as follows:

$$\delta\nu_{MS}^{AA'} = K_{MS}\frac{m_{A'} - m_A}{m_{A'}(m_A - m_e)} \tag{2.9}$$

$$\delta\nu_{FS}^{AA'} = F\delta\langle r^2\rangle^{A,A'} \tag{2.10}$$

where m_A and $m_{A'}$ are the nuclear masses of isotopes with atomic mass A and A', m_e is the electron mass, F the field shift factor and K_{MS} the total mass shift coefficient. The latter contains two components: the specific mass shift and the normal mass shift ($K_{MS} = K_{SMS} + K_{NMS}$). The normal mass shift factor reflects the change in the reduced mass of the electron-nucleus system and it can be extracted using $K_{NMS} = \nu^A \cdot m_e$, where ν^A depicting the transition frequency with respect to the fine-structure levels. On the other hand, the specific mass shift reflects the changes in the correlations between the electrons and its calculation is often a significant challenge for atomic theory. The field shift is proportional to the change in the transition energy of the electron between the upper $|j\rangle$ and the lower $|i\rangle$ electronic states which are involved, $\Delta|\Psi_e(0)|_{i\rightarrow j}^2$. Thus, the field shift contribution in the isotope shift can be expressed

$$\delta\nu_{FS}^{AA'} = -\frac{Ze^2}{6\epsilon_0}\Delta|\Psi_e(0)|_{i\rightarrow j}^2\delta\langle r^2\rangle^{A,A'} = F\delta\langle r^2\rangle^{A,A'} \tag{2.11}$$

If K_{MS} and F are known, the mean-squared (rms) charge radii of an atomic nucleus can be obtained by using an isotope shift measurement, $\delta\nu^{AA'}$ via the formula

$$\delta\langle r^2\rangle^{A,A'} = \frac{\delta\nu_{FS}^{AA'}}{F} - K_{MS}\frac{m_{A'} - m_A}{Fm_{A'}(m_A - m_e)} \tag{2.12}$$

Although laser spectroscopy allows for the precise determination of changes in mean-square charge radii along an isotopic chain via isotope shifts measurements, it cannot provide absolute charge radii. At present, two complementary techniques are applied to obtain absolute charge radii: elastic electron scattering [13–15] and X-ray spectroscopy of muonic atoms [16–19]. In the former, information about the nuclear charge distributions are extracted by the scattering of high-energy electrons (> 50 MeV) on atomic nuclei. More specifically, this method is equivalent to the Rutherford scattering technique with the difference that in this case the considered interaction between the incident electrons and the investigated nucleus is only the electromagnetic force. With the assumption of a point nucleus of small charge without spin and magnetic moment the differential cross section from the electron scattering can be calculated by Mott's formula in the Born approximation. If ones take into account the finite size of the nucleus then enters the "form or structure factor" into the Born approximation through which the electric charge and the magnetic distributions inside the nucleus can be determined. From

the X-ray spectroscopy of muonic atoms, one can deduce the nuclear charge radii with high precision based on the detection of the muonic X-rays emitted following to the atomic capture of a negative muon. In muonic atom spectroscopy, a negative muon beam bombards a target material and due to the interaction between the muons and the outer atomic electrons, they slow down and are finally captured by the atom. The capture is followed by the emittance of X-ray photons during the cascade of the muon from a high initial state to the ground state. By detecting these X-rays, the muonic energy level scheme can be determined from which the nuclear charge radius or its quadrupole moment can be deduced. However, these methods cannot easily be applied to short-lived radionuclides as large sample quantities are required. Respective data usually exists only for stable nuclides. Thus, a combination of the data from optical isotope shift measurements and electron scattering and/or muonic-atom spectroscopy allows one to extract absolute charge radii also for radionuclides.

2.1.3 Magnetic dipole moment

The magnetic dipole moment of the nucleus is originating from two effects: the orbiting motion of the protons and the intrinsic angular momentum, also called intrinsic spin, of all nucleons. Therefore, the magnetic dipole moment operator of the nucleus can be expressed as the sum of the individual contributions of the nucleons:

$$\boldsymbol{\mu} = \frac{\mu_N}{\hbar}\left(\sum_i^A g_l^i \boldsymbol{l_i} + \sum_i^A g_s^i \boldsymbol{s_i}\right) \tag{2.13}$$

Here the g_l and g_s are the orbital and spin gyromagnetic ratios, respectively. For a free proton and neutron are given by [20]:

$$\begin{aligned} g_l^\pi &= 1 \quad \text{and} \quad g_s^\pi = +5.585694700(18) \quad \text{(free proton)} \\ g_l^\nu &= 0 \quad \text{and} \quad g_s^\nu = 3.82608545(90) \quad \text{(free neutron)} \end{aligned} \tag{2.14}$$

Alternatively, the magnetic moment operator can be written as a function of the total nuclear spins I

$$\boldsymbol{\mu_I} = \frac{g\mu_N \boldsymbol{I}}{\hbar} \tag{2.15}$$

with g the nuclear gyromagnetic ratio, $\hbar$ the Planck constant and μ_N the nuclear magneton. The nuclear magneton μ_N is related to the Bohr magneton μ_B by the electron-to-proton mass ratio

$$\boldsymbol{\mu}_N = \mu_B \frac{m_e}{m_p} \tag{2.16}$$

where m_e and m_p are the electron and proton mass, respectively. The experimental magnetic dipole moment is the expectation value of the of the z-component of the magnetic dipole operator for a state $|I, m = I>$

$$\mu = < I, m = I|\boldsymbol{\mu_z}|I, m = I >= gI\mu_N \tag{2.17}$$

The magnetic moment provides information about the orbital occupation of the valence nucleons. This can be understood in a shell-model picture in which the magnetic moment

of an odd-A nucleus is - in first approximation - determined by the last unpaired nucleon. For this last valence nucleon placed in an orbit with $j = l \pm s$, the single-particle magnetic moment can be deduced according to the following formulas [21]:

$$
\begin{aligned}
\mu &= g_l \left(j - \frac{1}{2} \right) + \frac{1}{2} g_s, \quad j = l + \frac{1}{2} \\
\mu &= g_l \frac{j(j + \frac{3}{2})}{j + 1} - \frac{j g_s}{2(j + 1)}, \quad j = l - \frac{1}{2}
\end{aligned}
\tag{2.18}
$$

Using the g factors from Eq. (2.14) the free magnetic moments for a single proton and neutron, so-called *Schmidt moments*, can be calculated. However, it is found that experimentally the magnetic moments are better reproduced using effective g-factors which take into account the presence of the nuclear medium. Typical values are $g_{s,eff} \sim 0.7 g_s$ and $g_{l,eff} \sim g_l$, although they vary depending on the mass region. For an odd-odd nucleus, the magnetic moment can be derived by taking into consideration the contribution from both odd proton (μ_π) and odd neutron (μ_ν) [22]:

$$
\mu = \frac{I}{2} \left[\frac{\mu_\pi}{j_\pi} + \frac{\mu_\nu}{j_\nu} + \left(\frac{\mu_\pi}{j_\pi} - \frac{\mu_\nu}{j_\nu} \right) \frac{j_\pi(j_\pi + 1) - j_\nu(j_\nu + 1)}{I(I + 1)} \right]
\tag{2.19}
$$

While effective single particle-values for the proton and neutron magnetic moment can be used, empirical values of the neighbouring odd mass nuclei usually give a better estimation of the experimental magnetic moment.

In conclusion, by measuring the magnetic moments of both odd-A and odd-odd nuclei, information about the nuclear wavefunction can be deduced.

2.1.4 Electric quadrupole moment

The nuclear electric quadrupole moment is a parameter which gives information about the shape of the nuclear charge distribution.
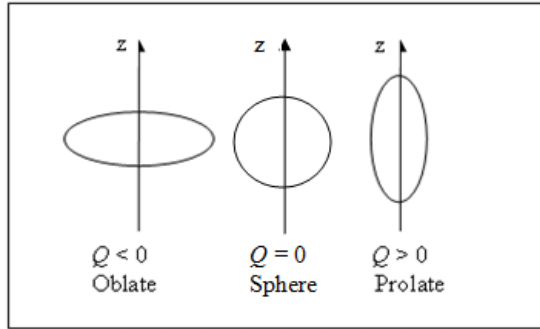

Figure 2.2: The spheroidal shapes of nuclei as indicated by the value of the electric quadrupole moment Q. Figure from [23].

The quadrupole moment operator of a nucleus is defined as [24]:

$$
\boldsymbol{Q} = \sum_{i=1}^{A} e_i (3 z_i^2 - r_i^2) = \sqrt{\frac{16\pi}{5}} \sum_{i=1}^{A} e_i r_i^2 Y_2^0 (\theta_i, \phi_i)
\tag{2.20}
$$

in cartesian or spherical coordinates, respectively. Instead of using free proton and neutron charges, also here effective values give quadrupole moments in better agreement with the experiment. Typical values are $e_\pi \approx 1.3e$ and $e_\nu \approx 0.5e$. Note that despite the fact that the neutron carries no charge, it still contributes to the quadrupole moment.

Similar to the magnetic moment, the quadrupole moment which is observed in the experiments, called spectroscopic quadrupole moment Q_s, is derived by taking the expectation value of the $\hat{Q}_z$ in the studied state |I,m=I>:

$$Q_s = <I, m = I|\boldsymbol{Q_z}|I, m = I> = \sqrt{\frac{I(2I-1)}{(2I+1)(2I+3)(I+1)}} <I, m = I||\boldsymbol{Q_z}||I, m = I>$$
(2.21)

This demonstrates that the spectroscopic quadrupole moment of a nucleus with spin < 1 is 0.

Quadrupole moments are typically discussed in the context of deformation which arises due to the collective effect of many nucleons. By convention, Q is positive if the shape is prolate (rugby ball). In contrast, the value of Q is negative if the shape is oblate (discus). A spherical nucleus has a zero quadrupole moment. Experimentally, most nuclei are found to be prolate [25]. For axially symmetric nuclei with the nuclear spin having a well-defined direction with respect to the symmetry axis of the deformation, the spectroscopic quadrupole moment can be related to the intrinsic quadrupole moment Q_0 according to

$$Q_s = \frac{3K^2 - I(I+1)}{(I+1)(2I+3)}Q_0$$
(2.22)

Here, K the projection of the total spin I onto the symmetry-axis of the deformed nucleus. By measuring magnetic dipole moments and electric quadrupole moments as it is done e.g. in laser spectroscopy experiments, both single-particle effects as well as collective effects in the nucleus can be studied. In this interpretation, the intrinsic quadrupole moment is in turn related to the deformation parameter β, which describes the deformation of the non-spherical nucleus (but axially symmetric), through

$$Q_0 = \frac{3}{\sqrt{5\pi}}ZR_0^2\beta(1 + 0.36\beta)$$
(2.23)

2.2 Experimental techniques of laser spectroscopy

There are several experimental methods of laser spectroscopy of short-lived radionuclides that have been employed at various facilities worldwide. Most of the work reported here is about collinear laser fluorescence spectroscopy of fast atom or ion beams. One of the representative experiments of this technique is the COLlinear LAser SPectroscopy (COLLAPS) setup [8] at ISOLDE/CERN. In this method, an accelerated atom/ion beam is collinearly overlapped with a co- or counter-propagating laser beam. If the wavelength of the laser beam corresponds to the energy difference of an electronic transition of the ion/atom, they will be resonantly excited into a higher lying state. Dependant on its lifetime, the excited state decays by emitting a fluorescence photon which then can be detected using photo-multiplier tubes (PMT). Thus, by scanning the laser frequency and observing the subsequent decay of the fluorescent photons, the

hyperfine structure spectrum, as shown in figure 2.1, can be revealed. Finally, the nuclear structure information can extracted through fitting of the obtained spectra.

In order to reach high resolution in collinear laser spectroscopy, it is operated with fast beams ($\geq$30 keV). Very often, high resolution is essential to resolve the hyperfine structure. The use of such an accelerated beam minimises the resolution limit set by the Doppler broadening of the spectral lines which is a consequence of the thermal movements of the atoms in the ensemble. The thermal velocity v of ions/atoms in a gas at a certain temperature T follows the Maxwell-Boltzmann distribution. The corresponding Doppler width $\delta\nu_D$ for an atom of mass m and optical transition frequency ν_0 is given by [26]:

$$\delta\nu_D = \frac{\nu_0}{c}\sqrt{\frac{8k_BT\ln 2}{m}} = \frac{\nu_0}{c}\delta v \tag{2.24}$$

where ν_0 is the transition frequency, m is mass of the atom, k_B is the Boltzmann constant. The δv represents the relative spread in the velocity of the ions, which is not zero due to the gas temperature.

When the ions are leaving from an ion source, they also exhibit a certain spread in their kinetic energy δE which results in a velocity spread. By applying an acceleration voltage U_{acc}, all ions within a beam gain the same amount of kinetic energy $e \cdot U_{acc}$ such that their initial energy spread δE remains the same. The velocity spread corresponding to this δE can be then calculated:

$$\delta E = \delta\left(\frac{1}{2}mv^2\right) = mv\delta v = constant \tag{2.25}$$

This means that with the rise of the absolute velocity v, their velocity spread δv is decreasing. Using the relation $v = \sqrt{2eUm}$ and combining it with equation 2.24 gives a Doppler width of $\delta\nu_D = \nu_0\delta E/\sqrt{2eUmc^2}$, with U the acceleration voltage. At typical acceleration voltages of 30 keV and initial energy spreads of a few eV, the Doppler broadering is in the order of a few tens of MHz, comparable or smaller than the natural linewidth for many transitions. For most of the isotopes, the hyperfine splittings are in the order of 10-1000 MHz [8] and can therefore be resolved by CLS using fast beams with a kinetic energy of more than 30 keV.

The Doppler-shifted frequency ν can be calculated using the relativistic Doppler effect:

$$\nu = \nu_0\frac{(1 - \beta cos\phi)}{\sqrt{(1 - \beta^2)}} \tag{2.26}$$

where ϕ is the angle between the propagation direction of the radiation and the velocity v of the observer, ν the frequency seen by the ion/atom, ν_0 the frequency of the laser in the laboratory frame, $\beta = |v/c|$ the relativistic Lorentz factor. For collinear or anti-collinear beam-laser geometry, it is given by:

$$\nu = \nu_0\frac{(1 \pm \beta)}{\sqrt{(1 - \beta^2)}} \tag{2.27}$$

with $<+>$ for the anti-collinear ($\cos(180°) = 1$) and $<->$ for the collinear ($\cos(0°) = +1$) case.

Although in fast beam CLS a high resolution can be obtained, the sensitivity of
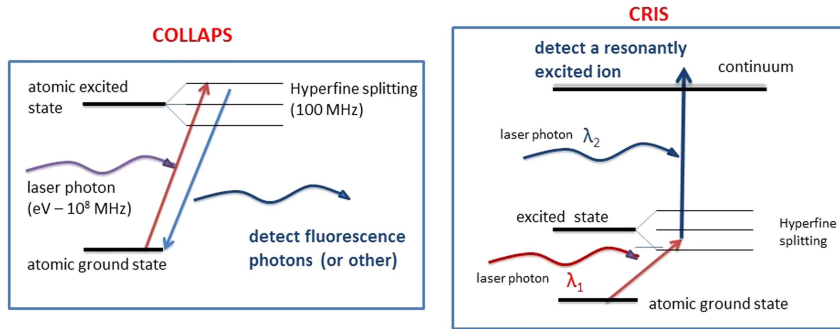
Figure 2.3: Schematic of two laser spectroscopy experiments at ISOLDE. Left: the scheme used at the COLLAPS beam line. Right: a typical scheme for CRIS setup. Figure from [8].

fluorescence-based CLS is limited by the efficiency of the fluorescence-photon detection as well as by the presence of background originating from the detector's dark counts, scattered laser light and light from ion collisions with residual-gas molecules. The limitation in sensitivity due to the aforementioned type of high background count rate becomes a considerable effect when working with exotic nuclei which have low yields and short half-lives. Background reduction can be achieved by using bunched beams. For this purpose, a radio-frequency quadrupole cooler and buncher, such as ISCOOL [27,28] at ISOLDE/CERN can be employed in which a continuous ion beam is accumulated and afterwards released as bunches with a well-defined time structure. By recording only the resonance fluorescence signal during the time the bunch appears in front of the light-collection region, the background in the photon detection is reduced by factors up to 10,000 and a gain in sensitivity by about two orders of magnitude can be accomplished. For instance, the charge radii of ^{49,51,52}Ca that extracted with a yield of a few hundred ions per second at ISOLDE/CERN, were measured for the first time with this technique of bunched ion beams [29]. For studying neutral atoms in CLS, a charge-exchange process to neutralize the ion beam needs to be employed. The neutralization can be achieved in a so-called charge-exchange cell (CEC) filled with a thin vapor of an alkali element. Neutralization is then achieved via collisions between the ions and the element inside the CEC. The main efficiency loss factor of this method is caused by the filling of different atomic excitation states inside the neutralized atom. This means that not all atoms are accessible to the chosen spectroscopic transition frequency.

An alternative solution to the problem of sensitivity and background-free particle detection can be found in the combination of collinear laser spectroscopy with the principle of laser resonance ionisation which is used by the Collinear Resonance Ioniza-tion Spectroscopy (CRIS) experimental setup [30] at ISOLDE/CERN. The underline principles of this method is to use two or three lasers in order to not only resonantly excite the atoms to the atomic state of interest with a single narrow-band laser but also to subsequently ionise the resonantly excited atoms. The ions are then separated from the neutral atoms via electrostatic deflector plates and are efficiently detected by particle detectors. Therefore, this process is very selective which provides the opportunity to

detect the optical resonance by counting ions very efficiently and virtually without any background.

Compared to CLS, the in-source laser spectroscopy technique is currently one of the most sensitive and efficient laser spectroscopy techniques available at radioactive ion beam (RIB) facilities. It is used for instance at the Resonance Ionization Laser Ion Sources (RILIS) of the ISOLDE facility at CERN [31]. In a number of cases the limit of its sensitivity (so the required yields in ions per second) can be lowered down to 1-10 ions/s [32, 33] instead of the typical values required for other collinear laser spectroscopy methods like in COLLAPS which lie within $10^2 - 10^4$ ions/s. Since the resonance ionization is performed either in a hot environment (hot cavity). The method's limitation lies in the Doppler broadening (see equation 2.24) of optical resonances in the GHz range [7]. For masses >100A or sufficiently large HFS splittings, the structures can still be resolved as has been demonstrated in a multitude of experiments [33, 34].

All laser-spectroscopy techniques mentioned above are applicable for revealing the structure of atoms and positive ions. However, in nature and more specifically in the solar atmosphere, in the interstellar medium and in plasma, there are also negative ions, i.e. atoms or molecules with an additional electron. Their nuclear structure cannot be determined with the traditional spectroscopic methods since all their transitions are optically forbidden due to their few bound excited states which usually have the same parity [35]. As a consequence of the lack of bound excited states, there is often only one atomic parameter which can be determined with high accuracy at RIB facilities. This is the energy released when an additional electron is attached to a neutral atom forming a negative ion, the so called electron affinity (EA) of the neutral atom. The
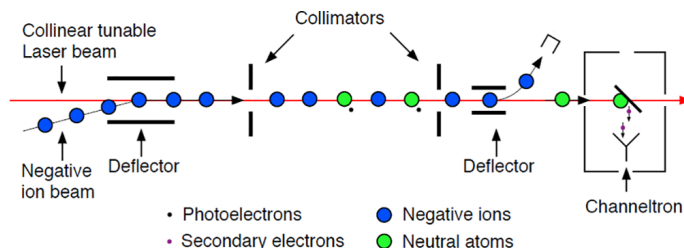
Figure 2.4: Schematic representation of the GANDALPH beamline. Figure from [36].

experimental studies of the inter-electronic interactions, which determine the binding potential of the additional electron in a negative ion, can serve as a useful test for theoretical models beyond the independent particle model. The experimental arrangement used for studying photo-detachment of radioactive negative ions at ISOLDE is the Gothenburg ANion Detector for Affinity measurements by Laser PHotodetachment (GANDALPH) [36, 37]. A beam of negative ions (blue in fig. 2.4) is overlapped with a laser beam (red arrow in fig. 2.4), in either a co- or counter-propagating geometry. During the photo-detachment process, neutral atoms (green in fig. 2.4) are produced which hit a target and create secondary electrons which are detected by an electron multiplier. Hence, by scanning the laser frequency and counting the neutral atoms, the threshold energy of the photo-detachment is found which corresponds to the electron affinity.

Despite the remarkable progress that has been made in the field of laser spectroscopy at RIB facilities over the past decades, there are still large unexplored regions in the nuclear chart. This is due to the very low productions of the most exotic nuclides far away from stability and of the lack of accessible transitions from existing laser systems. Thus, to extend the studies to exotic nuclides far away from stability, more sensitive and high resolution methods are needed. For this reason, a novel electrostatic ion beam trap (EIBT) for ultra-sensitive collinear laser spectroscopy of radionuclides is currently under development at ISOLDE/CERN. The idea is to employ an EIBT, or also called multi-reflection time-of-flight (MR-ToF) device [38], in order to overcome the sensitivity limit of conventional fluorescence-based collinear laser spectroscopy, where currently at least about hundred ions per second are needed to obtain a hyperfine spectrum. More details about this topic, which is the main subject of this thesis, will be given in section 3.2 and chapter 4.

2.2.1 Line shape of CLS spectra

The line shape and width of a resonance in the hyperfine spectrum is affected by several broadening mechanisms. The main sources of broadening are:
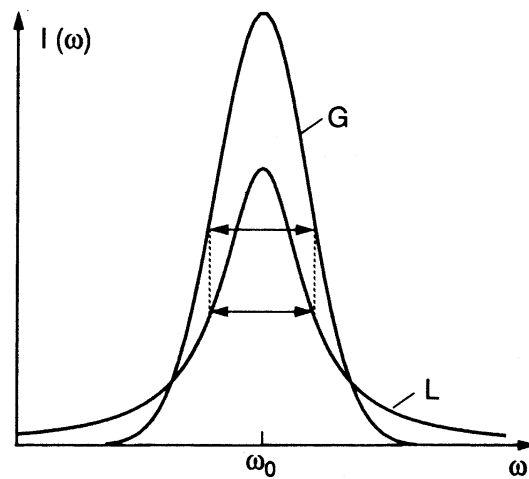
Figure 2.5: Comparison between Lorentzian (L) and Gaussian (G) line profiles of equal half-widths. Figure from [39].

- **Lifetime broadening** is an important contribution influence of the line shape obtained with high-resolution CLS. The Heisenberg's uncertainty principle for the energy, $\Delta E \Delta \tau \geq \frac{\hbar}{2}$, determines the minimal possible line width, the so called natural linewidth. As the excited state decays exponentially in time, a line profile of Lorentzian shape in terms of frequency is produced. The Lorentz profile is given by

$$L(x, \Gamma_L) = \frac{1}{\pi} \frac{\Gamma_L/2}{x^2 + (\Gamma_L/2)^2} \tag{2.28}$$

Due to the finite life time of the excited state τ the natural linewdth can be described by $\Gamma = \frac{1}{2\pi\tau}$ with τ being the lifetime of the state. For the D1 and D2 line in Mg^+ ions the natural linewidth is 42 MHz in the $3p^2P_{3/2}$ and $3p^2P_{1/2}$ states [40].

- **Doppler broadening** is an additional contributor to the broadening of the spectral linewidth which arises due to the thermal motion of the atoms at any temperature T. It is described by a Gauss/normal distribution:

$$G(x,) = \frac{1}{\sigma\sqrt{2\pi}}e^{-\frac{x^2}{2\sigma^2}} \tag{2.29}$$

where σ is related to the Full Width Half Maximum (FWHM) of the Gaussian function via $\Gamma_G = 2\sqrt{2ln(2)\sigma} \approx 2.35482\sigma$. In the current thesis, the hyperfine spectra were fitted with Gaussian profile since for low ion-beam energies the Doppler broadening is the most significant contribution to the linewidth.

- **Power broadening** is caused by the saturation of the population in the absorbing levels. At sufficiently large laser intensities, the pumping rate on an absorbing transition becomes larger than the relaxation process rate and as a result the width of the spectral line is affected [41]. It can be described by a Lorentz function.

- **Pressure broadening (or Collision broadening)** is the result of inelastic collisions between atoms or molecules. The rate of the collisions are affected by the density and the temperature. The pressure broadening effect can be described by a Lorentzian profile. Due to the ultra-high vacuum in the optical detection region in the CLS experiments, the pressure broadening effects are normally negligible.

A comparison of the Lorentzian and Gaussian line shape is presented in figure 2.5. A convolution between these two functions is called a Voigt profile, which is commonly used to describe the resonance line shape in CLS.

3 Multi-Reflection Time-of-Flight (MR-ToF) Devices

The physics of trapped ions has evolved ever since the invention and development of ion traps about 50 years ago. For instance, electrostatic ion-beam traps (EIBT) have been first developed in the 1990s and since then they intensively utilised in molecular cluster physics [42, 43] as well in chemistry [44]. Recently, EIBTs have gained significant importance as multi-reflection time-of-flight mass spectrometers (MR-ToF MS) at RIB facilities for various studies in nuclear physics [45].

3.1 General overview

In an Electrostatic Ion Beam Trap (EIBT) [46–48] or Multi-Reflection Time-of-Flight (MR-ToF) device, an ion beam is confined by reflecting it between two electrostatic mirrors. These typically consists of a set of ring-shaped electrodes as for example illustrated in figure 3.1. They are separated by a field-free region, a so called drift tube. The typical revolution frequency is in the order of few kHz.
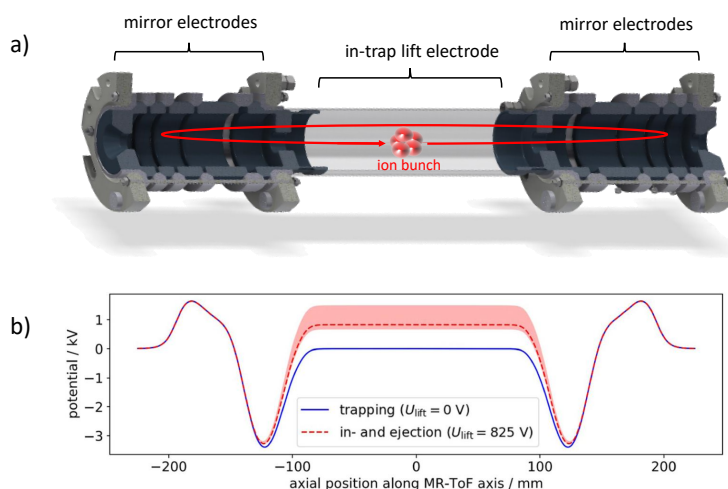

Figure 3.1: a) Sectional view of an MR-TOF device and b) Example of the distribution of the electric potential along the central axis of the MR-ToF device for a set of mirror potentials. The blue curve shows the potential switched to for capturing the ions by use of the in-trap lift. Figure b) from [5].

On first sight, the functionality of an MR-ToF device seems contradict Earnshaw's

theorem which states that charged particles cannot be stored only by electrostatic forces. However, the kinetic energy of the ions is very different from zero and and ion beams can indeed be stored by electrostatic devices such as the present one or storage rings [49].

MR-ToF instruments and EIBTs have found widespread use in modern physics. The first electrostatic ion beam traps were utilized to investigate the cluster and molecule properties [42, 43, 50–53]. More recently, they are used for precision mass spectrometry studies as well as a tool for ion separation of short-lived radionuclides due to their ability to reach high mass resolving powers ($R = m/\Delta m => \geq 10^5$) in just tens of milliseconds flight time [54–61]. For instance, at ISOLDE/CERN, about 10 years ago, ISOLTRAP collaboration [62] has employed for the first time an MR-ToF device, developed at the University of Greifswald, for high-precision mass measurements on short-lived radionuclides. This advance in ion-trap technology in rare isotope science, paved the way for the precision mass determination of exotic radionuclides at ISOLDE such as the masses of the calcium isotopes ^{53,54}Ca [55].
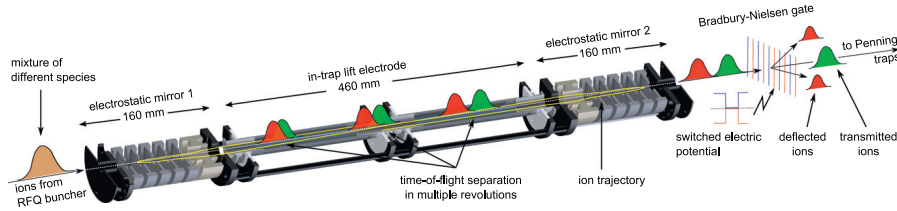
Figure 3.2: Schematic overview of the ISOLTRAP's MR-ToF MS including Bradbury-Nielsen Gate for the ion separation. Figure from [63].

In addition to mass measurements, this MR-ToF device can be used as a mass separator to suppress contamination in the ISOLDE beam, e.g. for subsequent Penning-trap mass measurements [64]. The mass selection is facilitated by a Bradbury-Nielsen Gate [65] which is installed behind the MR-ToF device. A schematic overview of ISOLTRAP's MR-ToF device is shown in figure 3.2. Ions with different masses m_i and charge q_i are transferred from an RFQ buncher to the MR-ToF device for ion beam storage. The time of flight (ToF) depends for a given ion-beam energy on the mass-to-charge ratio of the ions according to $t_i \propto \sqrt{m_i/q_i}$. After a specific number of reflections, the ions are ejected from the MR-ToF device and can be distinguished in ToF on an ion detector for mass measurements. The mass resolving power R of an MR-ToF device is given by

$$R = \frac{m}{\Delta m} = \frac{t}{2\Delta t} \tag{3.1}$$

where t is the total flight time and Δt is the time-of-flight width of one ion species at the detector plane. According to the above formula, one approach to increase the mass resolving power one is to extend the flight time t. Without the use of an MR-ToF instrument, this can be achieved by a longer flight path of the ions. This increases the dimensions of the time-of-flight (ToF) setup considerably which ultimately limits its feasibility. The use of an MR-ToF device, however, avoids the enlargement of the physical dimensions of the apparatus. An MR-ToF device has the capability to trap ion bunches for several thousand revolutions between the electrostatic mirrors. This

leads to an ion path which exceeds the physical length of the device of typically ~ 1 m by several orders of magnitude. As a consequence the mass resolving power is largely improved compared to conventional ToF mass measurements. For instance, a mass resolving powers of up to $R_{FWHM} = 3 \cdot 10^5$ have been achieved [66] in ISOLTRAP's MR-ToF device. In [67], a mass resolving power of $R_{FWHM} = 6 \cdot 10^5$ has been reported, achieved by trapping stable $^{133}Cs^+$ ions for 49 ms.

In addition to ISOLTAP MR-ToF mass spectrometer at ISOLDE/CERN, similar devices are coupled to other worldwide RIB facilities which reflects the importance of these instruments for experiments with rare and short-lived nuclei. Example for this recent development are the MR-ToF devices at Argonne National Laboratory [68], TITAN at ISAC/TRIUMF (Vancouver, Canada) [69], FRS/GSI (Darmstadt, Germany) [67], S3-SPIRAL2/GANIL (Caen, France) [70], SLOWRI at RIBF/RIKEN (Wak, Japan) [71] or IGISOL at the University of Jyväskylä (Jyväskylä, Finland) [72].

In this thesis, a novel use of an MR-ToF device will be presented. As discussed in sec. 3.3, the present work exploits an MR-ToF apparatus as a trap of the purpose of ultra-sensitive collinear laser spectroscopy.

3.2 Working Principle of MR-ToF devices

The axial confinement of the ions is accomplished by the outermost mirror electrode to which is applied a positive or negative potential to store positively ions. For radial refocusing of the ions during each revolution, a negative potential is applied to the innermost mirror electrodes which acts as a focusing lens. For the storage of negative ions, the polarity of the potentials is inverted. In order to capture incoming ions inside an MR-ToF device, the potential of the entrance mirror needs to be smaller than the ions kinetic energy $E_{kin} > U_{mirror} \cdot q$ such that the ions can pass the electrostatic mirror and reach the inner trap region (central drift tube).

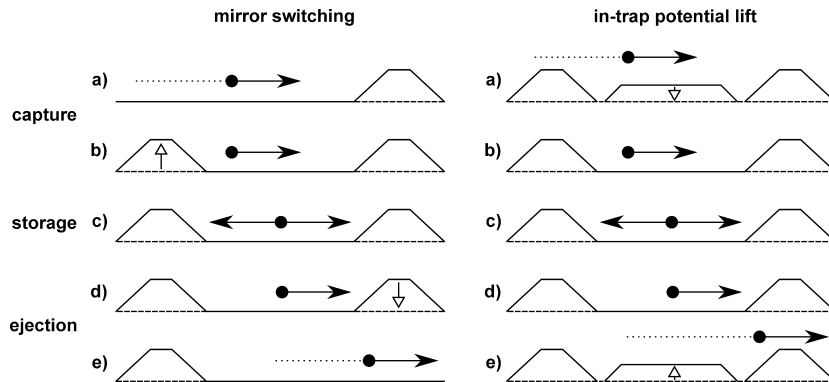Figure 3.3: Different techniques to capture ions in an MR-ToF device. Figure from [73].

There are two commonly used ion capture modes of an MR-ToF device. These are the mirror switching and the technique for an in-trap lift, see fig 3.3. In the former mode, the injection mirror is switched down to a lower potential while the ions are entering the MR-ToF device [45]. Afterwards, the injection mirror is switched back to the trapping

potential again in order to confine the ions inside the trapping region. After storing the ions for the desired time, the ion bunch can be ejected from the trap by switching down a mirror again.

In the in-trap lift technique, the mirror potentials always stay constant but the kinetic energy of the ions is modified. Initially, the ions kinetic energy E_{kin} surpassed the mirror potential $U_{mirror} \cdot q < E_{kin}$. The incoming ions hence pass the first electrostatic mirror and enter the central drift tube. The latter is set to U_{CDT} resulting in an ion beam energy of $E_{kin} = E_{kin,0} - U_{CDT} \cdot q$. When the ions are in the center of the central drift tube, its potential is switched to ground without effecting the ions. In this way, the ions are now trapped and reflected back and forth between the set of mirror electrodes until the in-trap lift is activated in opposite direction to release the ions from the MR-ToF device [63].

In addition, auxiliary electrodes for the shielding, the deflection or the pick-up can be implemented in an MR-ToF device. The purpose of the shielding electrodes are to protect the sensitive inner region from field penetration of the mirror due to electric fields from lenses or other ion-optical elements which are located up- or downstream of the MR-ToF device [74]. Moreover, deflector electrodes, which are located between the mirror electrodes and the central drift tube, help in the selection of the desired mass by deflecting the unwanted species. Different ion species will pass the deflector electrodes at different times due to their different mass-over-charge and as a result contaminants can be selectively deflected and no longer trapped in the MR-ToF device. This scheme is especially useful when large amount of ions of different ion species are to be mass separated. By means of the deflector electrodes individual ion species requiring a lower R can be quickly removed, which may otherwise disturb the ions of interest through so-called space-charge effects [67, 75, 76].

Finally, a pick-up electrode can be placed next to the mirror electrodes or more commonly in the middle of the drift tube. Those electrodes represent an interesting non-destructive diagnostic tool for the ion motion in a MR-ToF device. Once the ions are trapped, they can be detected with the pick-up electrode through the measurement of the image current which is induced by the periodically passing ions [77]. From the pick-up signal, the relative abundance of the stored ions, their masses or their lifetimes can be determined [78].

3.3 General concept of MIRACLS

The successful application of conventional fluorescence-based CLS as performed at today's RIB facilities, is typically limited to nuclides with yields of 100 to 10,000 ions/s delivered from an ion source, depending on the specific case and spectroscopic transition. However, there is a lot of theoretical interest to explore the properties of exotic nuclides far away from stability. The more "exotic", the lower is generally the production yield. Consequently, to push the boundaries of currently accessible nuclides forward, more sensitive laser-spectroscopic techniques have to be envisioned.

By taking a closer look at the measurement process of CLS experiments, one observes that the radioactive ions interact with the laser beam in the time scale of some microseconds, whereas the half-life of the isotopes range from several milliseconds to

seconds or even longer. By comparing the interaction time scale with the half-life of the isotopes, it is obvious that there is a large unexplored potential to increase the sensitivity of CLS. This is the underlying idea of the novel **M**ulti **I**on **R**eflection **A**pparatus for **CLS** (MIRACLS) project at ISOLDE/CERN which aims to reach into, in terms of CLS, uncharted regions on the nuclear chart. A schematic overview of the concept of MIRACLS can be seen in figure 3.4.
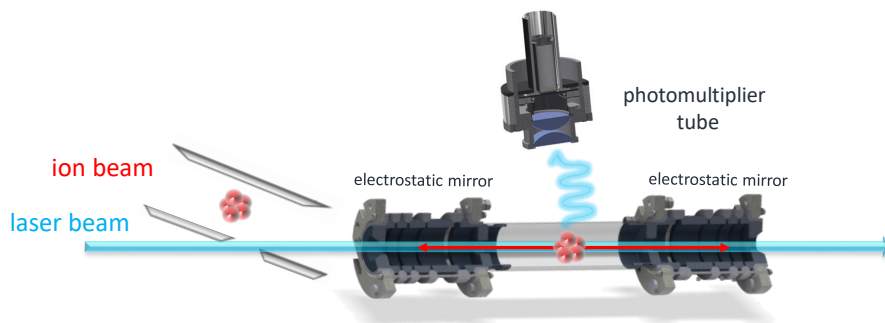

Figure 3.4: Schematic illustration of the MIRACLS concept.

The basic idea is to trap fast and bunched ion beams between two electrostatic mirrors while being overlapped with a laser beam which resonantly excites the ions. The emitted fluorescence photons following the de-excitation of the ions are detected in the optical detection region (ODR) by photo-multiplier tubes (PMTs) which are located in the middle of the MR-ToF central drift tube. The reflection of the ions between the two electrostatic mirrors enables the ion bunch to interact with the laser during each revolution. Thereby, the experimental observation time is notably extended compared to a single passage of the ions in front of the ODR in traditional CLS. For closed two-level systems in the studied optical transition, the enhancement of the observation time is only limited by the respective life time of the radioactive nuclides or the maximum trapping time. In conventional MR-ToF operation, ions can be stored in the trap for thousands of revolutions [79]. Hence the use of an MR-ToF device at MIRACLS it will make it possible to isolate a laser spectroscopic signal out of the background even for exotic nuclides with low production yields and detect signals which would not be detectable with conventional CLS techniques. This is illustrated by the plots on the left of figure 3.5. Here, the simulated resonance spectra are shown for a signal-to-background ratio (in the center of the resonance) of $\approx 1/6$. While the resonance is not visible in the spectrum of a single passage as in conventional CLS, it emerges out of the background when trapping the ions for many revolutions at MIRACLS.

In order to maintain the high resolution of conventional CLS, the MIRACLS approach ultimately envisions an unprecedented MR-ToF device which works with ion beam energies of ≈ 30 keV. Like CLS, MIRACLS' ultimate goal is to work with ion beam energies of more than 30 keV such that the spectral resolution approaches the natural linewidth. It is worth to be mentioned that all the MR-ToF devices built so far use ion beam energies around a few keV.

The extension in observation time facilitated by MIRACLS increases the CLS signal as well as the background by the same factor r. Here the factor r represents the number of
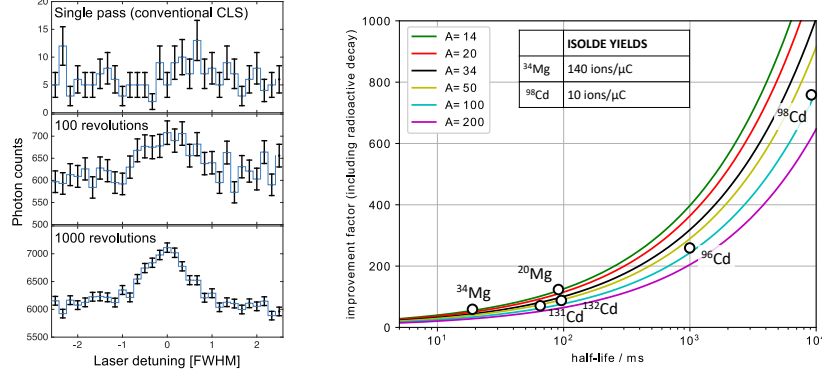
Figure 3.5: *Left plot*: Simulated photon counts for a single passage, 100 and 1000 revolutions of an ion bunch in the ODR of the MR-ToF device. Figure from in the thesis article III [4].*Right plot*: Improvement factor in experimental sensitivity at MIRACLS in comparison to conventional CLS experiments as a function of the nuclides' half-life $T_{1/2}$ and the mass number A. Some of the first science cases of MIRACLS are indicated with white circles.

revolutions inside the MR-ToF device. However, the statistical noise in the background only increases proportional to $\sqrt{r}$ if Poisson statistics is assumed. Due to the fact that the ions can be probed by the laser beam multiple times, the signal S and background B increase both linearly with the number of revolutions r in the MR-ToF device. The signal-to-noise ratio for all the revolutions in the MR-ToF device S/N is given by

$$\frac{S}{N} = \frac{S}{\sqrt{B}} = \frac{rs}{\sqrt{rb}} = \sqrt{r}\frac{s}{\sqrt{b}} = \sqrt{r}\frac{s}{n} \tag{3.2}$$

where the s and b is the CLS signal height and the background for one revolution in the MR-ToF device, respectively. Therefore, at MIRACLS the signal-to-noise ratio improves by a factor of $\sqrt{r}$. The number of revolutions in the MR-ToF device can be determined by the ratio of the trapping time t_{trap} and the time for one revolution t_1, such that $r = t_{trap}/t_1$.

In the study of short-lived nuclides ions are lost due to radioactive decay, hence the improvement factor is reduced compared to eq. 3.2. The CLS signal for all revolutions S, by taking into account the radioactive decay of nuclides with a half-life $T_{1/2}$, is given by

$$S \approx \sum_{i=0}^{r} \epsilon N_0 R exp\left(-i\frac{\ln 2}{T_{1/2}}t_1\right)\Delta t_0 \tag{3.3}$$

Here ϵ is the detection efficiency of the ODR, N_0 the initial number of trapped ion of interest, R the fluorescence photon emission rate and Δt_0 the time interval where the ions are in the ODR. Respectively, the background for all revolutions B follows as

$$B = \sum_{i=0}^{r} B_0\Delta t_0 = rB_0\Delta t_0 \tag{3.4}$$

where B_0 is the background rate due to PMT dark counts and the laser stray light. The signal-to-noise ratio for all revolutions, taking into account the radioactive decay, can

be written as

$$\frac{S}{N} \approx \frac{\epsilon N_0 R \frac{T_{1/2}}{\ln 2}\left[1 - exp\left(-\frac{\ln 2}{T_{1/2}}t_{trap}\right)\right]}{\sqrt{B_0 t_{trap}}} \qquad (3.5)$$

The optimal trapping time is $t_{trap} = 1.181265T_{1/2}$ and it can by extracted via the formula

$$\frac{\partial(S/N)}{\partial t_{trap}} = 0 \qquad (3.6)$$

Based on this analysis, the MIRACLS improvement factor in experimental CLS sensitivity for radioactivity is shown on the right of figure 3.5 when considering a realistic MR-ToF design. The improvement factor range from 30 to a few hundreds depending on the nuclides mass and half-life. Figure 3.5 also illustrates some of the first science cases to be addressed by MIRACLS.

3.3.1 First science cases of MIRACLS

The MIRACLS approach will offer new opportunities to explore regions in the nuclear chart which are unreachable with conventional CLS. Among those, very exotic Cd isotopes represent one of the first science case of MIRACLS. The rms nuclear charge radii for cadmium (Cd) isotopes between mass number A=100 and A=130 have been successfully obtained by employing conventional CLS at COLLAPS beamline at ISOLDE/CERN [80]. However, the lower production yields of the isotopes ^{98,99,131,132}Cd demand for methods with higher sensitivity. To this end, it is planned to take advantage of MIRACLS's enhanced experimental sensitivity and perform CLS beyond the N=50 and N=82 neutron shell closure with the goal to extend the laser spectroscopy work on Cd isotopes performed at COLLAPS.
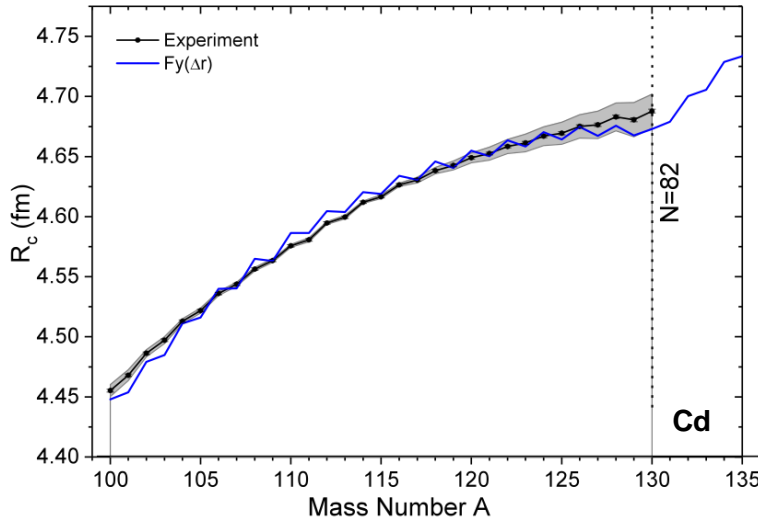

Figure 3.6: Rms nuclear charge radii R_c fro Cd isotopes. The experimental values which obtained at COLLAPS are compared with the results of density functional theory employing the Fayans functional Fy(Δ r) [80].

As shown in figure 3.6, the experimental charge radii of Cd isotopes are compared with the results of Fayans density functional theory (DFT) [81]. Taking into account that the latter has been optimised for Ca isotopes [29, 82], it is remarkable how well the nuclear charge radii of Cd are reproduced in DFT. The Fayans functional predicts a kink at the shell closure N=82 in the Cd isotopes but the experimental results from previous measurements could not reach nuclides beyond N=82. Therefore, the investigation of more neutron-rich Cd isotopes will establish whether such a kink exists at the N=82 shell-closure. Moreover, if observed, its experimentally determined size will serve to benchmark the quality of the Fayans DFT prediction.

Other important nuclear observables which are accessible via CLS are the nuclear spins and the electromagnetic moments. For ^{99,131}Cd, the nuclear magnetic dipole moment μ and the electric quadrupole moment Q are not experimentally known. A simple linear trend over mass number in the electromagnetic moments for their 5/2 ground states is expected from the study of the neutron-deficient ^{101,109}Cd isotopes [83]. However, the shell model calculations of the quadrupole moment in ^{99}Cd results in a value which appears to deviate from this expected linearity. For that reason, a first CLS measurement of ^{99}Cd will allow to investigate whether the linearity is present in ^{99}Cd in contrast to the shell-model predictions. Analogously, the electromagnetic moments of ^{131}Cd will shed new light on the nuclear structure beyond the N = 82 shell closure.
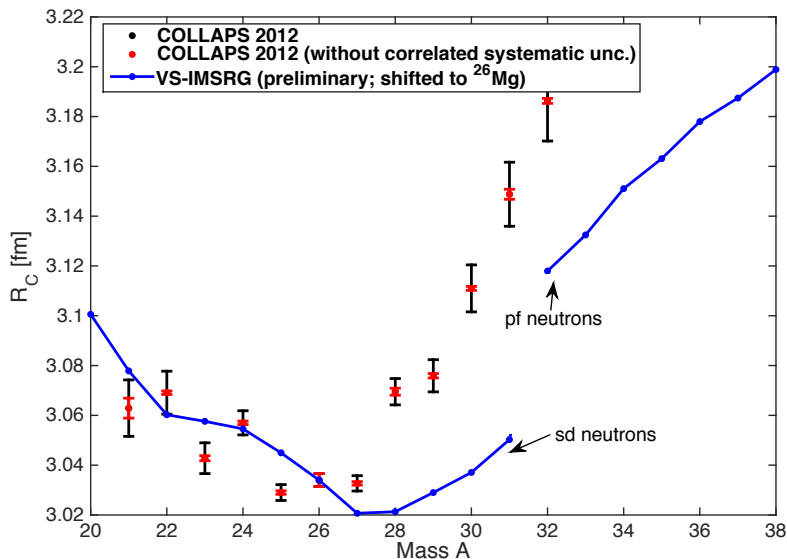
Figure 3.7: Experimental nuclear rms charge radii of magnesium isotopes in [84] compared to preliminary results of VS-IMSRG [85]. The latter are shifted by a constant offset of 0.155 fm to match the experimental value of 26Mg.

Another interesting science case that can be addressed by MIRACLS are the charge radii of exotic magnesium (Mg) isotopes (Z=12). Similarly to the neutron-rich and neutron-deficient cadmium isotopes, the low productions yields of exotic Mg isotopes do not allow their study with conventional CLS due to its limited experimental sensitivity.

Nuclear charge radii of $^{21-32}$Mg isotopes have been measured at COLLAPS. As displayed in figure 3.7, between the A=21-26 and A=26-30, the charge radii follow fairly linear trends in addition to a well-known odd-even staggering. Ab initio methods, like VS-IMSRG [85], are currently under development in order to calculate the charge radii along the entire Mg isotopic chain. For Mg charge radii, some preliminary results from VS-IMSRG are depicted in figure 3.7. The large discontinuity which is observed near N=20 are to be expected and explained by the nonphysical artifacts due to the calculation by employing sd neutrons for N<20 and pf neutrons for N>20. Above ^{32}Mg and all within the pf neutrons valence space, VS-IMSRG predicts a linear trend in the charge radii which is in agreement with the expectations from the experimental results. On the neutron-deficient side of the isotopic chain, the preliminary VS-IMSRG prediction yields a large radius compared to the neighbouring Mg isotopes based on the expectations from the experimental data.

Hence, the determination of the nuclear charge radii of ^{20,33,34}Mg will evaluate the predictive power of leading ab-initio methods spanning from the N = 8 shell closure in close proximity to the proton-drip line to neutron-rich nuclides, right in the centre of the island of inversion.

Before these intriguing and ambitious science goals can be addressed, it will be important to demonstrate the feasibility of the MIRACLS concept experimentally. To this end, a proof-of-principle (PoP) apparatus has been set up around an MR-ToF device [2] operating at a beam energy of ≈2 keV. As part of the present work, this apparatus was modified for the purpose of CLS. The goal of the PoP setup is to demonstrate the functionality of the novel MIRACLS technique, to investigate the spectroscopic lineshape and to benchmark the simulation approach of the future 30 keV MR-ToF device [5]. Moreover, the accuracy of the PoP setup has been studied by measuring the well known isotope shift of stable Mg isotopes. More details about the PoP experiment will be given in the following chapter 4.

4 MIRACLS' Proof-of-Principle (PoP) Experiment

The MIRACLS proof-of-principle (PoP) apparatus, operating at around 2 keV beam energy, has been assembled at CERN ISOLDE around a low-energy MR-ToF device from the University of Greifswald [2] which was modified for the purpose of CLS. The goal of the resulting setup is to demonstrate the MIRACLS concept, to investigate spectroscopic line shape and to benchmark simulations that are employed to design a future device operating at 30 keV [3–5]. This beam energy is essential to minimize Doppler broadening and, hence, to reach the high resolution of the conventional CLS technique.

4.1 Proof-of-principle experimental setup

Details of the proof-of-principle setup are shown in figure 4.1. The ion beam is formed in an offline magnesium (Mg) or calcium (Ca) ion source depending on the studied case. For studies with stable Mg isotopes, a continuous ion beam of $^{24-26}$Mg$^+$ ions is provided by an electron-impact ionization source (adapted from [86]), which is typically floated to $\approx$250 V. In the case of Ca ions, a surface ionization source is used.

The ions are continuously injected into a helium-filled linear Paul trap which allows for beam accumulation, bunching and cooling. After their release from the Paul trap, the ion bunch is accelerated by crown-shaped acceleration electrodes towards a pulsed drift tube (Lift1).When the ions are in the center of this drift tube, its initial potential of $\approx$-2080 eV is rapidly switched to ground potential without being noticed by the ions. Hence, the ions leave the pulsed drift tube with an energy of $\approx$2.3 keV. The ion bunch is subsequently deflected by a 90° quadrupole bender onto the optical axis of the MR-ToF device. A retractable MagneToF detector is installed in front of the MR-ToF device for beam diagnostics. Inside the MR-ToF instrument, the ions are trapped for several revolutions between the two sets of electrostatic mirrors. Capturing the ion bunch into the MR-ToF device is achieved by the in-trap lift technique in which the electric potentials of the mirror electrodes are kept constant at all times [2,73] (see chapter 3.2). The in-trap lift mechanism is also used to eject the ions from the MR-ToF device and guide them to a second retractable MagneToF detector for beam diagnostics and beam-tuning purposes [2,73].

For CLS measurements, optical access to the MR-ToF device is required such that the laser light is guided into the apparatus with the goal to resonantly excite the trapped ions. For this reason, the laser beam enters and exits the set-up through a, Brewster-angled quartz window to minimize laser scattering inside the apparatus and as a result the background rate in the CLS measurement.

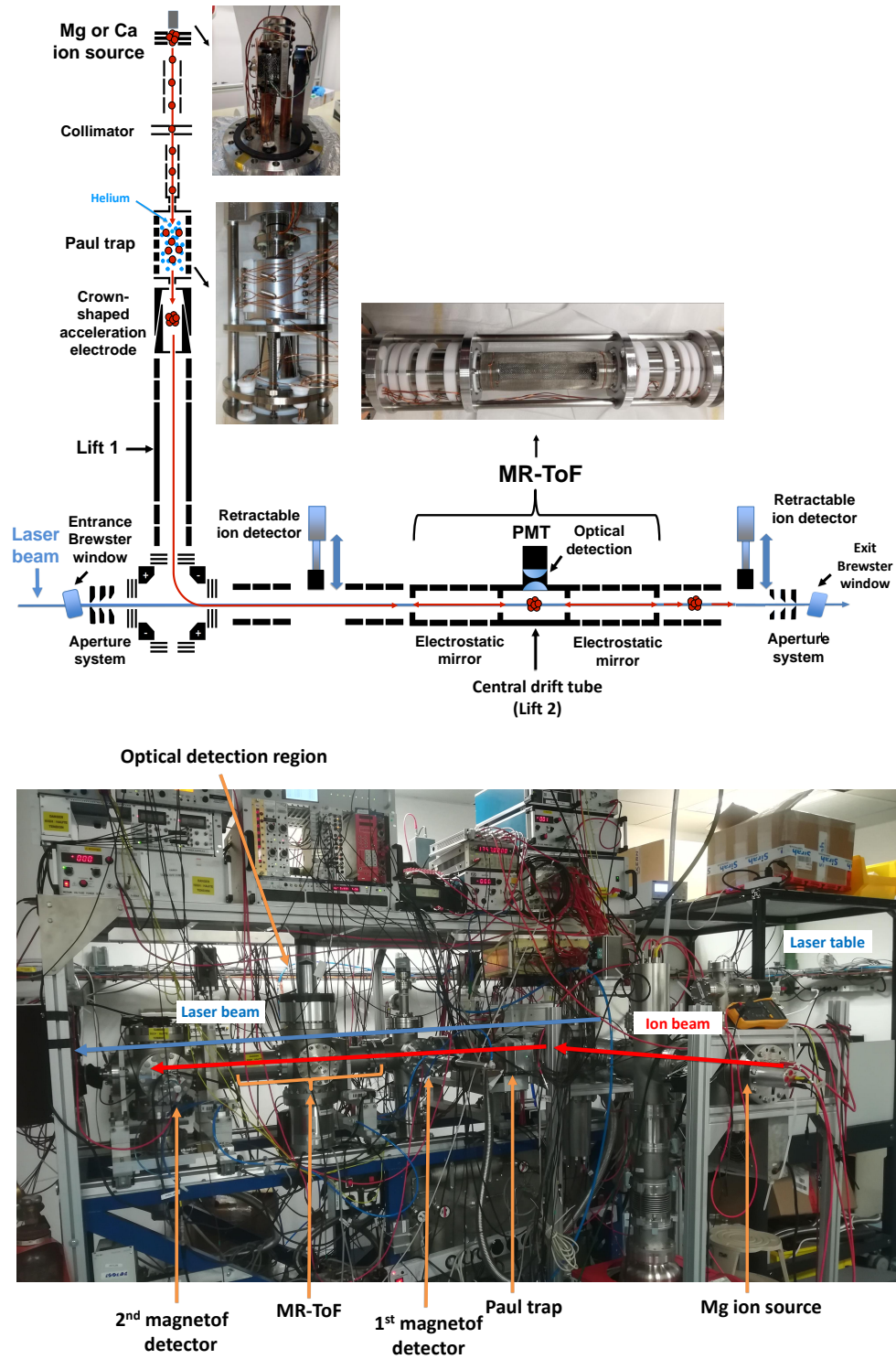For the detection of fluorescence photons emitted by laser-excited Mg$^+$ ions, an optical

Figure 4.1: *Top*: Schematic drawing of the modified MIRACLS' proof-of-principle setup. In the inserts the Mg ions source, the Paul trap and the MR-ToF device are pictured. *Bottom*: Picture of the setup in the MIRACLS laboratory.

lens system and a PMT, which is based on COLLAPS design [87], are installed above the central drift tube (CDT or Lift2) of the MR-ToF device. A retractable MagneToF detector is placed downstream of the MR-ToF device for monitoring and beam-tuning purposes.

In order to achieve efficient CLS measurements, a series of modifications were carried out along the entire beam line in order to reduce the laser stray light into the PMT which is the main source of background in our CLS work (see chapter 4.1.5.1). In the following, the individual components are discussed in more details.

4.1.1 Mg ion source
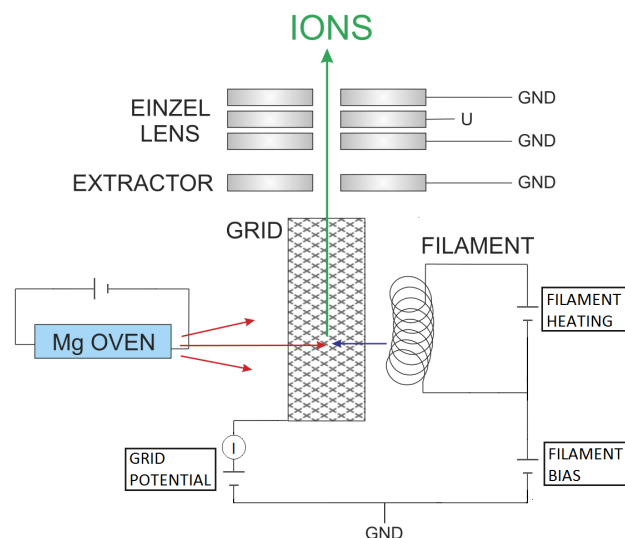
Figure 4.2: Overview of the circuit diagram of the MIRACLS' PoP ion source. The basic design was developed by collaboration partners at GSI and TU Darmstadt [86].

For the first measurements, an offline electron impact ion source (see figure 4.2) was selected which produces stable $^{24-26}$Mg$^+$ ions with the natural abundances of 78.99%, 10.00%, and 11.01% respectively [88]. The even-even isotopes, ^{24,26}Mg$^+$, constitute well suited test cases since as already mentioned (see section 2.2.1), they exhibit a closed two-level system in their D1 and D2 transitions. Hence, laser-excited ions decay back into their initial state.

To produce the necessary vapor pressure an oven with the respective element resistively heated. In the present case the neutral Mg atoms are directed to the ionisation area. For the ionization of Mg atoms, electrons are emitted by a thoriated tungsten filament heated to provoke thermionic emission of electrons. They enter the ionization region through a metallic grid which is held at a potential of $U_{Grid} = 250$ V. Singly charged Mg$^+$ ions are formed by electron impact ionisation. Hence, the energy of the electrons is selected to be close to the maximum in the respective cross section. The grid defines the initial ion beam energy $\approx$250 eV. A field gradient at the ionization region, achieved

by an extraction electrode, drags the ions out of the source. The continuous beam of Mg^+ ions is spatially focused by an einzel lens.

4.1.2 Paul trap

The ion beam is cooled, accumulated and bunched in a linear Paul trap. It consists of four segmented rods. Each rod is composed of five segments to form the axial trapping potential. The radial confinement is accomplished with an RF field of frequency 1.997 MHz. The Paul trap is enclosed in a cylinder with two endcap electrodes. The entrance endcap of the trap is held on a constant potential. In contrast exit endcap can be switched between two values for trapping and ejecting of the ions respectively. The Paul trap is filled with helium which thermalises the ions through He-Mg^+ collisions to ambient temperature. The incoming "hot" ions are consequently cooled to the minimum of the axial potential well. A schematic representation of the Paul trap is shown in figure 4.3.

The injection of the ions into the Paul trap can be controlled by a deflection electrode upstream of the ion trap. By switching the potential of this electrode the ion beam from the Mg^+ source is deflected away from the entrance hole into the Paul trap. The period of time during which ions can enter the Paul trap is defined as the *loading time* whereas the time between ion injection (when the injection electrode is closed) and release of the ions from the Paul trap is defined as the *cooling time*.
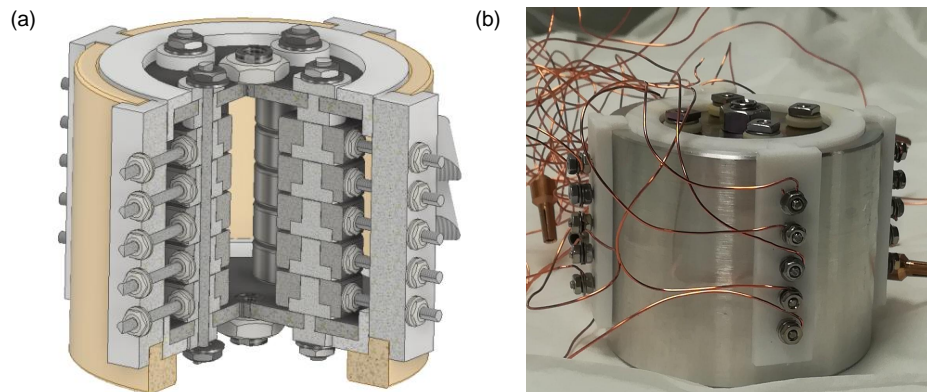
Figure 4.3: (a) 3D section view of the PoP' Paul trap and (b) Photograph of PoP's Paul trap.

4.1.3 MR-ToF device

The MR-ToF device consists of two opposing electrostatic mirror sets which are separated by the central drift tube (CDT). Each electrostatic mirror is composed of four cylindrical electrodes. The central drift tube is made out of two electrodes and a connecting cylindrical, conductive mesh. For an improved photon-detection efficiency, the side of the conductive mesh facing the optical detection region, is replaced by a mesh with higher transparency. When the ions are in the middle of the central drift tube, which serves as a field-free region for the ions, the in-trap lift is switched from some positive
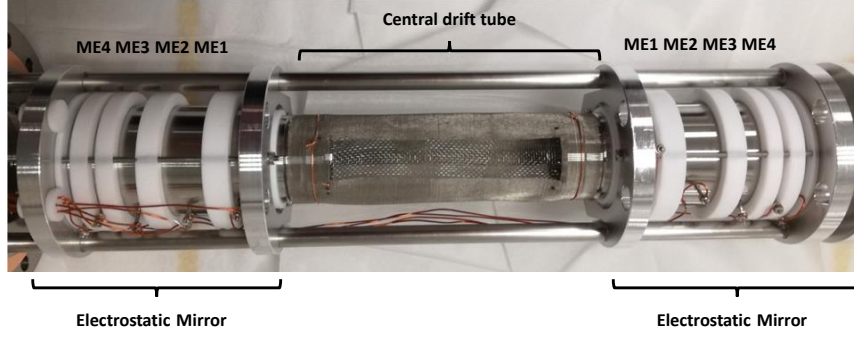
Figure 4.4: Top view of the PoP's MR-ToF device.

value potential U_{CDT} to ground. The kinetic energy E of the ions in the middle of the central drift tube is given by $E \cong e(U_{seg5} - U_{Lift1} - U_{CDT})$ and is smaller than the mirror potentials so that the ions are trapped in between them. For ejection of the ions, the in-trap lift is applied in opposite direction such that the ions can leave the MR-ToF device and finally be detected with the help of a retractable MagneToF detector.

Due to the fact that the ions are reflected between the electrostatic mirrors to prolong their flight path, the performance of the MR-ToF device depends on the stability of the electric potentials applied to the mirror electrodes. In this context, bias voltages of those mirror electrodes at which the ions turn around and are reflected towards the opposite mirror are generally the most important ones. In particular, their voltage sources need to be stable in order to minimize the fluctuations of ions' total time-of-flight. Hence, investigations are underway for the PoP's MR-ToF device in order to increase the short- and long-term stability of suitable voltage supplies for enhanced performance of the apparatus in analogy to recent work in [89].

4.1.4 Control and data acquisition system

The control of the experimental setup (timing sequence, communication with devices, data acquisition) is fully integrated in the "ClusterTrap-CS" from the University of Greifswald [90, 91]. A FPGA card (National Instruments), which is programmed as a pulse-pattern generator, generates the time-sequence signal to control the high voltage switching of the electrode potentials (blocking voltage, endcap of Paul trap, Lift1 and Lift2). Thus, the activation and the deactivation of the switching electrodes are controlled from this FPGA card. A schematic time structure of a measurement cycle is depicted in figure 4.5. The loading time during which ions are injected into the Paul trap, is controlled by a deflection electrode which is to ground potential for ion loading and to 400 V to deflect the ions away from the Paul trap (blocking voltage). Following a cooling time, the ions are ejected from the Paul trap by switching its endcap from $\approx$244 V (trapping) to $\approx$169 V (ion injection).

After the ejection from the Paul trap, the ions are accelerated towards the pulsed drift tube of Lift1. When they reach its middle, the lift is activated by switching the potential of the drift tube from $\approx$-2080 V to ground potential. During some microseconds, the ions travel from the middle of Lift1 to the middle of Lift2 which is switched from $\approx$830 V
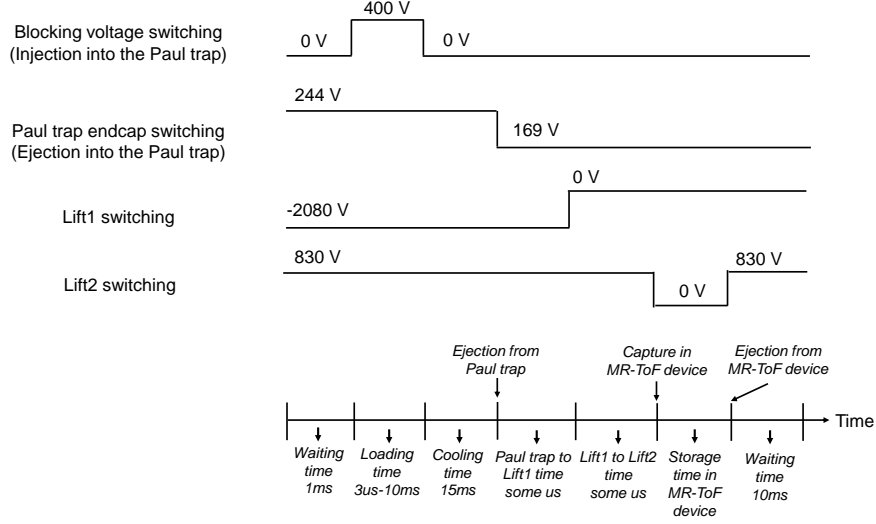
Figure 4.5: Time structure for the experimental measurement cycle.

to ground potential to capture the ions in the MR-ToF device. After a specific number of revolutions i.e. for a defined storage time, the ions are ejected from the MR-ToF device by switching Lift2 from ground back to $\approx$830 V. At the end of the cycle, an additional waiting time is applied which provides the necessary time for the recharging of the capacitors which buffer the high-voltage switchers to provide stable potentials.

After the ejection of the ions from the MR-ToF device they reach a MagneToF detector (model: 14924). The data acquisition for ion counting is performed with a commercial program which uses a 4-GHz Time-of-Flight Multiscaler (P7887 card) for single ion counting and with a picoscope 6000 for a large number of ions per bunch when individual ion hits cannot be resolved in time. The data acquisition is triggering either on the ejection pulse of the Paul trap or of the MR-ToF device.

For the photon detection, a LabView program controls a multi-channel scaler (SRS 430) program, which collects the counts from a photo-multiplier tube and synchronizes the photon-counting with the laser scanning program. This allows one to construct a spectrum of the photon counts versus frequency step.

4.1.5 Laser setup

The photo-excitation of stable Mg^+ ions itself is achieved with a laser beam of $\approx$280 nm wavelength. The fundamental laser light of 560 nm is created by a Sirah Matisse dye laser which is pumped by a Spectra Physics 20-W continues wave diode-pumped solid-state laser (Milennia eV) with a wavelength of 532 nm. The dye laser is operated with Rhodamine 560 dye dissolved in ethylene glycol and has an output power of 0.5 W to 1 W. For the measurement, the control and the stabilization of the wavelength of the dye laser, a wavemeter (WSU-10 by HighFinesse) is employed and it is regularly calibrated using a temperature-stabilised HeNe or alternatively a diode laser which is locked to the hyperfine transition from $5p^2S_{1/2}$ state with F=2 to the $5p^2S_{3/2}$ state with F=3 of ^{87}Rb at approximately 780 nm. The accuracy of the wavemeter according to the
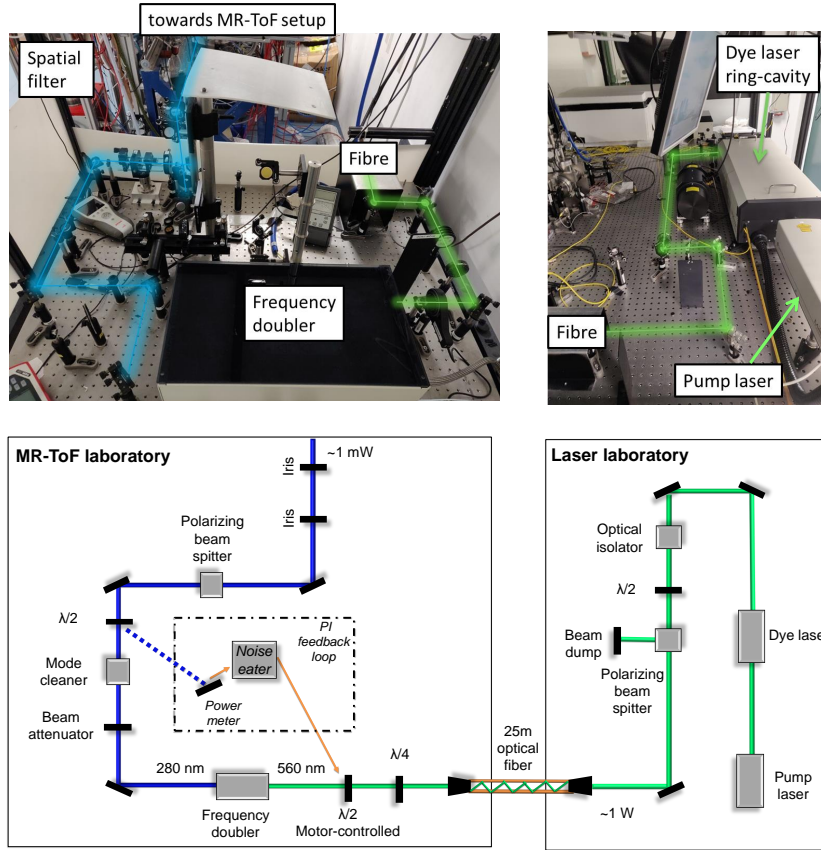
Figure 4.6: Schematic of the laser setup for MIRACLS PoP experiment.

manufacturer is 10 MHz when it is calibrated by a well-known reference within 200 nm or 30 MHz in our case where the well-known reference is more than 200 nm away.

The transportation of the laser light of 560 nm is accomplished by the use of a high-power optical fibre (LMA-15 Single-mode 15 μm core fiber) to the laser table in the MIRACLS lab, where the light is frequency doubled via the Spectra Physics WaveTrain frequency doubler to the wanted 280 nm wavelength. After passing through some beam shaping optics, the laser beam enters the vacuum chamber though a Brewster window. The laser power sent into the MR-ToF setup can be adjusted with a beam attenuator in front of a spatial filter which is used to obtain a pure Gaussian beam profile free of side fringes. An additional stabilization of the power level is taking place by guiding the back reflection of a $\lambda/2$ plate, which is located behind the spatial filter, onto a power meter. Its output is used to rotate a motor-controlled $\lambda/2$ plate in front of the frequency doubler. A picture of the laser path is illustrated in figure 4.6. A more detailed discussion can be found in the thesis article III [4] .

The hyperfine structure of an isotope is recorded as a function of laser frequency. This is achieved by scanning the laser frequency around the Doppler-shifted resonance frequencies in the lab frame f_L calculated from literature values in the ions' rest frame for ^{24}Mg$^+$ and ^{26}Mg$^+$ ions, respectively. In the present study, it is preferred to scan the

laser frequency instead of scanning the ion bunch energy, also called "Doppler tuning", as commonly done in conventional CLS. The latter may change the ion trajectories inside the MR-ToF device, which may influence the CLS line shape and position.

4.1.5.1 Stray-light suppression

The leading source of the photon background is laser stray light, for instance light scattered off components in the beam line. For efficient CLS measurements, these background should be minimized in order to obtain the highest signal-to-noise ratio. In MIRACLS' PoP setup, this minimization was achieved by the installation of two elements, a stray light shielding around the ODR and apertures systems next to the entrance and exit Brewster window. The stray-light shielding, as figure 4.7 illustrates, consists of a cylinder and a plate with a slit mounted inside the cylinder. The fluorescence photons emitted from an ion beam with a radius in the order of 3 mm to 4 mm can still reach the lens while photons coming from other directions are suppressed. On the other hand, the aperture system cuts away the tails of the Gaussian shaped laser beam that could otherwise be scattered on various beamline components. Hence, it aims to block out photons which are geometrically not originating from the ions in the optical detection region. Both aforementioned stray-light suppression elements are coated with photon-absorbing black colour (Tetenal camera varnish spray) to absorb as many photons as possible before they can reach the ORD. More details about the stray-light suppression are given in the thesis article II [92].
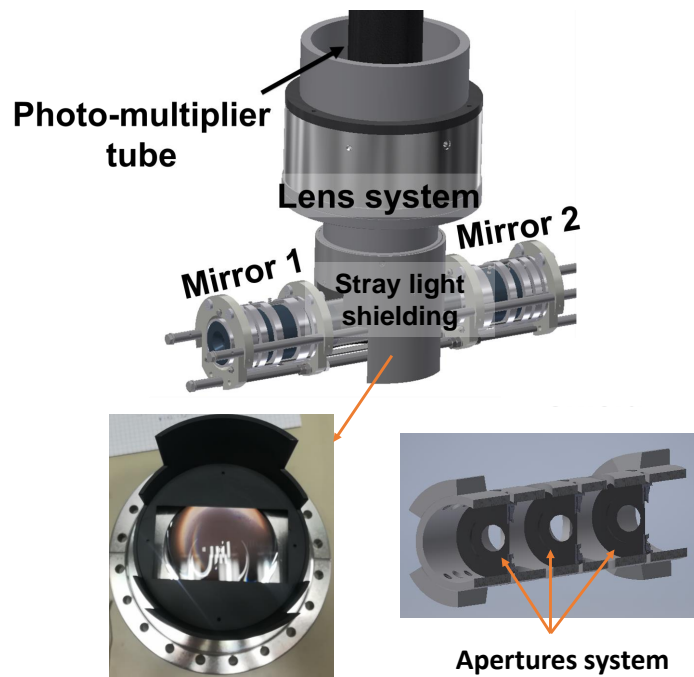
Figure 4.7: Stray-light suppression elements.

4.2 Experimental results

4.2.1 Measurement and Analysis procedure

As a first test-case for the MIRACLS technique, ions of stable magnesium isotopes are selected since the even-even isotopes, ^{24,26}Mg$^+$, have no hyperfine splitting of the fine-structure levels due to their zero nuclear spin. This results in a closed two-state structure for the $3s^2S_{1/2} \rightarrow 3p^2P_{1/2}$ (D1) and $3s^2S_{1/2} \rightarrow 3p^2P_{3/2}$ (D2) transitions. An excited ion will therefore always decay back into its ground state and no optical pumping to another (hyper-)fine structure state will take place. Hence the same transition can be probed very often while the ions are trapped inside the MR-ToF device.
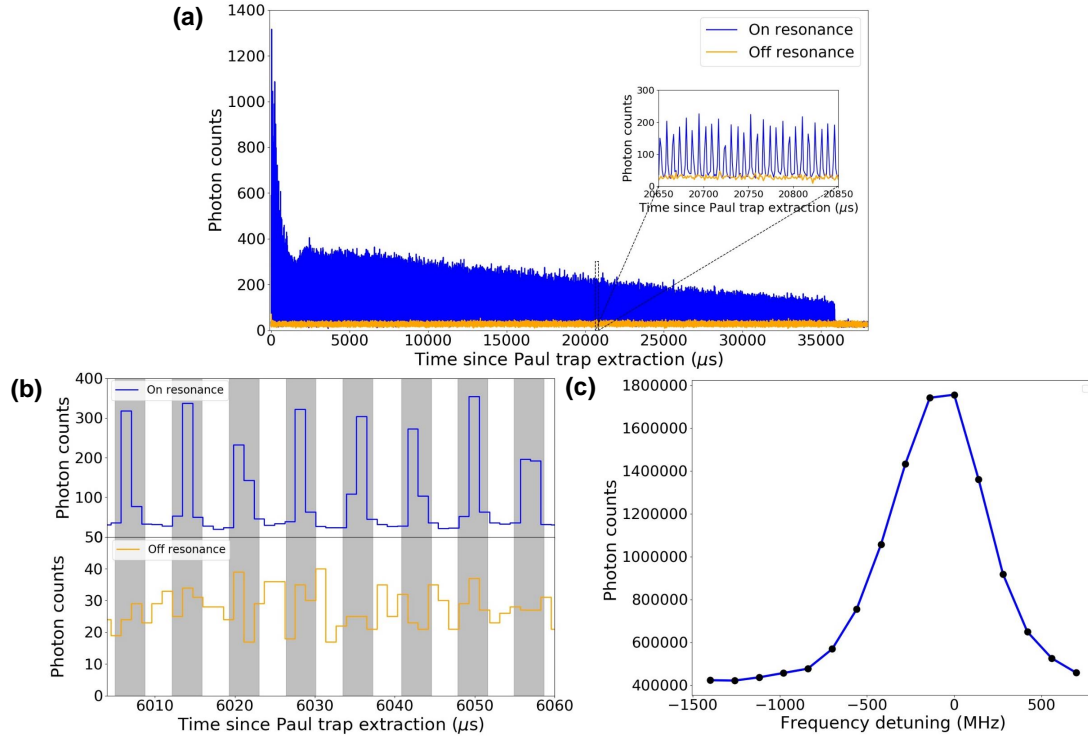
Figure 4.8: (a) Typical spectrum of photons versus time since extraction from the Paul trap while ^{24}Mg$^+$ ions are trapped for 5000 revolutions inside MIRACLS' MR-ToF device. The data for a laser frequency on resonance with the D1 transition is compared to a laser frequency detuned, off-resonance. (b) A zoom on revolution 840 to 847. The grey bands represent examples of the time gates used in the analysis. (c) Resonance spectrum of ^{24}Mg$^+$ ions when integrating the time-gated data over 5000 revolutions. See text for details.

An example of spectrum of photon counts versus time is shown in figure 4.8 (a) where ^{24}Mg$^+$ ions are trapped for up to ∼5000 revolutions inside the MR-ToF device. The corresponding hyperfine (HFS) spectrum, i.e. photon counts versus frequency, is presented in figure 4.8 (c). To obtain such a HFS spectrum, the laser frequency is scanned across the frequency range of interest and for each laser step, the fluorescence

photons are counted as a function of the time since the extraction from the Paul trap.

In figure 4.8 (a), a continuous reduction of the fluorescence signal over the revolution number is observed. This reduction is to a large extend correlated with ion losses which are also observed by detecting the ions on the MagneToF detector located directly after the MR-ToF device (see figure 4.9). One major reason for ion losses is found in collisions with the residual gas particles inside the MR-ToF instrument. In this context, we notice an increased pressure in the MR-ToF vacuum chamber when the Paul trap is filled with He. As a compromise the Paul trap is operated with a He-gas flow which is still sufficient to efficiently cool incoming Mg^+ ions while keeping the pressure in the MR-ToF region low. Another potential reason for losses of the photon rate over time in figure 4.8 (a) may be small instabilities on the mirrors potential which disturb the ion trajectories resulting a non-ideal overlap of the laser and the ion beam.

In the inset of figure 4.8 (a), the photon transient is enlarged in the region of revolution number 3000. For the on-resonance data, the individual peaks correspond to the photon signal when the ion bunch is passing in front of the optical detection region for each revolution inside the MR-ToF device. They are equally spaced with a revolution time of $t_{rev} \approx 7.15 \mu s$. The revolution time depends on the mass-over-charge ratio, beam energy and mirror potentials. The ejection of $^{24}Mg^+$ ions after $\sim$5000 revolutions from the MR-ToF device is clearly notable by the signal disappearance. The hyperfine spectrum in figure 4.8 (c) is extracted by integrating the data from the time gates that are applied for each laser frequency step to the spectrum in figure 4.8 (a), as depicted in figure 4.8 (b). In this case, the resonance spectrum consist of only a single peak because of the absence of a hyperfine splitting for nuclides with spin 0 such as ^{24}Mg. Each resonance is characterised in this by a centroid frequency, a width (FWHM), an intensity above the background.

For the extraction of these parameters, the χ^2-minimization procedure in the SATLAS [93] analysis package is employed during the fitting of the individual spectra. A Gaussian profile is assumed to describe the resonance's line shape since the Doppler broadening is the dominant contributor to the broadening of our spectral linewidth. The photon counts are assumed to follow Poisson statistics, hence, an uncertainty of $N^{1/2}$ is adopted for a measurement of N photons. Since the scatter of the photon numbers actually measured for many of the HFS spectra is large than expected from only Poisson statistics, the uncertainties are increased by a factor that the reduced χ^2 equals 1.

4.2.2 MIRACLS' performance

The main advantage of MIRACLS is the fact that the trapped ions can be probed many times, i.e. once for each revolution inside the MR-ToF device. Thus, the signal strength in the hyperfine spectrum is further increased the more revolutions are integrated. In order to investigate the performance of the current MIRACLS setup, the evolution of the resonance's centroid frequency, the width and the intensity as a function of the revolution number are determined.

Figure 4.9 (a) and (b) show the integrated fluorescence counts and the ion counts over the revolution number per cycle, respectively. Here, each cycle corresponds to one ion bunch extracted from the Paul trap. The reduction in photon intensity over revolution number is linked to the decrease of the ion counts. By comparing figure 4.9 (a) and (b),
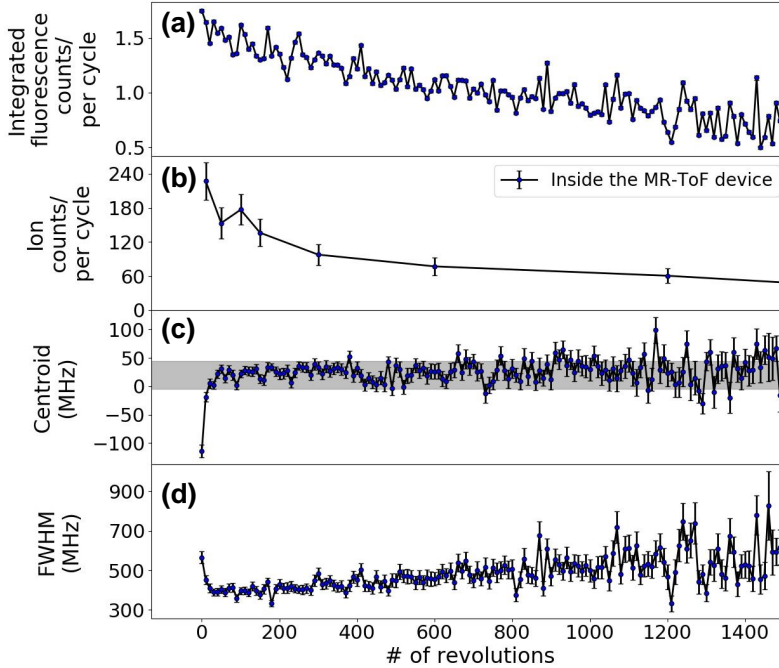
Figure 4.9: Evolution of the area (integrated fluorescence counts) (a), the center (centroid) (c), the width (FWHM) (d) of the resonance peak versus the number of revolutions. For comparison, (b) illustrates the corresponding ion number versus revolution number. The data is based on 1500 measurement cycles for each laser frequency step. The shaded area (c) indicates a frequency interval of 50 MHz. Every point in (a), (c) and (d) arises from a fit to resonance spectrum in which 10 consecutive revolutions were added together. This is the result of the aggregation of the ToF peaks for every 10 revolutions.

however, there is no exact one-to-one relationship. In particular, the initially observed losses in the ion number is larger compared to the losses in fluorescence. This may be due to ions on unstable orbits far away from the central MR-ToF axis. Hence, these ions never interact with the laser beam and get expelled from the MR-ToF during the first tens of revolutions. After 150 revolutions, the decay in fluorescence counts follows closely the one observed in the ion counts.

The evolution of HFS centroid frequency versus the number of revolutions is shown in figure 4.9 (c). After a sharp initial rise up to ~40th revolution the centroid remains constant within 50 MHz band. The initial increase is related to a tail during the high-voltage switching of central drift tube (Lift2). Investigation about the accurate description of the HV-switching process to fully correct for it in the resonance centroids is currently in progress. This topic will be discussed extensively in a upcoming manuscript.

In figure 4.10, an example of fitted HFS spectra, obtained for different revolutions number, are illustrated. From these spectra, one can observe small shifts in the centroid that are also depicted in figure 4.9 (c). Also, the width of the peak (FWHM) has also an increased trend (see figure 4.9 (d)) which is easy visible in figure 4.10 by comparing

3 selected revolutions (150th, 650th and 1150th).
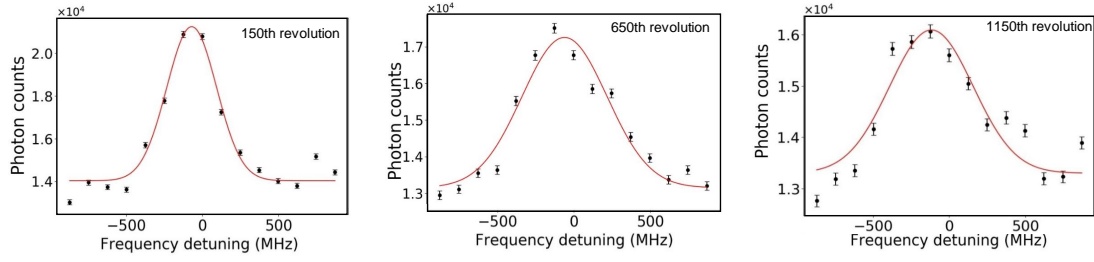
Figure 4.10: Measured resonance spectra of $^{24}Mg^+$ ions in the D2 line for different revolution numbers in MIRACLS' MR-ToF device. The experimental data (in black) is fitted by a Gaussian line shape (in red).

4.2.3 Sensitivity limit

The main goal of the MIRACLS technique is to enhance the sensitivity of fluorescence-based CLS in order to address physics cases that cannot be addresses with the conventional approach today. Figure 4.11 illustrates the experimental signal-to-noise ratio (S/N) attained for different intensities of $^{24}Mg^+$ ions trapped for 1500 revolutions inside the MR-ToF device. The signal-to-noise ratio is calculated by taking into account as signal (S) the amplitude value of the resonance peak and as noise (N) the square root of the background value which are given by the Gaussian fitting of the respective resonance.
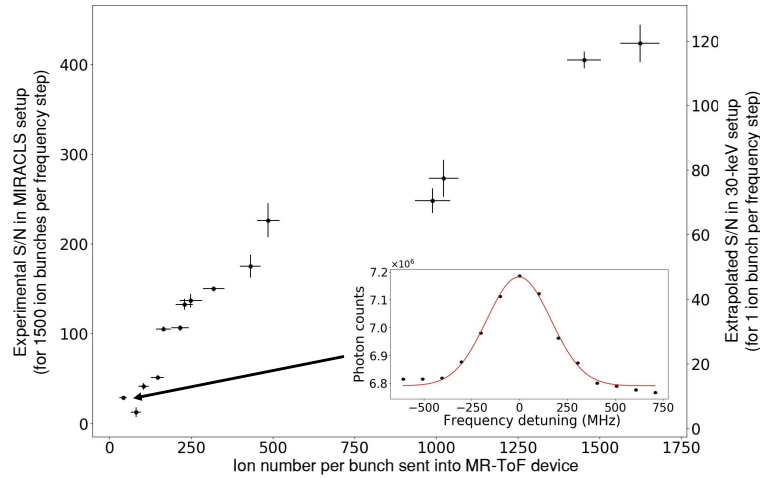
Figure 4.11: Experimental CLS sensitivity expressed in terms of signal-to-noise ratio (S/N) for $^{24}Mg^+$ ions trapped for 1500 revolutions with the MR-ToF proof-of-principle setup. An extrapolation of the sensitivity for the 30-keV apparatus is given on the right y-axis assuming a single ion shot per frequency step. The insert shows a typical resonance for $^{24}Mg^+$ ions.

The uncertainty of each S/N value is extracted by using the error propagation formula, including the covariance term, on the already increase uncertainties of the amplitude

and the background parameters. From up to ∼500 ions injected into the MR-ToF device, the S/N ratio follows a linear increasing trend as expected. The inset of figure 4.11, for instance illustrates a HFS spectrum for 50 ions per bunch which demonstrates that even for very low ion intensities a spectrum of good quality can be attained.

However, for much higher numbers of injected ions, see around ∼1000 and ∼1500 ions per bunch, in figure 4.11, the S/N ratio drops significantly bellow the linear trend observed for lower numbers of stored ions. This is associated with space-charge effects inside the MR-ToF device. Space-charge effects arises due to the Coulomb interaction between the ions which becomes relevant once too many ions are stored simultaneously.

For instance, figure 4.12 shows the stability of the centroid frequency for two different ions numbers. For ∼310 injected ions, the resonance's centroid remains rather stable after the initial rise as discussed in section 4.2.2. However, for ∼880 injected ions, the centroid frequency is not longer constant over revolution number. Instead a very pronounced minimum is observed at revolution ∼600 in the centroid evolution. As a consequence, the resonance of individual revolutions do no longer add up for longer ion numbers. Hence, the signal strength does not increase linearly with ion number anymore, which explains the reduced S/N ratio in figure 4.11 for the highest ion numbers.

On the right axis of figure 4.11, an extrapolation of the sensitivity for the 30-keV setup is given, which is based on the number of photon detectors and the expected reduction in laser-stray light as typically obtained considering an identical optical detection region of COLLAPS. However, it does not include differences in the FWHM of the laser spectroscopic line shape or in the efficiency of ion trapping, storage or laser-excitation in the 30-keV MR-ToF device in which should be more favourable.
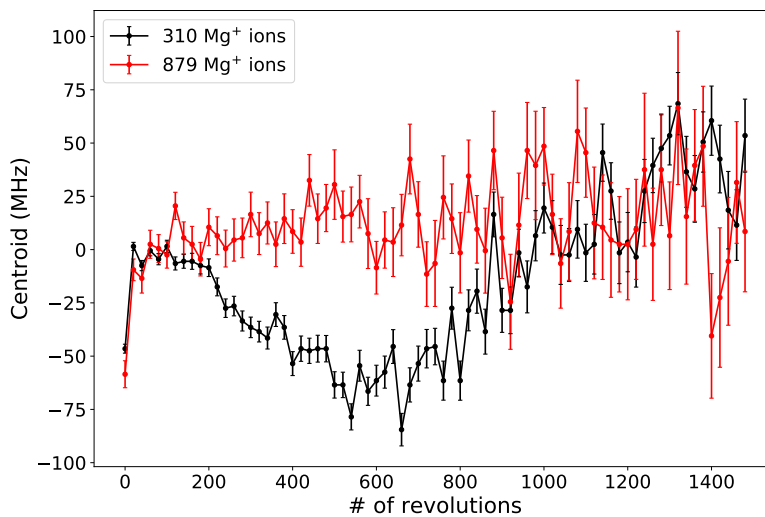
Figure 4.12: CLS centroid frequency over revolution number in the MR-ToF device for two different ion numbers confined in the trap.

4.2.4 Isotope shift measurements

In order to establish the accuracy of MIRACLS technique, the isotope shift between $^{26}Mg^+$ versus $^{24}Mg^+$ was measured in the D2 line. To obtain the HFS spectra of both isotopes from which the isotope shift can be extracted, the laser frequency is scanned over the Doppler-shifted resonance frequencies in the lab frame. In a first step, the isotope shift is determined in conventional single-passage CLS, i.e. without trapping the ions in the MR-ToF device.
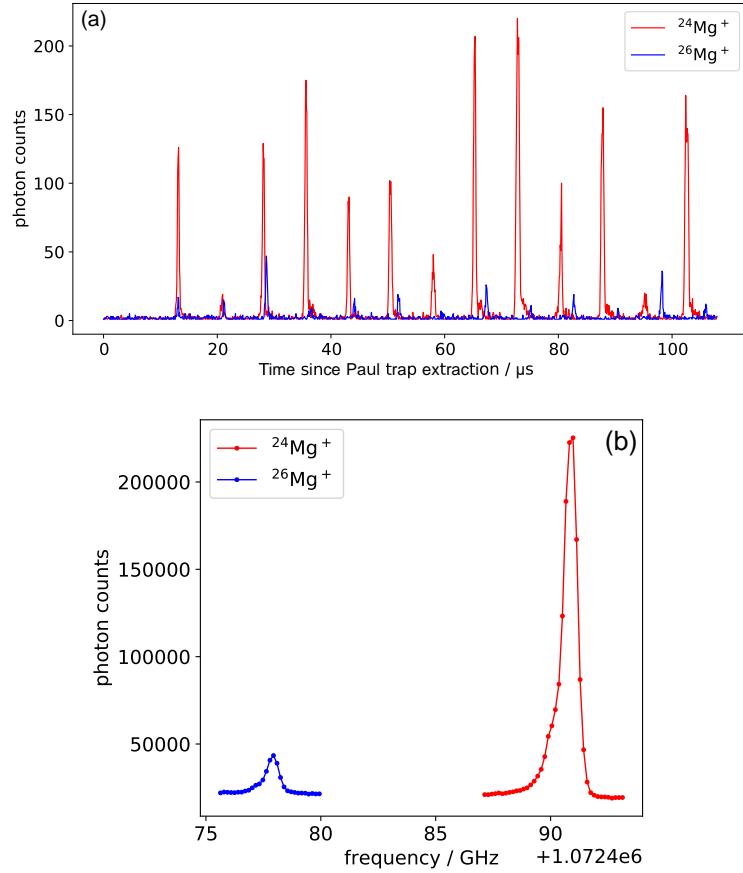
Figure 4.13: (a) Photon counts versus the time since extraction of the ions from the Paul trap for the resonance frequency of $^{24}Mg^+$ and $^{26}Mg^+$ ions (b) Resonance spectra of $^{24}Mg^+$ and $^{26}Mg^+$ ion in the D2 line for the lab-frame laser frequencies.

The purpose of this first measurement campaign is to investigate systematic uncertainties in this particular low-energy CLS setup which are independent of the MR-ToF operation itself. This work is discussed in the thesis article I [94]. In summary, a 20 MHz systematic uncertainty has been identified in this isotope shift which is due to the non-linear inaccuracies in the wavemeter. Moreover, the HV switching of Lift1 and Lift2 may result to actual ion beam energies which are different to the nominal acceleration voltages applied to the respective pulsed-drift tubes. Finally, incomplete

knowledge about the ions' starting potential inside the Paul trap adds to the systematic uncertainty in the isotope shift.

In the second step, the isotope shift is measured in the MIRACLS technique, i.e. when trapping the ions inside the MR-ToF device. The photon counts recorded by the PMT next to the central drift tube as a function of time since the ions' extraction from the Paul trap is shown in figure 4.13 (a). For the respective resonance frequency, the passage of the ions can be seen as a strong increase in the number of detected photons. Due to their different masses, the peaks associated with the passage of ^{24}Mg$^+$ and ^{26}Mg$^+$ ions separate over time. Due to the higher mass of ^{26}Mg$^+$ ions their revolution period inside the MR-TOF device is longer compared to ^{24}Mg$^+$.

An example of isotope shift measurement, which was obtained during the present work, is shown in figure 4.13 (b). It illustrates the resonance of both ^{24}Mg$^+$ and ^{26}Mg$^+$ ions with the respective lab frame frequencies. The latter has to be converted into the ions' rest frame to extract the isotope shift. For this purpose, the kinetic energy of the ions inside the MR-ToF device is attained from the measured acceleration potentials. In particular, the kinetic energy of the ions in the middle of the central drift tube follows the formula $E = e(U_{PT} - U_{Lift1} - U_{Lift2})$ (see chapter 3.2) where all relevant potentials are measured on a regular bases with a precision voltage divider. Based on this kinetic energy, the Doppler-shifted frequency ν in the rest frame of the ions for both isotopes, can be determined from the laser frequency in the lab frame via the expression (see eq.2.27)

$$\nu = \nu_0 \frac{(1 - \beta)}{\sqrt{(1 - \beta^2)}} \tag{4.1}$$
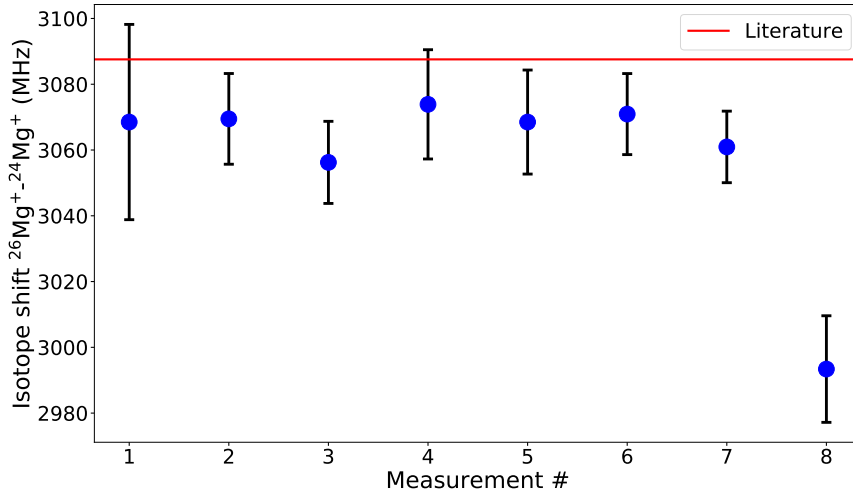
Figure 4.14: Preliminary results for the isotope shift measurements of ^{26}Mg$^+$ versus ^{24}Mg$^+$ in D2 line compared to its more precise determination in [84]. Error bars reflect statistical uncertainties only.

The analysis of all data sets follows the procedures as outlined in the thesis article I [94]. The results are shown in figure 4.14. As can been seen the largest difference from the literature value is ∼90 MHz in one measurement run which is not fully understood. In

addition to the error bars shown, systematic uncertainties have to be considered. These account for 20 MHz for the non-linearities in the wavemeter's performance and 8 MHz for the uncertainty in the ions' starting potential in the Paul trap. Moreover, the impact of the HV-switching of Lift1 and Lift2 need to be evaluated. Preliminary results of this work indicate that the impacts of Lift1 and Lift2 cancel a large extend. Hence, values given here may not be far away from the final mean values in the isotope shifts. Once confirmed, this would validate that the MR-ToF apparatus does not significantly add to the systematic uncertainties, at least relative to the other systematic uncertainties of the present MIRACLS apparatus. These results are preliminary in terms of the influence of the HV switching of the two drift tubes (Lift1 and Lift2) on the ion beam energy. Ongoing work is focused on the accurate measurement of the HV switching process to minimise and then quantify the remaining uncertainties due to this aspect on the measured isotope shift.

4.2.5 MIRACLS beyond closed two-level systems

In order to advance the MIRACLS technique to more general cases, $^{40}\text{Ca}^+$ was selected as the next candidate to performing CLS with the PoP setup. As it is indicated in figure 4.15a (blue curve), trapping $^{40}\text{Ca}^+$ ions for up to 230 revolutions was achieved. However, only the first ≈ 28 revolutions are visible in the fluorescence signal. This is a consequence of optical pumping to a metastable state in Ca^+ ions, see insert of figure 4.15a. However, by using a second laser beam at a wavelength of 866 nm, optical re-pumping from this dark state ($\text{D}_{3/2}$) into the ground state (red curve in figure 4.15a) was accomplished. As a result, all the 230 revolutions were visible in the fluorescence signal until the ions were extracted from the MR-ToF device.
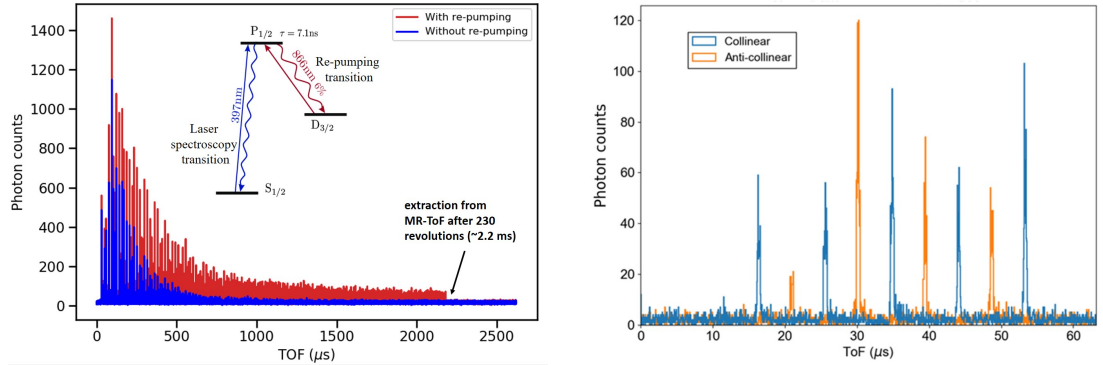
(a) ToF spectrum that indicates the successful optical re-pumping from a dark state into the ground state on $^{40}\text{Ca}^+$.

(b) Collinear-Anticollinear ToF spectrum for trapping $^{40}\text{Ca}^+$ ions for 4 revolutions.

Figure 4.15: Photon count numbers as a function of time from laser excited $^{40}\text{Ca}^+$ ions inside the MR-ToF device.

In addition to the demonstration of the optical re-pumping from a dark state, we also performed collinear-anticollinear spectroscopy on $^{40}\text{Ca}^+$ ions (see figure 4.15b). Ultimately, this may allow one to measure absolute transition frequencies, according to

$\nu_0^2 = \nu_a \cdot \nu_c$, which eliminates the uncertainty due to incomplete knowledge of the ions' beam energy. By using two laser beams, the MIRACLS approach allows to perform collinear CLS along one direction of ion propagation while data in anti-collinear CLS can be recorded in the other flight direction. As a result, the stored radioactive ions can be used even more efficiently.

Such spectra of photons counts versus time for collinear and anticollinear CLS are presented in figure 4.15b for trapping $^{40}\text{Ca}^+$ ions for 4 revolutions inside the MR-ToF device. The two configurations in laser-ion overlap were realised in two separate measurements, but can be readily done simultaneously if two separate laser systems are available.

5 Conclusion and outlook

The **M**ulti **I**on **R**eflection **A**pparatus for **C**ollinear **L**aser **S**pectroscopy (MIRACLS) project is a novel approach for highly sensitive and high-resolution laser spectroscopy of short-lived radionuclides. This is achieved through the combination of the conventional fluorescence-based collinear laser spectrocopy (CLS) and an Multi-Reflection Time-of Flight (MR-ToF) device, well known from mass spectrometry. The latter allows the trapping of fast ion beam in-between its electrostatic mirrors. Hence, ion bunches can be confined for many revolutions during which they are repeatedly probed by a laser beam of appropriate wavelenght. As a result, the experimental sensitivity is enhanced significantly compared to conventional single-passage CLS.

This thesis has presented the general concept of MIRACLS project as well as the experimental results from CLS measurements which have been performed for the first time in an MR-ToF device. As first test case, stable magnesium ions were selected since the closed two-level system in the $3s^2S_{1/2} \rightarrow 3p^2P_{3/2}$ transition of their the even-even isotopes, $^{24,26}Mg^+$, provides the opportunity to probe the same transition as long as the ions are trapped inside the MR-ToF device. This work characterised the MIRACLS performance, especially in terms of experimental sensitivity. Moreover, the well-known isotope shift between the $^{24,26}Mg^+$ isotopes was measured and compared to the literature value to benchmark the accuracy that can be reached with the MIRACLS. Thereinafter, the technique was extended to $^{40}Ca^+$ ions as a first representative of elements which did not exhibit a spectroscopy closed two-levels system. This aspect of the present work constitutes the first step to expand the MIRACLS technique to more general ionic transitions.

While the current work exploited an MR-ToF device operated with a few keV beam energy, the ultimate goal of the MIRACLS project is to develop a high resolution MR-ToF device that confines ion bunches at 30 keV. This will minimize the Doppler broadening such that the spectral linewidth is comparable to the natural linewidth. At this time, simulations and preparations are in final stage to construct such a 30 keV MR-ToF device at ISOLDE/CERN. Additionally, design of a cryogenic Paul Trap is in progress which will provide optimal beam preparation in the future 30-keV setup. In particular, it will allow the reduction of the longitudinal emittance in CLS, i.e. a simultaneous decrease of energy spread and temporal bunch width. Furthermore, developments are ongoing towards versatile UHV compatible and highly UV absorbing coatings for more advanced stray-light suppression for the 30 keV MR-ToF device compare to the PoP one.

The apparatus of the present work is currently upgraded in order to increase the short- and long-term stability of the power supplies which provide voltage to the mirror electrodes. Small fluctuations in the mirror's voltage can distort the total flight time and the ions trajectories in general so it is essential to keep them as stable as possible. In parallel, work has begun to explore the feasibility of the photo-detachment spectroscopy

of negative ions in this setup. Once demonstrated, this collaborative effort between MIRACLS and GANDALPH (see chapter 2.2) opens the path for high-sensitivity and higher resolution in the determination of the electron affinity of chemical elements.

In summary, this works has successfully demonstrated a new technique for collinear laser spectroscopy. Our results establish MIRACLS as a next-generation technique for high resolution and high sensitivity laser spectroscopy. Amongst other, this opens a path to access "exotic" short-lived isotopes, currently out of experiments reach. This will allow to guide and benchmark modern nuclear theory in its quest to describe all atomic nuclei across the nuclear chart from first principles.

6 Bibliography

[1] S.L. Kaufman. High-resolution laser spectroscopy in fast beams. *Optics Communications*, 17(3):309–312, 1976. URL: https://www.sciencedirect.com/science/article/pii/0030401876902674, doi:https://doi.org/10.1016/0030-4018(76)90267-4.

[2] M. Rosenbusch, S. Kemnitz, R. Schneider, L. Schweikhard, R. Tschiersch, and R. N. Wolf. Towards systematic investigations of space-charge phenomena in multi-reflection ion traps. *AIP Conference Proceedings*, 1521(1):53–62, 2013. URL: https://aip.scitation.org/doi/abs/10.1063/1.4796061, arXiv:https://aip.scitation.org/doi/pdf/10.1063/1.4796061, doi:10.1063/1.4796061.

[3] Lechner S., Fischer P., and Heylen H. et al. Fluorescence detection as a new diagnostics tool for electrostatic ion beam traps. *Hyperfine Interact.*, 240(1):95, 2019. URL: https://doi.org/10.1007/s10751-019-1628-1.

[4] S. Sels, P. Fischer, H. Heylen, V. Lagaki, S. Lechner, F. M. Maier, P. Plattner, M. Rosenbusch, F. Wienholtz, R. N. Wolf, W. Nörtershäuser, L. Schweikhard, and S. Malbrunot-Ettenauer. First steps in the development of the Multi Ion Reflection Apparatus for Collinear Laser Spectroscopy (in press). *Nucl. Instrum. Meth. B*, 2019. doi:10.1016/j.nimb.2019.04.076.

[5] F. M. Maier, P. Fischer, H. Heylen, V. Lagaki, S. Lechner, P. Plattner, S. Sels, F. Wienholtz, W. Nörtershäuser, L. Schweikhard, and S. Malbrunot-Ettenauer. Simulations of a proof-of-principle experiment for collinear laser spectroscopy within a multi-reflection time-of-flight device. *Hyperfine Interact.*, 240(1):54, 2019. doi:10.1007/s10751-019-1575-x.

[6] K. Blaum, J. Dilling, and W. Nörtershäuser. Precision atomic physics techniques for nuclear physics with radioactivebeams. *Phys. Scripta*, T152:014017, 2013. doi:10.1088/0031-8949/2013/t152/014017.

[7] P. Campbell, I. D. Moore, and M. R. Pearson. Laser spectroscopy for nuclear structure physics. *Prog. Part. Nucl. Phys.*, 86:127–180, 2016. doi:10.1016/j.ppnp.2015.09.003.

[8] M. L. Bissell K. Blaum B. Cheal K. T. Flanagan G. Neyens W. Nörtershäuser R. Neugart, J. Billowes and D. T. Yordanov. Collinear laser spectroscopy at ISOLDE: new methods and highlights. *J. Phys. G*, 44(6):064002, 2017. doi:https://doi.org/10.1088/1361-6471/aa6642.

[9] R Catherall, W Andreazza, M Breitenfeldt, A Dorsival, G JFocker, T P Gharsa, Giles T J, J-L Grenard, F Locci, P Martins, SMarzari, J Schipper, A Shornikov, and T Stora. The ISOLDE facility. *Journal of Physics G: Nuclear and Particle Physics*, 44(9):094002, aug 2017. URL: https://doi.org/10.1088%2F1361-6471%2Faa7eba, doi:10.1088/1361-6471/aa7eba.

[10] C.J. Foot. *Atomic Physics*. OUP Oxford, 1st edition, 2005.

[11] P. Smith. C. Heise J.R. Esmond R.L.Kurucz. Atomic spectral line database. URL: https://www.cfa.harvard.edu/amp/ampdata/kurucz23/sekur.html.

[12] Deyan Todorov Yordanov. From ^{27}Mg to ^{33}Mg : transition to the Island of inversion. *Ph.D. thesis*, Johannes Kepler University Linz, 2019.

[13] D. G. Ravenhall. Electron scattering and nuclear charge distributions. *Reviews of Modern Physics*, 30:430438, 1958. URL: https://journals.aps.org/rmp/pdf/10.1103/RevModPhys.30.430, doi:10.1103/RevModPhys.30.430.

[14] Robert Hofstadter. The electron-scattering method and its application to the structure of nuclei and nucleons. *Nobel Lecture*, 1961. URL: https://www.nobelprize.org/prizes/physics/1961/hofstadter/lecture/.

[15] Robert Hofstadter. High-Energy Electron Scattering and Nuclear Structure Determinations. *Phys.Rev.*, 92:978, 1953. doi:10.1103/PhysRev.92.978.

[16] S Schmidt, M Willig, J Haack, R Horn, A Adamczak, M AbdouAhmed, F D Amaro, P Amaro, F Biraben, P Carvalho, T-L Chen, L M PFernandes, T Graf, M Guerra, T W Hänsch, M Hildebrandt, Y-C Huang andP Indelicato, L Julien, K Kirch, A Knecht, F Kottmann, J J Krauth andY W Liu, J Machado, M Marszalek, C M B Monteiro, F Nez, J Nuber, DN Patel, E Rapisarda, J M F dos Santos, J P Santos, P A O C Silva, LSinkunaite, J-T Shy, K Schuhmann, I Schulthess, D Taqqu, J F C AVeloso, L-B Wang, M Zeyen, A Antognini, and R Pohl. The next generation of laser spectroscopy experiments using light muonic atoms. *Journal of Physics: Conference Series*, 1138:012010, nov 2018. URL: https://doi.org/10.1088%2F1742-6596%2F1138%2F1%2F012010, doi:10.1088/1742-6596/1138/1/012010.

[17] Adamczak, A., Antognini, A., Berger, N., Cocolios, T.E.and Dressler, R., Eggenberger, A., Eichler, R., Indelicato, P. andJungmann, K., Kirch, K., Knecht, A., Papa, A., Pohl, R. andPospelov, M., Rapisarda, E., Reiter, P., Ritjoho, N., Roccia,S., Severijns, N., Skawran, A., Wauters, F., and Willmann, L. Nuclear structure with radioactive muonic atoms. *EPJ Web Conf.*, 193:04014, 2018. doi:10.1051/epjconf/201819304014.

[18] Knecht, A., Skawran, A., and Vogiatzi, S.M. Study of nuclear properties with muonic atoms. *Eur. Phys. J. Plus*, 135:777, 2020. URL: https://doi.org/10.1140/epjp/s13360-020-00777-y.

[19] G. Fricke and K. Heilig. *Nuclear charge radii*. Springer, Berlin, Heidelberg, 2004.

[20] Fundamental physics constants. Accessed: 2019-06-07. URL: https://physics.nist.gov/cuu/constants/index.html.

[21] Carlos A. Bertulani. *Nuclear Physics in a Nutshell*. Princeton University Press, stu - student edition edition, 2007. URL: http://www.jstor.org/stable/j.ctt7shsk.

[22] Kris L. G. Heyde. *The Nuclear Shell Model*. Springer, Berlin, Heidelberg, study edition edition, 1994. URL: https://doi.org/10.1007/978-3-642-79052-2k.

[23] Khairi Abdullah. *FUNDAMENTALS IN NUCLEAR PHYSICS*. 12 2014.

[24] G. Neyens. Nuclear magnetic and quadrupole moments for nuclear structure research on exotic nuclei. *Rep. Prog. Phys*, 66:633–689, 04 2003. doi:10.1088/0034-4885/66/4/205.

[25] P Stránský, Alejandro Frank, and Roelof Bijker. On prolate shape predominance in nuclear deformation. *Journal of Physics: Conference Series*, 322:012018, 10 2011. doi:10.1088/1742-6596/322/1/012018.

[26] Neyens G. Neugart R. *Nuclear Moments, Lecture Notes in Physics*, volume II. 2006. doi:10.1007/3-540-33787-3_4.

[27] H. Frånberg, P. Delahaye, J. Billowes, K. Blaum, R. Catherall, F. Duval, O. Gianfrancesco, T. Giles, A. Jokinen, M. Lindroos, D. Lunney, E. Mane, and I. Podadera. Off-line commissioning of the isolde cooler. *Nuclear Instruments and Methods in Physics Research Section B: Beam Interactions with Materials and Atoms*, 266(19):4502 – 4504, 2008. Proceedings of the XVth International Conference on Electromagnetic Isotope Separators and Techniques Related to their Applications. URL: http://www.sciencedirect.com/science/article/pii/S0168583X08007647, doi:https://doi.org/10.1016/j.nimb.2008.05.097.

[28] Billowes J. Blaum K. et al. Mané, E. An ion cooler-buncher for high-sensitivity collinear laser spectroscopy at ISOLDE. *Eur. Phys. J.*, A 42:503507, 2009. doi:10.1140/epja/i2009-10828-0.

[29] R. F. Garcia Ruiz, M. L. Bissell, K. Blaum, A. Ekström, N. Frömmgen, G. Hagen, M. Hammen, K. Hebeler, J. D. Holt, G. R. Jansen, M. Kowalska, K. Kreim, W. Nazarewicz, R. Neugart, G. Neyens, W. Nörtershäuser, T. Papenbrock, J. Papuga, A. Schwenk, J. Simonis, K. A. Wendt, and D. T. Yordanov. Unexpectedly large charge radii of neutron-rich calcium isotopes. *Nature Physics*, 12(6):594–598, 2016. doi:10.1038/nphys3645.

[30] Á. Koszor s, J. Billowes, C.L. Binnersley, M.L. Bissell, T.E. Cocolios, B.S. Cooper, R.P. de Groote, G.J. Farooq-Smith, V.N. Fedosseev, K.T. Flanagan, S. Franchoo, R.F. Garcia Ruiz, W. Gins, K.M. Lynch, G. Neyens, F.P. Gustafsson, C. Ricketts, H.H. Stroke, A. Vernon, S.G. Wilkins, and X.F. Yang. Resonance ionization schemes for high resolution and high efficiency studies of exotic nuclei at the cris experiment. *Nuclear Instruments and Methods in Physics Research Section B: Beam Interactions with Materials and Atoms*, 463:398 – 402, 2020. URL: http://www.

sciencedirect.com/science/article/pii/S0168583X19302277, doi:https://doi.org/10.1016/j.nimb.2019.04.043.

[31] Valentin Fedosseev, Katerina Chrysalidis, Thomas Day Goodacre, Bruce Marsh, Sebastian Rothe, Christoph Seiffert, and Klaus Wendt. Ion beam production and study of radioactive isotopes with the laser ion source at ISOLDE. *Journal of Physics G: Nuclear and Particle Physics*, 44(8):084006, jul 2017. doi:10.1088/1361-6471/aa78e0.

[32] G.D. Alkhazov, A.E. Barzakh, V.P. Denisov, K.A. Mezilev, Yu.N. Novikov, V.N. Panteleyev, A.V. Popov, E.P. Sudentas, V.S. Letokhov, V.I. Mishin, V.N. Fedoseyev, S.V. Andreyev, D.S. Vedeneyev, and A.D. Zyuzikov. A new highly efficient method of atomic spectroscopy for nuclides far from stability. *Nuclear Instruments and Methods in Physics Research Section B: Beam Interactions with Materials and Atoms*, 69(4):517 – 520, 1992. URL: http://www.sciencedirect.com/science/article/pii/0168583X9295309F, doi:https://doi.org/10.1016/0168-583X(92)95309-F.

[33] B. A. et al. March. Characterization of the shape-staggering effect in mercury nuclei. *Nature Physics*, 14.

[34] B.A. Marsh, B. Andel, A.N. Andreyev, S. Antalic, D. Atanasov, A.E. Barzakh, B. Bastin, Ch. Borgmann, L. Capponi, T.E. Cocolios, T. Day Goodacre, M. Dehairs, X. Derkx, H. De Witte, D.V. Fedorov, V.N. Fedosseev, G.J. Focker, D.A. Fink, K.T. Flanagan, S. Franchoo, L. Ghys, M. Huyse, N. Imai, Z. Kalaninova, U. Köster, S. Kreim, N. Kesteloot, Yu. Kudryavtsev, J. Lane, N. Lecesne, V. Liberati, D. Lunney, K.M. Lynch, V. Manea, P.L. Molkanov, T. Nicol, D. Pauwels, L. Popescu, D. Radulov, E. Rapisarda, M. Rosenbusch, R.E. Rossel, S. Rothe, L. Schweikhard, M.D. Seliverstov, S. Sels, A.M. Sjödin, V. Truesdale, C. Van Beveren, P. Van Duppen, K. Wendt, F. Wienholtz, R.N. Wolf, and S.G. Zemlyanoy. New developments of the in-source spectroscopy method at rilis/isolde. *Nuclear Instruments and Methods in Physics Research Section B: Beam Interactions with Materials and Atoms*, 317:550 – 556, 2013. XVIth International Conference on ElectroMagnetic Isotope Separators and Techniques Related to their Applications, December 2–7, 2012 at Matsue, Japan. URL: http://www.sciencedirect.com/science/article/pii/S0168583X13008914, doi:https://doi.org/10.1016/j.nimb.2013.07.070.

[35] David J Pegg. Structure and dynamics of negative ions. *Reports on Progress in Physics*, 67(6):857–905, may 2004. doi:10.1088/0034-4885/67/6/r02.

[36] D. Leimbach, S. Rothe, L. Bengtsson, A. Ringvall-Moberg, J. Sundberg, K. Wendt, and D. Hanstorp. Upgrades of the GANDALPH photodetachment detector towards the determination of the electron affinity of astatine. *Nuclear Instruments and Methods in Physics Research Section B: Beam Interactions with Materials and Atoms*, 463:277 – 279, 2020. URL: http://www.sciencedirect.com/science/article/pii/S0168583X19303192, doi:https://doi.org/10.1016/j.nimb.2019.05.015.

[37] Sebastian Rothe, Julia Sundberg, Jakob Welander, Katerina Chrysalidis, Thomas Day Goodacre, Valentin Fedosseev, Spyridon Fiotakis, Oliver Forstner, Reinhard Heinke, Karl Johnston, Tobias Kron, Ulli Köster, Yuan Liu, Bruce Marsh, Annie Ringvall-Moberg, Ralf Erik Rossel, Christoph Seiffert, Dominik Studer, Klaus Wendt, and Dag Hanstorp. Laser photodetachment of radioactive $^{128}I^-$. *Journal of Physics G: Nuclear and Particle Physics*, 44(10):104003, aug 2017. `doi:10.1088/1361-6471/aa80aa`.

[38] H. Wollnik and M. Przewloka. Time-of-flight mass spectrometers with multiply reflected ion trajectories. *International Journal of Mass Spectrometry and Ion Processes*, 96(3):267 – 274, 1990. URL: `http://www.sciencedirect.com/science/article/pii/016811769085127N`, `doi:https://doi.org/10.1016/0168-1176(90)85127-N`.

[39] Wolfgang Demtröder. *Laser Spectroscopy, Basic Concepts and Instrumentation.* Springer, Berlin, Heidelberg, 1996. URL: `https://doi.org/10.1007/978-3-662-08260-7`.

[40] W. Ansbacher, Y. Li, and E.H. Pinnington. Precision lifetime measurement for the 3p levels of mg ii using frequency-doubled laser radiation to excite a fast ion beam. *Physics Letters A*, 139(3):165 – 169, 1989. URL: `http://www.sciencedirect.com/science/article/pii/0375960189903538`, `doi:https://doi.org/10.1016/0375-9601(89)90353-8`.

[41] P.F. Bernath. *Spectra of Atoms and Molecules.* Oxford University Press, 2016. URL: `http://www.chemistry.uoc.gr/lapkin/Bernath_Spectra%20of%20Atoms%20and%20Molecules.pdf`.

[42] S. Knauer, P. Fischer, G. Marx, M. Müller, M. Rosenbusch, B. Schabinger, L. Schweikhard, and R. N. Wolf. A multi-reflection time-of-flight setup for the improvement and development of new methods and the study of atomic clusters. *Int. J. Mass Spectrom.*, 446:116189, 2019. `doi:10.1016/j.ijms.2019.116189`.

[43] Paul Fischer, Gerrit Marx, and Lutz Schweikhard. Multiple ion capture and separation in an electrostatic storage device. *International Journal of Mass Spectrometry*, 435:305 – 314, 2019. URL: `http://www.sciencedirect.com/science/article/pii/S1387380618303208`, `doi:https://doi.org/10.1016/j.ijms.2018.11.010`.

[44] W. Henry Benner. A gated electrostatic ion trap to repetitiously measure the charge and m/z of large electrospray ions. *Analytical Chemistry*, 69(20):4162–4168, 1997. `arXiv:https://doi.org/10.1021/ac970163e`, `doi:10.1021/ac970163e`.

[45] D. Zajfman, O. Heber, L. Vejby-Christensen, I. Ben-Itzhak, M. Rappaport, R. Fishman, and M. Dahan. Electrostatic bottle for long-time storage of fast ion beams. *Phys. Rev. A*, 55:R1577–R1580, Mar 1997. URL: `https://link.aps.org/doi/10.1103/PhysRevA.55.R1577`, `doi:10.1103/PhysRevA.55.R1577`.

[46] H. Wollnik and M. Przewloka. Time-of-flight mass spectrometers with multiply reflected ion trajectories. *Int. J. Mass Spectrom.*, 96(3):267–274, 1990. `doi:10.1016/0168-1176(90)85127-N`.

[47] D. Zajfman, O. Heber, L. Vejby-Christensen, I. Ben-Itzhak, M. Rappaport, R. Fishman, and M. Dahan. Electrostatic bottle for long-time storage of fast ion beams. *Phys. Rev. A*, 55:R1577–R1580, 1997. `doi:10.1103/PhysRevA.55.R1577`.

[48] M. Dahan, R. Fishman, O. Heber, M. Rappaport, N. Altstein, D. Zajfman, and W. J. van der Zande. A new type of electrostatic ion trap for storage of fast ion beams. *Rev. Sci. Instrum.*, 69(1):76–83, 1998. `doi:10.1063/1.1148481`.

[49] Klavs Hansen, Yejun Li, Vladimir Kaydashev, and Ewald Janssens. Thermal radiation of laser heated niobium clusters nb n+, 8 n 22. *The Journal of Chemical Physics*, 141(2):024302, 2014. `arXiv:https://doi.org/10.1063/1.4885364`, `doi:10.1063/1.4885364`.

[50] O. Heber, P. D. Witte, A. Diner, K. G. Bhushan, D. Strasser, Y. Toker, M. L. Rappaport, I. Ben-Itzhak, N. Altstein, D. Schwalm, A. Wolf, and D. Zajfman. Electrostatic ion beam trap for electron collision studies. *Rev. Sci. Instrum.*, 76(1):013104, 2005. `doi:10.1063/1.1832192`.

[51] R. Antoine, T. Doussineau, P. Dugourd, and F. Calvo. Multiphoton dissociation of macromolecular ions at the single-molecule level. *Phys. Rev. A*, 87:013435, 2013. `doi:https://doi.org/10.1103/PhysRevA.87.013435`.

[52] B. Kafle, O. Aviv, V. Chandrasekaran, O. Heber, M. L. Rappaport, H. Rubinstein, D. Schwalm, D. Strasser, and D. Zajfman. Electron detachment and fragmentation of laser-excited rotationally hot Al_4^-. *Phys. Rev. A*, 92:052503, 2015. `doi:10.1103/PhysRevA.92.052503`.

[53] Eric T. Dziekonski, Joshua T. Johnson, Kenneth W. Lee, and Scott A. McLuckey. Determination of collision cross sections using a fourier transform electrostatic linear ion trap mass spectrometer. *Journal of The American Society for Mass Spectrometry*, 29(2):242–250, 2018. `doi:https://doi.org/10.1007/s13361-017-1720-1`.

[54] Y. Ito, P. Schury, M. Wada, S. Naimi, T. Sonoda, H. Mita, F. Arai, A. Takamine, K. Okada, A. Ozawa, and H. Wollnik. Single-reference high-precision mass measurement with a multireflection time-of-flight mass spectrograph. *Phys. Rev. C*, 88:011306, 2013. `doi:https://doi.org/10.1103/PhysRevC.88.011306`.

[55] F. Wienholtz, D. Beck, K. Blaum, Ch Borgmann, M. Breitenfeldt, R. B. Cakirli, S. George, F. Herfurth, J. D. Holt, M. Kowalska, S. Kreim, D. Lunney, V. Manea, J. Menendez, D. Neidherr, M. Rosenbusch, L. Schweikhard, A. Schwenk, J. Simonis, J. Stanja, R. N. Wolf, and K. Zuber. Masses of exotic calcium isotopes pin down nuclear forces. *Nature*, 498(7454):346–349, 2013. `doi:10.1038/nature12226`.

[56] D Atanasov, D Beck, K Blaum, Ch Borgmann, R B Cakirli, T Eronen, S George, F Herfurth, A Herlert, M Kowalska, S Kreim, Yu A Litvinov, D Lunney, V Manea,

D Neidherr, M Rosenbusch, L Schweikhard, F Wienholtz, R N Wolf, and K Zuber. Precision mass measurements of cesium isotopes—new entries in the ISOLTRAP chronicles. *J. Phys. G*, 44(4):044004, 2017.

[57] M. Rosenbusch, P. Ascher, D. Atanasov, C. Barbieri, D. Beck, K. Blaum, Ch. Borgmann, M. Breitenfeldt, R. B. Cakirli, A. Cipollone, S. George, F. Herfurth, M. Kowalska, S. Kreim, D. Lunney, V. Manea, P. Navrátil, D. Neidherr, L. Schweikhard, V. Somà, J. Stanja, F. Wienholtz, R. N. Wolf, and K. Zuber. Probing the $N = 32$ shell closure below the magic proton number $Z = 20$: Mass measurements of the exotic isotopes ^{52,53}K. *Phys. Rev. Lett.*, 114:202501, 2015. doi:10.1103/PhysRevLett.114.202501.

[58] A. de Roubin, D. Atanasov, K. Blaum, S. George, F. Herfurth, D. Kisler, M. Kowalska, S. Kreim, D. Lunney, V. Manea, E. Minaya Ramirez, M. Mougeot, D. Neidherr, M. Rosenbusch, L. Schweikhard, A. Welker, F. Wienholtz, R. N. Wolf, and K. Zuber. Nuclear deformation in the A$\approx$ 100 region: Comparison between new masses and mean-field predictions. *Phys. Rev. C*, 96:014310, 2017. doi:10.1103/PhysRevC.96.014310.

[59] A. Welker, N. A. S. Althubiti, D. Atanasov, K. Blaum, T. E. Cocolios, F. Herfurth, S. Kreim, D. Lunney, V. Manea, M. Mougeot, D. Neidherr, F. Nowacki, A. Poves, M. Rosenbusch, L. Schweikhard, F. Wienholtz, R. N. Wolf, and K. Zuber. Binding energy of ^{79}Cu: Probing the structure of the doubly magic ^{78}Ni from only one proton away. *Phys. Rev. Lett.*, 119:192502, 2017. doi:10.1103/PhysRevLett.119.192502.

[60] M. Mougeot, D. Atanasov, K. Blaum, K. Chrysalidis, T. Day Goodacre, D. Fedorov, V. Fedosseev, S. George, F. Herfurth, J. D. Holt, D. Lunney, V. Manea, B. Marsh, D. Neidherr, M. Rosenbusch, S. Rothe, L. Schweikhard, A. Schwenk, C. Seiffert, J. Simonis, S. R. Stroberg, A. Welker, F. Wienholtz, R. N. Wolf, and K. Zuber. Precision mass measurements of $^{58-63}$Cr: Nuclear collectivity towards the $N = 40$ island of inversion. *Phys. Rev. Lett.*, 120:232501, 2018. doi:https://doi.org/10.1103/PhysRevLett.120.232501.

[61] M. Rosenbusch, Y. Ito, P. Schury, M. Wada, D. Kaji, K. Morimoto, H. Haba, S. Kimura, H. Koura, M. MacCormick, H. Miyatake, J. Y. Moon, K. Morita, I. Murray, T. Niwase, A. Ozawa, M. Reponen, A. Takamine, T. Tanaka, and H. Wollnik. New mass anchor points for neutron-deficient heavy nuclei from direct mass measurements of radium and actinium isotopes. *Phys. Rev. C*, 97:064306, 2018. doi:10.1103/PhysRevC.97.064306.

[62] Beck D. Blaum K. et al. Mukherjee, M. ISOLTRAP: An on-line penning trap for mass spectrometry on short-lived nuclides. *Eur. Phys. J.*, A35:1–29, 2008. doi:https://doi.org/10.1140/epja/i2007-10528-9.

[63] R.N. Wolf, D. Beck, K. Blaum, Ch. Böhm, Ch. Borgmann, M. Breitenfeldt, F. Herfurth, A. Herlert, M. Kowalska, S. Kreim, D. Lunney, S. Naimi, D. Neidherr, M. Rosenbusch, L. Schweikhard, J. Stanja, F. Wienholtz, and K. Zuber. On-line separation of short-lived nuclei by a multi-reflection time-of-flight device. *Nuclear*

Instruments and Methods in Physics Research Section A: Accelerators, Spectrometers, Detectors and Associated Equipment, 686:82 – 90, 2012. URL: http://www.sciencedirect.com/science/article/pii/S016890021200575X, doi:https://doi.org/10.1016/j.nima.2012.05.067.

[64] R. N. Wolf, D. Beck, K. Blaum, Ch. Böhm, Ch. Borgmann, M. Breitenfeldt, N. Chamel, S. Goriely, F. Herfurth, M. Kowalska, S. Kreim, D. Lunney, V. Manea, E. Minaya Ramirez, S. Naimi, D. Neidherr, M. Rosenbusch, L. Schweikhard, J. Stanja, F. Wienholtz, and K. Zuber. Plumbing neutron stars to new depths with the binding energy of the exotic nuclide ^{82}Zn. *Phys. Rev. Lett.*, 110:041101, Jan 2013. URL: https://link.aps.org/doi/10.1103/PhysRevLett.110.041101, doi:10.1103/PhysRevLett.110.041101.

[65] Oh Yoon, Ignacio Zuleta, Matthew Robbins, Griffin Barbula, and Richard Zare. Simple template-based method to produce Bradbury-Nielsen gates. *Journal of the American Society for Mass Spectrometry*, 18:1901–8, 12 2007. doi:10.1016/j.jasms.2007.07.030.

[66] F. Wienholtz, D. Atanasov, S. Kreim, V. Manea, M. Rosenbusch, L. Schweikhard, A. Welker, and R. N. Wolf. Towards ultrahigh-resolution multi-reflection time-of-flight mass spectrometry at ISOLTRAP. *Phys. Scripta*, T166:014068, 2015. doi:10.1088/0031-8949/2015/t166/014068.

[67] T. Dickel, W.R. Plaß, A. Becker, U. Czok, H. Geissel, E. Haettner, C. Jesch, W. Kinsel, M. Petrick, C. Scheidenberger, A. Simon, and M.I. Yavor. A high-performance multiple-reflection time-of-flight mass spectrometer and isobar separator for the research with exotic nuclei. *Nucl. Instrum. Meth. A*, 777:172 – 188, 2015. URL: http://www.sciencedirect.com/science/article/pii/S0168900214015629, doi:https://doi.org/10.1016/j.nima.2014.12.094.

[68] B. Liu, M. Brodeur, D.P. Burdette, J.M. Kelly, T. Kim, J. Long, and P.D. O'Malley. The performance of the commissioned notre dame multi-reflection time-of-flight mass spectrometer. *Nuclear Instruments and Methods in Physics Research Section A: Accelerators, Spectrometers, Detectors and Associated Equipment*, 985:164679, 2021. URL: http://www.sciencedirect.com/science/article/pii/S0168900220310767, doi:https://doi.org/10.1016/j.nima.2020.164679.

[69] Christian Jesch, T. Dickel, Wolfgang Plaß, Devin Short, Samuel San Andres, Jens Dilling, Hans Geissel, F. Greiner, Johannes Lang, Kyle Leach, Wayne Lippert, Christoph Scheidenberger, and Mikhail Yavor. The MR-TOF-MS isobar separator for the TITAN facility at TRIUMF. *Hyperfine Interactions*, 05 2015. doi:10.1007/s10751-015-1184-2.

[70] P. Chauveau, P. Delahaye, G. De France, S. El Abir, J. Lory, Y. Merrer, M. Rosenbusch, L. Schweikhard, and R.N. Wolf. PILGRIM, a Multi-Reflection Time-of-Flight Mass Spectrometer for Spiral2-S3 at GANIL. *Nuclear Instruments and Methods in Physics Research Section B: Beam Interactions with Materials and Atoms*, 376:211 –

215, 2016. Proceedings of the XVIIth International Conference on Electromagnetic Isotope Separators and Related Topics (EMIS2015), Grand Rapids, MI, U.S.A., 11-15 May 2015. URL: http://www.sciencedirect.com/science/article/pii/S0168583X16000732, doi:https://doi.org/10.1016/j.nimb.2016.01.025.

[71] P. Schury, M. Wada, Y. Ito, F. Arai, S. Naimi, T. Sonoda, H. Wollnik, V.A. Shchepunov, C. Smorra, and C. Yuan. A high-resolution multi-reflection time-of-flight mass spectrograph for precision mass measurements at RIKEN/SLOWRI. *Nuclear Instruments and Methods in Physics Research Section B: Beam Interactions with Materials and Atoms*, 335:39 – 53, 2014. URL: http://www.sciencedirect.com/science/article/pii/S0168583X1400559X, doi:https://doi.org/10.1016/j.nimb.2014.05.016.

[72] J. Uusitalo, J. Sarén, J. Partanen, and J. Hilton. Mass Analyzing Recoil Apparatus, MARA. *Acta Phys. Pol. B*, 50(3):319–327, 2019. doi:10.5506/APhysPolB.50.319.

[73] Robert N. Wolf, Gerrit Marx, Marco Rosenbusch, and Lutz Schweikhard. Static-mirror ion capture and time focusing for electrostatic ion-beam traps and multi-reflection time-of-flight mass analyzers by use of an in-trap potential lift. *International Journal of Mass Spectrometry*, 313:8 – 14, 2012. URL: http://www.sciencedirect.com/science/article/pii/S1387380611004775, doi:https://doi.org/10.1016/j.ijms.2011.12.006.

[74] Mikhail Yavor, Anatoli Verentchikov, Juri Hasin, Boris Kozlov, Mikhail Gavrik, and Andrey Trufanov. Planar multi-reflecting time-of-flight mass analyzer with a jig-saw ion path. *Physics Procedia*, 1:391–400, 08 2008. doi:10.1016/j.phpro.2008.07.120.

[75] P. Fischer, S. Knauer, G. Marx, and L. Schweikhard. In-depth study of in-trap high-resolution mass separation by transversal ion ejection from a multi-reflection time-of-flight device. *Rev. Sci. Instrum.*, 89(1):015114, 2018. doi:10.1063/1.5009167.

[76] Y. Toker, N. Altstein, O. Aviv, M. L. Rappaport, O. Heber, D. Schwalm, D. Strasser, and D. Zajfman. The kick-out mass selection technique for ions stored in an Electrostatic Ion Beam Trap. *J. Instrum.*, 4(09):P09001, 2009. doi:10.1088/1748-0221/4/09/P09001.

[77] L. Andersen, Oded Heber, and D Zajfman. Physics with electrostatic rings and traps. *Journal of Physics B: Atomic, Molecular and Optical Physics*, 37:R57, 05 2004. doi:10.1088/0953-4075/37/11/R01.

[78] Y Toker, D Schwalm, L H Andersen, O Heber, and D Zajfman. Sidebands from longitudinal bunch oscillations in an electrostatic ion beam trap. *Journal of Instrumentation*, 9(04):P04008–P04008, apr 2014. doi:10.1088/1748-0221/9/04/p04008.

[79] R. N. Wolf, F. Wienholtz, D. Atanasov, D. Beck, K. Blaum, Ch. Borgmann, F. Herfurth, M. Kowalska, S. Kreim, Yu. A. Litvinov, D. Lunney, V. Manea, D. Neidherr, M. Rosenbusch, L. Schweikhard, J. Stanja, and K. Zuber. ISOLTRAP's

multi-reflection time-of-flight mass separator/spectrometer. *Int. J. Mass Spectrom.*, 349-350:123–133, 2013. `doi:10.1016/j.ijms.2013.03.020`.

[80] M. Hammen, W. Nörtershäuser, D. L. Balabanski, M. L. Bissell, K. Blaum, I. Budinčević, B. Cheal, K. T. Flanagan, N. Frömmgen, G. Georgiev, Ch. Geppert, M. Kowalska, K. Kreim, A. Krieger, W. Nazarewicz, R. Neugart, G. Neyens, J. Papuga, P.-G. Reinhard, M. M. Rajabali, S. Schmidt, and D. T. Yordanov. From calcium to cadmium: Testing the pairing functional through charge radii measurements of $^{100-130}$Cd. *Phys. Rev. Lett.*, 121:102501, Sep 2018. URL: `https://link.aps.org/doi/10.1103/PhysRevLett.121.102501`, `doi:10.1103/PhysRevLett.121.102501`.

[81] P.-G. Reinhard and W. Nazarewicz. Toward a global description of nuclear charge radii: Exploring the fayans energy density functional. *Phys. Rev. C*, 95:064328, Jun 2017. URL: `https://link.aps.org/doi/10.1103/PhysRevC.95.064328`, `doi:10.1103/PhysRevC.95.064328`.

[82] A. J. Miller, K. Minamisono, A. Klose, D. Garand, C. Kujawa, J. D. Lantis, Y. Liu, B. Maaß, P. F. Mantica, W. Nazarewicz, W. Nörtershäuser, S. V. Pineda, P. G. Reinhard, D. M. Rossi, F. Sommer, C. Sumithrarachchi, A. Teigelhöfer, and J. Watkins. https://doi.org/10.1038/s41567-019-0416-9. *Nature Physics*, (5):432–436. `doi:10.1038/s41567-019-0416-9`.

[83] D. T. Yordanov, D. L. Balabanski, M. L. Bissell, K. Blaum, A. Blazhev, I. Budinčević, N. Frömmgen, Ch. Geppert, H. Grawe, M. Hammen, K. Kreim, R. Neugart, G. Neyens, and W. Nörtershäuser. Spins and electromagnetic moments of $^{101--109}$Cd. *Phys. Rev. C*, 98:011303, Jul 2018. URL: `https://link.aps.org/doi/10.1103/PhysRevC.98.011303`, `doi:10.1103/PhysRevC.98.011303`.

[84] D. T. Yordanov, M. L. Bissell, K. Blaum, M. De Rydt, Ch. Geppert, M. Kowalska, J. Krämer, K. Kreim, A. Krieger, P. Lievens, T. Neff, R. Neugart, G. Neyens, W. Nörtershäuser, R. Sánchez, and P. Vingerhoets. Nuclear charge radii of $^{21-32}$Mg. *Phys. Rev. Lett.*, 108:042504, Jan 2012. URL: `https://link.aps.org/doi/10.1103/PhysRevLett.108.042504`, `doi:10.1103/PhysRevLett.108.042504`.

[85] J. D. Holt et al. private communications. 2021.

[86] T. Murböck, S. Schmidt, Z. Andelkovic, G. Birkl, W. Nörtershäuser, and M. Vogel. A compact source for bunches of singly charged atomic ions. *Review of Scientific Instruments*, 87(4):043302, 2016. `arXiv:https://doi.org/10.1063/1.4944946`, `doi:10.1063/1.4944946`.

[87] K. Kreim, M.L. Bissell, J. Papuga, K. Blaum, M. De Rydt, R.F. Garcia Ruiz, S. Goriely, H. Heylen, M. Kowalska, R. Neugart, G. Neyens, W. Nörtershäuser, M.M. Rajabali, R. Sánchez Alarcón, H.H. Stroke, and D.T. Yordanov. Nuclear charge radii of potassium isotopes beyond N=28. *Physics Letters B*, 731:97 – 102, 2014. URL: `http://www.sciencedirect.com/science/article/pii/S0370269314001038`, `doi:https://doi.org/10.1016/j.physletb.2014.02.012`.

[88] Fujii T. Moynier, F. Theoretical isotopic fractionation of magnesium between chlorophylls. *Sci RepB*, 7:69 – 173, 2017. `doi:https://doi.org/10.1038/s41598-017-07305-6`.

[89] F. Wienholtz, K. Blaum, J. Karthein, D. Lunney, S. Malbrunot-Ettenauer, V. Manea, M. Mougeot, L. Schweikhard, T. Steinsberger, and R.N. Wolf. Improved stability of multi-reflection time-of-flight mass spectrometers through passive and active voltage stabilization. *Nuclear Instruments and Methods in Physics Research Section B: Beam Interactions with Materials and Atoms*, 463:348 – 356, 2020. URL: `http://www.sciencedirect.com/science/article/pii/S0168583X19302496`, `doi:https://doi.org/10.1016/j.nimb.2019.04.061`.

[90] F. Ziegler, D. Beck, H. Brand, H. Hahn, G. Marx, and L. Schweikhard. A new pulse-pattern generator based on labview fpga. *Nuclear Instruments and Methods in Physics Research Section A: Accelerators, Spectrometers, Detectors and Associated Equipment*, 679:1–6, 2012. URL: `https://www.sciencedirect.com/science/article/pii/S016890021200280X`, `doi:https://doi.org/10.1016/j.nima.2012.03.010`.

[91] F. Martinez, F.Marx, L. Schweikhard, and et al. The new clustertrap setup. *Eur. Phys. J. D*, 63:255–262, 2011. URL: `https://doi.org/10.1140/epjd/e2011-10528-3`, `doi:https://doi.org/10.1140/epjd/e2011-10528-3`.

[92] V. Lagaki, P. Fischer, H. Heylen, F. Hummera, S. Lechner, S. Sels, F. Maier, P. Plattner, M. Rosenbuschb, F. Wienholtz, R.N. Wolf, W. Nörtershäusera, L. Schweikhard, and S. Malbrunot-Ettenauer. Stray-light suppression for the MIRACLS proof-of-principle experiment. *Acta Physica Polonica B*, 51:571–576, 01 2020. URL: `https://www.actaphys.uj.edu.pl/fulltext?series=Reg&vol=51&page=571`.

[93] W. Gins, R.P. de Groote, M.L. Bissell, C. Granados Buitrago, R. Ferrer, K.M. Lynch, G. Neyens, and S. Sels. Analysis of counting data: Development of the satlas python package. *Computer Physics Communications*, 222:286–294, 2018. URL: `https://www.sciencedirect.com/science/article/pii/S0010465517302990`, `doi:https://doi.org/10.1016/j.cpc.2017.09.012`.

[94] V. Lagaki, H. Heylen, I. Belosevic, P. Fischer, C. Kanitz, F.M. Maier, W. Nörtershäuser, P. Plattner, M. Rosenbusch, M. Vilen S. Sels, L. Schweikhard, F. Wienholtz, R.N. Wolf, and S. Malbrunot-Ettenauer. An accuracy benchmark of the miracls apparatus: Conventional, single-passage collinear laser spectroscopy inside an MR-ToF device. *submitted*, 2021.

7 Cumulative thesis articles

7.1 Author contributions

Article I: *"An accuracy benchmark of the MIRACLS apparatus: Conventional, single-passage Collinear Laser Spectroscopy inside a MR-ToF device"*
V. Lagaki, H. Heylen, I. Belosevic, P. Fischer, C. Kanitz, S. Lechner, F. M. Maier, W. Nörtershäuser, P. Plattner, M. Rosenbusch, S. Sels, L. Schweikhard, M. Vilen, F. Wienholtz, R.N. Wolf and S. Malbrunot-Ettenauer, *submitted* (2021)
V.L. took the lead in performing the experiment supported by individual, selected contributions from other members of the MIRACLS team. Moreover, V.L. performed the full data analysis. V.L. and S.M.E. prepared the manuscript, which was edited by all co-authors.

Article II: *"Stray-light suppression for the MIRACLS proof-of-principle experiment"*
V. Lagaki, P. Fischer, H. Heylen, F.Hummer, S. Lechner, F. Maier, P. Plattner, Marco Rosenbusch, M. Rosenbusch, S. Sels, F. Wienholtz, R.N. Wolf, W. Nörtershäuser, L. Schweikhard, S. Malbrunot-Ettenauer, *Acta Physica Polonica B*, 51, 571-576 (2020)
V.L. took the lead in performing the experiment supported by individual, selected contributions from other members of the MIRACLS team. Moreover, V.L. performed the full data analysis. V.L. prepared the manuscript, which was edited by all co-authors.

Article III: *"First steps in the development of the Multi Ion Reflection Apparatus for Collinear Laser Spectroscopy"*
S. Sels, P. Fischer, H. Heylen, V. Lagaki , S. Lechner, F.M. Maier, P. Plattner, M. Rosenbusch, F. Wienholtz, R.N. Wolf, W. Nörtershäuser, L. Schweikhard, S. Malbrunot-Ettenauer, *Nucl. Instr. Methods B*, 463, 310-314 (2019)
V.L. built the apparatus and took the lead in performing the experiment supported by individual, selected contributions from other members of the MIRACLS team. Moreover, V.L. performed the full data analysis. S.S. with S.M.E. prepared the manuscript, which was edited by all co-authors.

Confirmed:

Greifswald, den   Varvara Lagaki   Lutz Schweikhard

7.2 An accuracy benchmark of the MIRACLS apparatus: Conventional, single-passage Collinear Laser Spectroscopy inside a MR-ToF device

An accuracy benchmark of the MIRACLS apparatus:
Conventional, single-passage Collinear Laser Spectroscopy inside a MR-ToF device

V. Lagaki[a,b,*], H. Heylen[a], I. Belosevic[c], P. Fischer[b], C. Kanitz[a,d], S. Lechner[a,e], F.M. Maier[a,b], W. Nörtershäuser[f], P. Plattner[a,g], M. Rosenbusch[b,1], S. Sels[a,2], L. Schweikhard[b], M. Vilen[a], F. Wienholtz[a,b], R.N. Wolf[b,3], S. Malbrunot-Ettenauer[a]

[a]*Experimental Physics Department, CERN, CH-1211 Geneva 23, Switzerland*
[b]*Institut für Physik, Universität Greifswald, 17487 Greifswald, Germany*
[c]*TRIUMF, 4004 Wesbrook Mall, Vancouver BC V6T 2A3, Canada*
[d]*Department für Physik, Friedrich-Alexander-Universität Erlangen-Nürnberg, 91058 Erlangen, Germany*
[e]*Technische Universität Wien, Karlsplatz 13, 1040 Wien, Austria*
[f]*Technische Universität Darmstadt, Karolinenpl. 5, 64289 Darmstadt, Germany*
[g]*Universität Innsbruck, Innrain 52, 6020 Innsbruck, Austria*

Abstract

Collinear laser spectroscopy (CLS) has been performed in a multi-reflection time-of-flight (MR-ToF) device operated in single-pass mode, i.e., without confining the ions in the ion trap. While our Multi Ion Reflection Apparatus for Collinear Laser Spectrosocpy (MIRACLS) aims to increase the CLS sensitivity by storing ions in the MR-ToF device, the present work characterises conventional single-passage CLS as a preparatory step for the upcoming comparison with MIRACLS' multi-pass mode. To this end, the isotope shift in the $3s\,^2\mathrm{S}_{1/2} \to 3p\,^2\mathrm{P}_{3/2}$ transition (D2 line) between ions of the magnesium isotopes ^{24}Mg and ^{26}Mg has been measured under varying experimental conditions. Our result agrees with the precise literature value. Associated studies of systematic uncertainties demonstrate a measurement accuracy of better than 20 MHz in this new apparatus. This value will serve as the reference for analogous studies to be performed in the MIRACLS approach in which ions are trapped in the MR-ToF device for thousands of revolutions and probed by the spectroscopy laser during each passage.

1. Introduction

For nearly five decades, atomic-physics techniques have very successfully provided accurate and precise information about nuclear ground state properties of short-lived radionuclides [1–7]. While laser spectroscopy accesses nuclear spins, charge radii and electromagnetic moments, ion traps have become invaluable tools for precision mass measurements.

Within the latter, multi-reflection time-of-flight (MR-ToF) instruments have in recent years emerged in the field of rare isotope science as versatile mass separators and spectrometers [8–16]. In these devices, also called electostatic ion beam traps [17–19], an ion bunch is reflected between two electrostatic mirrors such that an integrated ion flight path of a few kilometers can be folded into an apparatus with the length of about one meter. Ions of different masses m are consequently separated in mass according to their respective time of flight. Mass resolving powers exceeding $R = m/\Delta m > 10^5$ can be obtained in (tens of) milliseconds [13, 20, 21].

Given these superb performance characteristics, MR-ToF devices have recently found many applications at modern radioactive ion beam (RIB) facilities. Among others, these include mass measurements of radionuclides very far away from stability with production yields as low as a few ions per second [12, 22–24], beam identification for various experimental RIB programs [25], characterisation and optimisation of RIB production targets for fundamental science as well as medical isotope production [26, 27], suppression of contamination in the RIB [28], or mass-tagged ion counting in ion-source laser spectroscopy [29].

Our Multi Ion Reflection Apparatus for Collinear Laser Spectroscopy (MIRACLS) developed at ISOLDE/CERN envisions a novel application of MR-ToF devices, namely for highly sensitive laser spectroscopy. To this end, it combines the sensitivity of ion-trap techniques with the high resolution of collinear laser spectroscopy (CLS) of fast ion beams. In the latter, an ion beam with typical beam energies of ≥ 30 keV is collinearly overlapped with a narrow-band, continuous-wave laser beam. When the frequency of the laser corresponds to the energy difference of the studied transition, fluorescence light of laser-excited ions is reg-

---

istered by photon detectors. Hence, the detected photon rate as a function of laser frequency reveals the hyperfine structure which encodes the aforementioned nuclear properties by means of the hyperfine interaction between the atomic nucleus and its surrounding electron cloud.

Although nuclides accessible by CLS exhibit life-times of at least several milliseconds, their effective use in this conventional CLS approach is limited to a few microseconds while the ions pass the laser-ion interaction and optical-detection region. Hence, matching the involved time scales offers the possibility to significantly boost the experimental CLS sensitivity.

Following this vision, MIRACLS aims at confining the fast ion beam inside a MR-ToF device in which the ions are 're-cycled' by continued reflections between the two electrostatic mirrors. Thus, the ion ensemble can be repeatedly probed by the spectroscopy laser during each revolution in contrast to only once for conventional CLS. The MIRACLS approach increases the observation time and, hence, the CLS sensitivity. For instance, in closed two-level systems in which laser-excited ions decay back into their initial state, an ion can in principle be investigated until its radioactive decay. As a result, the MIRACLS approach is expected to yield multiplication factors of 30-700 depending on the half-life, mass and spectroscopic transition of the ions of interest.

To demonstrate the strengths of the MIRACLS concept, an MR-ToF apparatus [30, 31] has been extended for the implementation of in-trap CLS [32–35]. In particular, the MR-Tof's central drift tube hosts a field-free region for laser-ion interaction and optical detection. Laser access is provided along the axis of the device. While typical ion beam energies in CLS experiments of radionuclides are in the order of several tens of kiloelectron volts, the present setup operates at a beam energy of about 1.5 keV. This will allow proof-of-principle measurements for MIRACLS before the method will be applied in a future 30-keV device.

In the present work, we have as a first step performed conventional, single-passage CLS within this setup in order to benchmark the attainable accuracy for isotope-shift measurements in such an instrument. In particular, we have measured the isotope shift $\delta\nu^{24,26} = \nu_0^{26} - \nu_0^{24}$ in the $3s\,^2S_{1/2} \rightarrow 3p\,^2P_{3/2}$ transition (D2 line) between $^{24}Mg^+$ and $^{26}Mg^+$ ions. We varied the experimental procedures and parameters to expose systematic uncertainties for CLS in this apparatus. Thus, the presnt study lays the foundations for ongoing work on the MIRACLS technique. It will allow us to disentangle general limitations of this particular CLS implementation at relatively low ion energies from potential influences specifically caused by MR-ToF operation and ion storage.
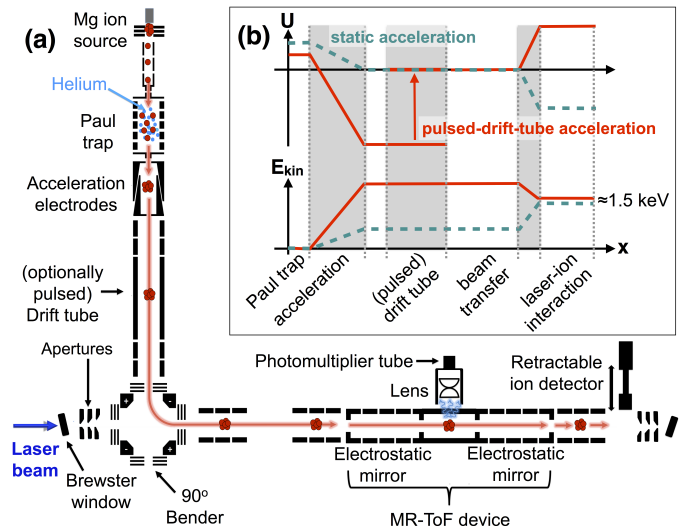

Figure 1: (a) Schematics of the experimental setup. (b) Sketch of electric potential U and ion beam energy E_{kin} along the path of the Mg^+ ions from the Paul trap to the laser-ion interaction region inside the MR-ToF device. Two different acceleration and ion-transfer schemes are employed. One involves a pulsed drift tube and is represented by the red solid lines. The second one is purely based on static potentials, see turquoise dashed lines. Both result in a final energy of $E_{kin} \approx 1.5$ keV when passing through the laser-ion interaction and optical detection region. See text for details.

2. Experimental Setup

2.1. MR-ToF apparatus

The experimental apparatus is based on the MR-ToF system described in Ref. [30, 31], which was upgraded for the purpose of collinear laser spectroscopy [32–35]. A schematic overview of the setup is shown in Fig. 1a. For the present study, Magnesium (Mg) atoms are ionized inside an electron-impact ion source which closely follows the design in Ref. [36]. Singly-charged ions of stable magnesium isotopes $^{24-26}Mg$ form a continuous beam which is injected into a helium buffer-gas-filled linear Paul trap. The latter consists of two end-cap plates with holes for ion injection and extraction as well as four rods which provide the RF field for radial ion confinement. The rods are longitudinally split into five segments of equal length and establish a DC gradient to drag buffer-gas-cooled ions into a potential minimum next to the downstream end-cap plate.

In order to define the ion loading time and hence the ion number inside the Paul trap, a steering electrode in front of the ion trap is controlled by a fast high voltage (HV) switch which, on demand, guides the ions either into or away from the Paul-trap entrance. After a cooling time typically set to a few milliseconds, the accumulated and cooled ions are released from the trap by lowering the potential of the downstream end-cap plate by another fast HV switch. The extraction pulse is synchronised with respect to the RF phase to ensure identical field conditions during each ion ejection.

The well-defined ion bunches with a typical temporal width

of a few hundred nanoseconds are subsequently accelerated for their transfer into the MR-ToF device. In the present work, two different acceleration schemes are utilised, see Fig. 1b. In the first option, which has been used in our previous work [32, 33, 35], the Paul trap is held at a potential of $U_{pt} \approx 250$ V. After extraction from the Paul trap, the ions are accelerated towards beamline components at $U_{acc} \approx -2080$ V. When the ion bunch reaches the centre of a drift tube, its potential is switched to ground potential (represented by a red, vertical arrow in Fig. 1b). Since this drift tube constitutes in its centre a field-free region, the change in potential is unnoticed by the ions and the pulsed drift tube acts as a 'potential lift'. Hence, the ions exit the drift tube with a kinetic energy of $E_{kin} = e(U_{pt} - U_{acc}) \approx 2330$ eV.

Since HV switching of this pulsed drift tube may lead to some uncertainty in the exact ion beam energy, a second acceleration scheme exclusively based on static potentials is alternatively employed. Considering its common use in CLS, the present work is largely based on this acceleration scheme. It proceeds identically to the previous one, but the acceleration is done towards $U_{acc} = 0$ V such that the drift tube remains on ground potential for the entire measurement cycle. The transfer energy is, hence, solely governed by $E_{kin} = eU_{pt}$. We observe a degraded transfer efficiency for lower ion beam energies, likely due to the increased transverse emittance. Consequently, we permanently raise the Paul trap potential to $U_{pt} \approx 470$ V which is close to its maximum in the present technical configuration.

Independently of the acceleration method, the ion beam subsequently passes an electrostatic quadrupole bender which guides the ions onto the MR-ToF axis. In the present work, all ring electrodes constituting the electrostatic mirrors of the MR-ToF device are left on ground potential. Hence, the ions cannot be trapped in the ion trap. Surrounded by the electrostatic mirrors, the MR-ToF's central drift tube is biased to a potential U_{cdt} such that the ions propagate inside the tube with $E_{kin} = eU_{tot} = e(U_{pt} - U_{acc} - U_{cdt}) \approx 1500$ eV, a kinetic energy typically used during MR-ToF operation. In particular, $U_{cdt} = 830$ V when utilising the lift after the initial acceleration and $U_{cdt} = -1010$ V otherwise.

During setup and ion-beam optimization, the ions impinge on a retractable ion detector at the end of the setup. At this position, ions of different magnesium isotopes are well resolved in time of flight even without being trapped in the MR-ToF device.

2.2. Laser setup

The employed laser setup has been discussed in detail in [35]. In order to study the $3s\,^2S_{1/2} \rightarrow 3p\,^2P_{3/2}$ transition (D2 line) in Mg$^+$ ions, a laser wavelength of 280 nm ($\lambda^{-1} = 35760.88$ cm^{-1}) is required. In a separate laser laboratory, a diode-pumped solid-state laser pumps a frequency-stabilised dye ring laser which produces a narrow-band, continuous-wave laser beam at 560 nm.

The latter is coupled into a high-power optical fibre to transport the laser beam into the about 25-m distant MR-ToF laboratory. There, second-harmonic generation is employed to obtain a laser beam at 280 nm. The output of the frequency doubler is stabilised in power by a proportional–integral (PI) feed-back loop which rotates a $\lambda/2$ plate in front of a polarisation filter in the upstream beam path of the 580 nm laser light and, thus, controls the laser power input into the frequency doubler.

After mode cleaning to obtain a Gaussian beam profile, the laser beam is sent into the MR-ToF apparatus with a typical power of ≈ 0.7 mW. At its entrance and exit, a quartz window is installed at the Brewster angle, see Fig. 1, to minimise reflections which could potentially lead to undesired laser stray light. The latter is further reduced by aperture sets which are placed in-vacuum next to the entrance and exit windows [34].

The laser frequency is set by locking the dye ring laser to a precision wavemeter (HighFinesse WSU-10) which is regularly calibrated against a temperature-stabilized He-Ne laser. To probe the hyperfine structure of an ion of interest, the laser is scanned across the anticipated frequency range. For each frequency step, photons are recorded for ion bunches released from the Paul trap in multiple measurement cycles.

In this work, two methods are used to scan the laser frequency in the rest frame of the ions. First, the laser frequency in the laboratory reference frame is fixed while the velocity of the ions is changed by altering the potential U_{cdt} of the MR-ToF's central drift tube. This results in a Doppler tuning of the laser frequency ν_{ion} observed by the ions according to

$$\nu_{ion} = \nu_{lab} \cdot \frac{1 - \beta}{\sqrt{1 - \beta^2}}. \tag{1}$$

Here, ν_{lab} represents the laser frequency in the laboratory frame and $\beta = v/c$ is the ion velocity v relative to the speed of light c. This approach is commonly applied in CLS [5].

However, for CLS studies over long isotopic chains or wide hyperfine structures the required difference in energy can be sizable. Within MIRACLS, different ion energies will lead to modified ion trajectories inside the MR-ToF device. This may influence the CLS measurement. For this reason, it is foreseen to operate MIRACLS' MR-ToF device at fixed ion energies and to scan the laser frequency directly in the laboratory frame. Consequently, this scheme, called laser scanning in the following, has also been tested in the present work for conventional, single-passage CLS. In our implementation, the set point of the PID loop which locks the dye laser to the wavemeter is altered in small steps such that the laser cavity follows to the new value. While the laser frequency is being changed all data taking is put on hold until the new set point in the fundamental wavelength has been reached within less than 1.5 MHz. The PID parameters have been optimised for stability as well as fast and reliable changes in frequency, i.e., in our configuration,

a frequency step of 10 MHz typically requires a few seconds until completion.

2.3. Optical detection region and data acquisition

The ion-laser interaction to excite the optical transition takes place in the field-free region of the MR-ToF's central drift tube. The latter is constructed from two ring electrodes, approximately 12 cm apart, connected by a cylindrical mesh. This establishes a well-defined electric potential and allows fluorescence light to reach a lens system (adopted from [37]) which directs the photons onto a photomulitpler tube, see Fig. 1a. Around this optical detection region, a blackened shield is mounted [34]. It prevents laser stray light, which does not arise from the ion-beam axis, to be reflected into the lenses and subsequently into the photodetector.

The signal of the photomultiplier tube is passed on to a multichannel scaler which records the number of detected photons versus time since the ions' extraction from the Paul trap. For each laser frequency, the data of multiple measurement cycles, typically a few hundred ion bunches ejected from the Paul trap, are summed. On resonance, the passage of the ion bunch in the optical detection region is visible in the histogram of photon number versus time as a peak of increased photon rate. In our MR-ToF setup, which has initially been designed for other purposes than CLS, laser stray light largely dominates the photon background. To suppress the background counts, the signal is gated in the analysis on the ion passage.

3. Measurement procedure and analysis

Typical resonances of ^{24}Mg$^+$ and ^{26}Mg$^+$ ions are shown in Fig. 2. Since both Mg isotopes are nuclides with nuclear spin $I = 0$, there is no hyperfine splitting and, thus, only a single peak is present in the resonance spectra. For a resonance scan, each laser frequency ν_{lab} is converted to the ions' rest frame frequency, ν_{ion}, according to Eq. 1. For an ion with mass m accelerated by an overall acceleration potential U_{tot} this becomes

$$\nu_{\mathrm{ion}} = \nu_{\mathrm{lab}} \frac{eU_{\mathrm{tot}} + mc^2}{mc^2} \left(1 - \sqrt{1 - \frac{m^2c^4}{(eU_{\mathrm{tot}} + mc^2)^2}} \right). \tag{2}$$

Here, e is the elementary charge and c the speed of light. In the calculation of U_{tot}, we assume U_{pt}, the starting potential from which the ions are released from the Paul trap, to be the mean value of the DC potentials applied to two segments which form the bottom of the well in the Paul trap, see later discussion in Sec. 4.1.1. All relevant electrical potentials are measured on a regular basis with high-precision voltage dividers. This includes measurements of the individual voltage steps when scanning the potential of the MR-ToF's central drift tube during Doppler tuning. Due to the relatively low beam energy of $E_{\mathrm{kin}} \approx 1.5$ keV, the observed full width at half maximum (FWHM) of the
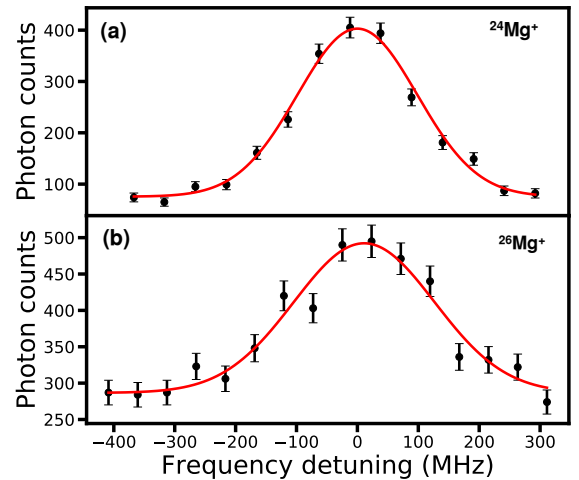

Figure 2: Measured resonance spectra of the D2 transition in ^{24}Mg$^+$ (a) and ^{26}Mg$^+$ ions (b) performed with laser scanning and a 'fast' Paul-trap extraction scheme. The experimental data of photon counts versus laser frequency (in black) is fitted by a Gaussian line shape (in red). The loading time and, hence, the total number of ions in the Paul trap remain the same for both runs, here 10 ms, to ensure identical conditions. The different resonance intensities are a consequence of the natural abundance of the Mg isotopes. The lower abundance of ^{26}Mg is partially compensated by collecting data over, in this case, 4 times more measurement cycles. See text for details.

experimental resonances is ≈ 250 MHz, i.e., much larger than the natural line width of 42 MHz of the D2 transition. Hence, the line width is dominated by Doppler broadening which results in a Gaussian line shape. Assuming that the line width is entirely governed by the ions' energy distribution, the FWHM in Fig. 2a corresponds to an energy spread of ≈ 1.8 eV at the given ion energy. All resonance spectra are fitted by a Gaussian line profile utilising a χ^2-minimization procedure in the SATLAS analysis package [38] to obtain the respective centroid frequency ν_0.

Each individual isotope-shift measurement $\delta\nu^{24,26}$ between ^{24}Mg$^+$ and ^{26}Mg$^+$ ions is initiated by the calibration of the wavemeter. Subsequently, CLS is performed by recording two ^{24}Mg$^+$ resonance spectra interleaved with one of ^{26}Mg$^+$ ions under identical measurement conditions. Because of its lower natural abundance, measurements with ^{26}Mg$^+$ ions last significantly longer than for ^{24}Mg$^+$ ions to obtain resonance spectra of comparable quality. The independent ^{24}Mg measurements also serve as a measure of potential drifts in the system during the longer data taking of ^{26}Mg$^+$ ions. For this purpose, the weighted average of the ^{24}Mg measurements, $\bar{\nu}_0^{24}$, and the associated Birge ratio R_B [39][4] are evaluated. Following the proce-

---

[4]For a set of n measurements x_i with an uncertainty σ_i, the Birge ratio is defined as

$$R_B = \sqrt{\chi^2/(n-1)} = \sqrt{\frac{1}{1-n} \sum_{i=1}^{n} \frac{(x_i - \bar{x})^2}{\sigma_i^2}}, \tag{3}$$

where $\bar{x}$ is the weighted average over all individual measurements x_i.

dures adopted by the Particle Data Group [40], we inflate the uncertainty on $\bar{\nu}_0^{24}$ by the Birge ratio in case the latter is larger than one. Finally, the isotope shift is calculated following $\delta\nu^{24,26} = \nu_0^{26} - \nu_0^{24}$.

With the aim to expose potential systematic errors in our apparatus, we have performed measurements of this isotope shift under various experimental conditions. These include different measurement schemes which could impact the ions' beam energy, i.e., (1.1) different ion extraction schemes from the Paul trap as well as (1.2) the two methods in ion acceleration as explained in Sec. 2.1. For the former, we use two different field gradients in the Paul trap resulting in a 'slow' or a 'fast' release from the ion trap, respectively. Moreover, (2) the Paul-trap loading time and, hence, ion numbers are varied to investigate space-charge effects in the ion trap. Finally, (3) the laser frequency as observed by the moving ions is changed via either laser scanning or Doppler tuning. Table 1 summarises all isotope-shift measurements in this work according to their respective experimental configurations.

In each measurement setting, $\delta\nu^{24,26}$ is determined multiple times and a weighted average is constructed. The uncertainty of the latter is inflated following the previously explained procedure in case of a Birge ratio $R_B > 1$ which indicates that the variations within the individual measurements exceed the statistically expected fluctuations. Fig. 3a and b provide examples for individual isotope-shift measurements in selected measurement configurations, discussed in detail next.

4. Results and Discussion

As stated above, the aim of the present measurement campaign is to determine the isotope shift $\delta\nu^{24,26}$ between $^{24}\text{Mg}^+$ and $^{26}\text{Mg}^+$ ions in the D2 transition in order to isolate systematic uncertainties of the new apparatus arising from everything except for the MR-ToF operation itself. The results of the different measurement schemes as introduced above are compared to each other in Fig. 4.

Table 1: Overview of all isotope-shift measurements in this work indicating the used ion-acceleration scheme (Accel.), the Paul-trap extraction mode, the Paul-trap loading time, as well as the employed method of frequency scanning, i.e., laser scanning or Doppler tuning. The number of individual isotope-shift measurements for each setting is listed in the last column.

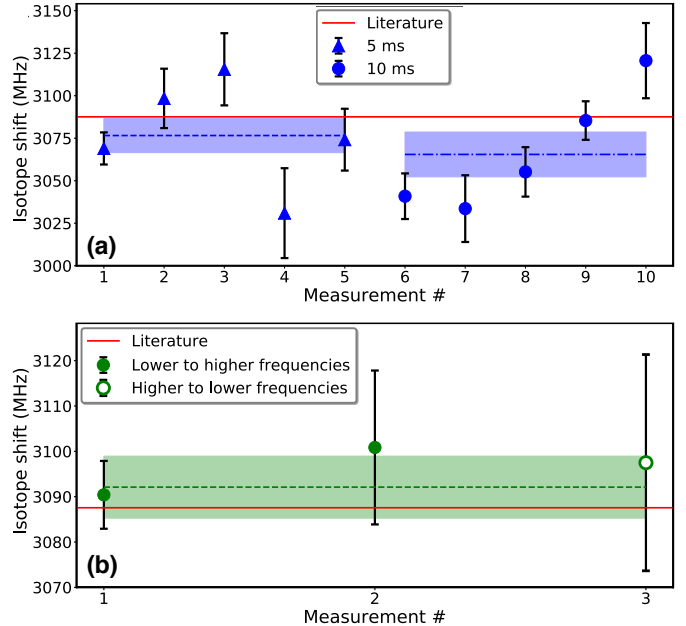| #	Accel.	Paul-trap extraction	Loading time (ms)	Scanning mode	# of IS
1	static	fast	5	laser	5
2	static	fast	10	laser	5
3	static	slow	20	laser	5
4	static	fast	20	laser	1
5	static	slow	10	Doppler	3
6	static	slow	20	Doppler	2
7	lift	fast	≤ 1	laser	2

Figure 3: Examples for the results of individual isotopes-shift measurements $\delta\nu^{24,26}$. (a) Results for different Paul-trap loading times for measurements performed with laser scanning and a 'fast' ion extraction. (b) $\delta\nu^{24,26}$ results for Doppler tuning from either lower to higher frequency or vice versa. A 'slow' ion extraction and a 10-ms loading time is employed. The respective weighted average of the individual measurements is indicated as a dashed line and its uncertainty is represented by the shaded area. For comparison, the precise literature value is shown in red. See text for details.

As a final accuracy benchmark, the present isotope-shift value is compared to its much more precise determination of $\delta\nu^{24,26} = 3087.560(87)$ MHz, measured using laser- and sympathetically-cooled Mg^+ ions stored in a Paul trap [41]. In the following, we discuss the results as well as all systematic uncertainties identified in this work.

4.1. Ion beam energy

In CLS, the dominating systematic uncertainty is normally related to an incomplete knowledge of the ion beam energy E_{kin}. For conventional CLS with $E_{\text{kin}} \geq 30$ keV, this is due to the uncertainty of the high-precision voltage dividers which are used to measure the acceleration potentials, e.g. the floating potential of the ion source or of a Paul trap acting as a ion cooler and buncher.

In our work, the largest systematic uncertainty is also found in E_{kin}. However, at the smaller electrostatic potentials and ion energies in our setup, the larger contribution arises due to uncertainties in the ions' starting potential within the Paul trap itself. Moreover, the realistic HV switching of the pulsed drift tube can result in an ion beam energy which differs from the expectation of the idealised lift operation. The two effects are discussed in the following subsections.

4.1.1. Starting potential U_{pt} in the Paul trap

The voltage applied to the DC electrodes at the bottom of the Paul-trap's potential well is not necessarily the
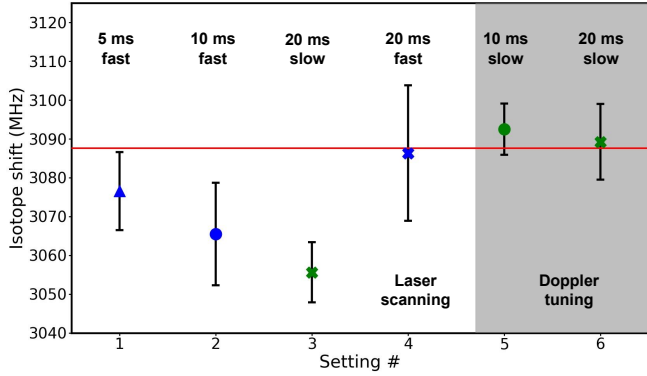
Figure 4: Results of the systematic investigations in the isotopes shift $\delta\nu^{24,26}$ within the MIRACLS apparatus with conventional, single-passage CLS. For all displayed measurements, the ions are accelerated by static potentials. Each data point corresponds to the weighted average of several individual measurements within a given measurement settings. The latter are characterised by their frequency-scanning method (laser scanning or Doppler tuning), Paul-trap extraction scheme ('slow' or 'fast'), and the Paul-trap loading time. See text for details.
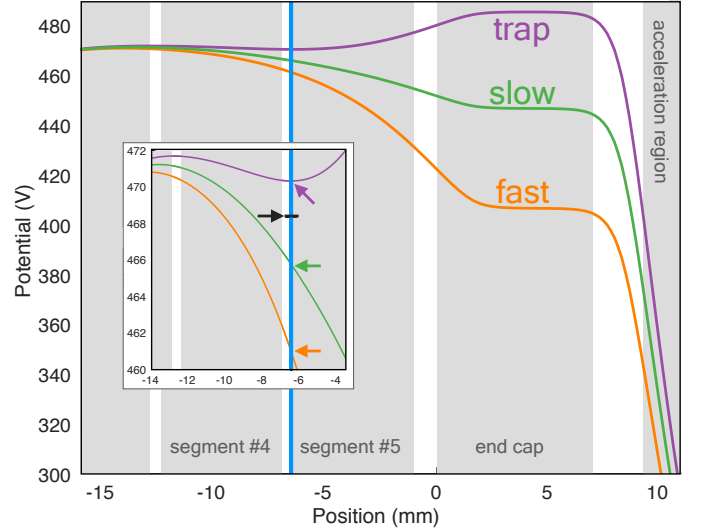

Figure 5: Electrostatic potential along the axis of the Paul trap during ion trapping as well as for the 'slow' and 'fast' ion extraction. The insert provides a closer look on the trapping region. The vertical blue line indicates the location of the potential minimum during trapping. The colored arrows point to the potential's value at this location for all three configurations. The black arrow indicates the mean value of the voltages applied to the electrodes of segment 4 and 5. See text for details.

same as the potential which the ions are exposed to. Moreover, the process of ion extraction from the ion trap may further affect the ions' kinetic energy E_{kin}. Both factors are of concern for conventional CLS of bunched beams in general. However, these effects are commonly surpassed in magnitude by the uncertainties in the voltage-divider ratio when working with $E_{\mathrm{kin}} \geq 30$ keV.

In order to estimate the ions' starting potential in our Paul trap, the electric potential within a 3D model of the ion trap is determined by solving the Laplace equation in a finite-difference method. The results of the calculations are shown in Fig. 5 for ion trapping as well as for two potential configurations by which the ions are released from the trap. We refer to the latter as 'slow' and 'fast' ion extraction, respectively, reflecting the smaller and larger potential gradient during initial ion acceleration. The three configurations differ in their respective potential applied to the end cap, which is 485 V for trapping, 407 V for 'slow' and 447 V for 'fast' extraction.

In the ion trapping mode, the minimum of the potential well is determined which also defines the mean ion position at the time of the extraction. The potential's value at this minimum would represent the initial ion potential U_{pt} if the ions were directly released from this minimum. In practice, the HV switching of the end cap will influence the ions' starting potential U_{pt}. In case of an infinitely fast HV switching, for instance, the ions would instantaneously 'drop' to the potential evaluated at the same axial position but in the configuration of ion extraction. The corresponding values are indicated in Fig. 5 by colored arrows for 'slow' and 'fast' ion extraction, respectively. The correct potential value U_{pt} should be somewhere in-between the extreme scenarios of infinitely fast HV switching and the minimum of the potential well during ion trapping. Since the exact starting potential in the Paul trap U_{pt} with

realistic HV switches is not known, we assume U_{pt} in the analysis to be the mean of the DC potentials applied to the two electrodes at the bottom of the Paul-trap well (Segment 4 and 5 in Fig. 5), as mentioned already in Sec. 2.1. This U_{pt} potential is very close to the mid-value between the potentials of trapping and 'slow' extraction, see Fig. 5. Additionally, to constrain the possible impact of the ions' starting potential on the isotope shift, we determine the potential at the trap minimum for trapping as well as extraction (see again colored arrows in the insert Fig. 5). These values are then used in the calculation of the ion beam energy and the respective isotope shift $\nu_0^{24,26}$ is determined. Considering these values, we take the maximal difference to the result with the previously assumed U_{pt} as the systematic uncertainty in $\nu_0^{24,26}$. This corresponds to ± 12 MHz in 'slow' and $+12/-40$ MHz in 'fast' extraction, respectively. Note that this systematic uncertainty is not included in Fig. 4 since it correlates the individual uncertainties, i.e., it shifts all values in the same direction and, within each group of identical extraction schemes, also by the same amount.

Experimentally, no statistically significant difference between the results of 'slow' and 'fast' extraction is observed, see Fig. 4. Since the uncertainties of isotope-shift measurements performed with 'slow' ion extraction are much smaller, both in statistics as well as systematics, their weight dominates the entire data set. Because of the reasonable agreement in the results of 'slow' and 'fast' extraction, we consequently adopt a systematic uncertainty of ± 12 MHz for incomplete knowledge of the ions' starting potential in the present work.

4.1.2. Pulsed drift tube

Pulsed drift tubes are commonly employed in ion-trap installations as they provide an elegant solution to define ion energies independently of the electrostatic potentials of vacuum chambers and beamlines. In CLS, however, these potential lifts are generally avoided since accurate knowledge of the ion-beam energy is indispensable. The operation of the pulsed drift tube as part of the ion acceleration can affect the ion beam energy in an unexpected way such that E_{kin} differs from the expectation in an idealised lift. Indeed, when assuming the nominal acceleration voltages related to the puled drift tube in this work, see Sec. 2.1, we obtain an isotope shift $\nu_0^{24,26}$ which is about 200 MHz larger than the literature value.

Because of the non-vanishing capacitance of the pulsed drift tube and practical limitations of electric circuits, the HV switching of the drift tube cannot be performed in the form of an ideal step function. As a consequence, the ions may exit the lift before its final potential is reached. In our case, the HV switch is operated in a slightly over-damped mode, i.e., without major oscillations in voltage at the beginning of the HV switching. This will result in a lower ion energy compared to the estimate based on the nominal switch voltages. Assuming both isotopes are affected the same, a shift of 200 MHz in the isotope shift would correspond to ≈ 40 V in the acceleration potential. This is about 2 % of the HV switched at the pulsed drift tube. Measurements of the HV switching by 'standard equipment' in the laboratory suggest that this value reflects the right order of magnitude. We hence conclude that the use of a pulsed drift tube for accurate CLS requires detailed knowledge about the process of the respective HV switching or a sufficiently-long lift electrode. Measurements utilising the pulsed drift tube will thus not be considered further in the present work.

4.2. Paul-trap loading time and space-charge effects

Due to their Coulomb force interactions, the number of ions stored in the Paul trap has an influence on the properties of the ion ensemble. For CLS of bunched beams, these so-called space-charge effects may cause sizable shifts in the resonance centroids. To study their importance in our apparatus, different loading times of the Paul trap and, hence, numbers of stored ions are explored.[5]

---

[5]We note that the loading time is an incomplete parameterisation of the ion number. For instance, the ion-source current may change over a period of several measurement days resulting in different ion numbers despite the same loading time. At this time, we do not have the means to reliably determine the number of ions in an ion bunch. Our best estimate relies on single-ion counting at low intensities which is then scaled to longer loading times when pile-up in the ion detection occurs. This approach assumes a strict linearity between ion number and loading time. Although previous work suggests that such a linearity holds at least for the presently used loading times [42, 43], it is not established with certainty in this work. Hence, we prefer to state the loading time instead of an estimated ion number, despite the former's aforementioned limitations.
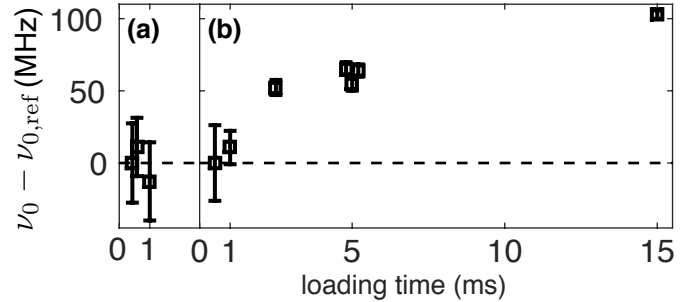

Figure 6: Resonance centroids ν_0 of ^{24}Mg$^+$ ions for different Paul-trap loading times compared to a reference value $\nu_{0,ref}$ corresponding to a measurement with a loading time of 0.5 ms. (a) and (b) represent two independent measurements sets. See text for details.

Compared to other Paul traps exploited for CLS, ours is relatively small. For instance, ISOLDE's cooler and buncher ISCOOL [44, 45] is operated for CLS applications with a flatter axial potential, among others, as three DC segments of each 9 mm in length are biased to the same voltage. Consequently, up to 10^6 ions can be simultaneously prepared in ISCOOL without affecting the CLS resonance spectrum.

In our trap, however, we notice space-charge effects already at much lower ion numbers. For example, Fig. 6b shows the measured centroid frequency of ^{24}Mg, ν_0^{24}, for different Paul-trap loading times. The centroid clearly increases with increasing loading time. This effect is much larger than frequency drifts in the system over time, as illustrated by three measurements at 5 ms in Fig. 6b which are taken at the beginning, middle and end of this measurements series.

Data for loading times of ≤ 1 ms, see also Fig. 6a, may indicate an operation bellow the trap's space-charge limit. However, the experimental uncertainties are too large to fully confirm the independence of ν_0 from the ion number. A loading time of 1 ms corresponds to ≈ 900 ^{24}Mg$^+$ ions per ion bunch at the end of the beamline when the ion number registered by the ion detector at low rates is scaled by the loading time.

In Fig. 3a, the implications of space-charge effects on the isotope shift are illustrated. While all other measurement settings remain identical, individual isotope shifts as well as their weighted averages are shown for the Paul-trap loading times of 5 ms and 10 ms. Within uncertainties, the isotopes shifts for both loading times agree with each other. Hence, the shift in ν_0 cancels in the isotope shift $\delta\nu^{24,26}$ in our work. This can be explained by the fact that ions of all Mg isotopes are stored simultaneously in the Paul trap. Thus, when the same loading time is used for measurements of ^{24}Mg and ^{26}Mg, both isotope masses appear to be similarly affected by the space charge of the single cloud of mixed isotopes.
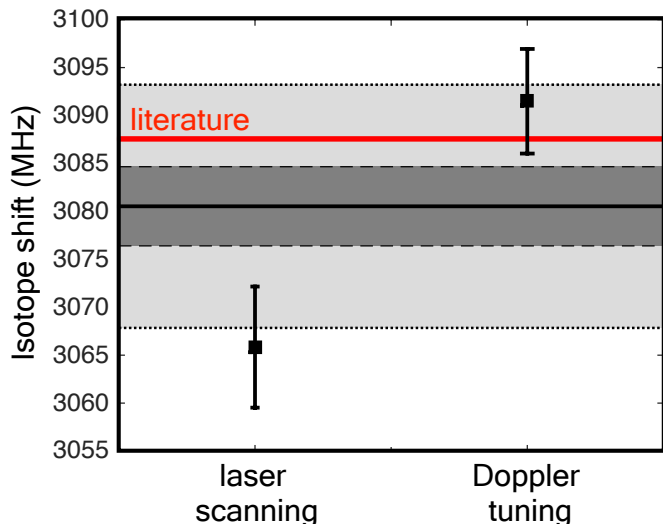
Figure 7: Isotope shift $\nu_0^{24,26}$ obtained by laser scanning and Doppler tuning. The weighted average of the two is indicated by the black line. The dark grey band represents the statistical uncertainty while the light gray band is the inflated uncertainty reflecting a systematic uncertainty on the isotope shift between these two scanning methods. Note that the systematic error due to the ions' starting potential is not included in the given data. See text for details.

4.3. Doppler tuning versus laser scanning

As discussed earlier, Doppler tuning is realised for a subset of the isotope-shift measurements by scanning the voltage applied to the MR-ToF's central drift tube. Fig. 3b presents the results of one Doppler-tuning data set. By introducing a sufficiently long waiting time in the measurement cycle, it is ensured that each voltage step is completed prior to data taking. To investigate potential remaining effects, the direction of the voltage scanning has been reversed. As shown in Fig. 3b, the respective results agree within their statistical uncertainties.

In addition to Doppler tuning, data sets are recorded with scanning the laser frequency in the laboratory frame. As visible in Fig. 4, a discrepancy between $\nu_0^{24,26}$ obtained from Doppler tuning and from laser scanning is observed. Since there is no evidence of systematic errors due to the other experimentally tested configurations, we combine all results from each frequency-scanning method. From a statistical perspective, each of these sets itself represents a fairly consistent data set. However, as shown by Fig. 7, the weighted averages in $\nu_0^{24,26}$ of laser scanning and of Doppler tuning are not consistent with each other. Note that the plotted values for $\nu_0^{24,26}$ do not consider the systematic uncertainty due to the ions' starting potential, see Sec. 4.1.1. This accounts for 12 MHz in $\nu_0^{24,26}$ when considering the 'slow' extraction scheme, but also correlates the two results. If this systematic effect shifts one of them towards a higher value of $\nu_0^{24,26}$, the second result will follow in the same direction, too. Hence, although voltage scanning is favoured, the comparison of the data to the accurate literature value does not unambiguously resolve whether a method of frequency scanning is fully

robust against systematic errors. Consequently, we proceed by following the previously introduced prescription and inflate the uncertainty on the weighted average of the two data sets with the Birge ratio R_B. Considering that systematic and statistical error should add in quadrature to this inflated uncertainty, we assign a systematic uncertainty of $\sigma_{\text{sys,FS}} = \sigma_{\text{stat}}\sqrt{R_B^2 - 1} = 12\,\text{MHz}$ due to the frequency-scanning methods in this work.

While Doppler tuning is the most commonly applied method in CLS, laser scanning is, for instance, employed by the CRIS collaboration at an accuracy of better than 1 MHz for isotope shifts, see Ref. [46, 47] for measurements in a similar mass range. The implementation of laser scanning in the present work proceeds similarly but differs in three technical aspects. Firstly, our wavemeter operates at a lower accuracy compared to the device employed by the CRIS. Secondly, instead of a He-Ne laser in our work, the wavemeter at CRIS is more accurately calibrated by a diode laser which is locked to a transition in rubidium or potassium atoms. Finally, the beams of diode laser and spectroscopy laser are coupled at CRIS into a Fabry-Perot Interferometer for laser frequency monitoring and calibration [46].

Recently, the performance of various precision wavemeters has been investigated in great detail [48, 49]. These studies indicate that measurements by a wavemeter similar to ours can show inaccuracies of up to ± 5 MHz which follow a non-linear, periodic pattern over a scanning range of $\approx 2\,\text{GHz}$ [48].

In our work, the wavemeter is used to lock the frequency of the fundamental wavelength to 560 nm. As a consequence of the frequency doubling to 280 nm, the effect of the wavemeter's relative inaccuracy is thus amplified by a factor of two. The resonances of $^{24}\text{Mg}^+$ and $^{26}\text{Mg}^+$ ions are approximately 12 GHz apart in their laboratory-frame frequencies. Hence, if the resonances of $^{24}\text{Mg}^+$ and $^{26}\text{Mg}^+$ ions happen to be close to opposite extremes in the wavemeter's deviation, a shift of up to 20 MHz could occur in either direction in the isotope shift $\nu_0^{24,26}$. For this reason, the systematic uncertainty of 12 MHz assigned above to our experiment's frequency scanning may potentially be caused entirely by the wavemeter.

4.4. Final result for $\nu_0^{24,26}$ and measurement accuracy of the apparatus

We obtain $\nu_0^{24,26} = 3081 \pm 4 \pm 17$ MHz for the isotope shift in the D2 transition between $^{24}\text{Mg}^+$ and $^{26}\text{Mg}^+$ ions. Here, the uncertainty is separated into statistical and systematic contributions. The latter consists of uncertainties due to ion's starting potential in the Paul trap (12 MHz, see Sec. 4.1.1) as well as the frequency-scanning methods (12 MHz, see Sec. 4.3). Both systematic uncertainties are added in quadrature. The measured value $\nu_0^{24,26}$ is in agreement with the more precise literature value. This demonstrates an accuracy of the present setup for conventional CLS at a level better than 20 MHz.

8

5. Conclusion and Outlook

As part of the developments towards the Multi Reflection Ion Apparatus for Collinear Laser Spectroscopy (MIRACLS), we have performed conventional, single- passage collinear laser spectrosocpy (CLS) in an MR-ToF device. In particular, the isotope shift of the well-known $3s\,^2\mathrm{S}_{1/2} \to 3p\,^2\mathrm{P}_{3/2}$ transition between $^{26}\mathrm{Mg}^+$ and $^{24}\mathrm{Mg}^+$ ions has been determined.

The measured isotope shift is in agreement with the more precise literature value. We have performed these measurements under varying experimental conditions to evaluate systematic uncertainties in our new apparatus.

One identified systematic uncertainty is due to the ions' starting potential in the Paul trap which influences the final ion beam energy. We estimate this uncertainty based on calculations of the axial potentials in the Paul trap. To reduce this uncertainty further, 'slower' ion extraction schemes from the Paul trap will be employed in future work.

Reflecting a second systematic uncertainty, a discrepancy between the results from Doppler tuning and laser scanning is observed. Its size is consistent with inaccuracies of the wavemeter. Ongoing CLS work performed on ions trapped in the MR-ToF device relies on laser scanning only. For this method, we assign a systematic uncertainty of 20 MHz in the isotope shift caused by the wavemeter, see Sec. 4.3. Ultimately, our implementation of laser scanning needs to be upgraded, as it has been shown to yield accurate isotope-shift results by other groups [46].

The present work also demonstrates that the use of a pulsed drift tube as a 'potential lift' in the ion acceleration severely affects a CLS measurement. In particular, a sizable difference in the isotope shift to the literature value is observed. This is associated with the high-voltage (HV) switching of the pulsed drift tube which inflates the ion beam energy in a non-trivial way. Although not relevant for the present result, the HV switching of electrode(s) is necessary for MR-ToF operation at MIRACLS, i.e., during ion capture into the ion trap. Ongoing work is hence dedicated to fully characterise the HV-switching process. Overall, the present work establishes that a measurement accuracy of about 20 MHz in isotope shifts is feasible in this new apparatus for conventional, single-passage CLS at an ion beam anergy of ≈ 1.5 keV. In a next step, we are performing CLS studies in the MIRACLS approach, i.e., by trapping the ions in the MR-ToF device. The comparison to the present results will allow us to quantify the influence of the MR-ToF operation on the CLS performance, especially in terms of the measurement accuracy as well as the sensitivity advantage of the multi-reflection scheme with respect to the present single-passage measurements.

6. Acknowledgments

References

[1] J. Bonn, G. Huber, H. Kluge, U. Köpf, L. Kugler, and E.-W. Otten, "Optical pumping of neutron deficient 187hg," *Physics Letters B*, vol. 36, no. 1, pp. 41–43, 1971.

[2] G. Bollen, P. Dabkiewicz, P. Egelhof, T. Hilberath, H. Kalinowsky, F. Kern, H. Schnatz, L. Schweikhard, H. Stolzenberg, R. B. Moore, H. J. Kluge, G. M. Temmer, and G. Ulm, "First absolute mass measurements of short-lived isotopes," *Hyperfine Interactions*, vol. 38, pp. 793–802, 12 1987.

[3] E. W. Otten, *Nuclear Radii and Moments of Unstable Isotopes*, pp. 517–638. Boston, MA: Springer US, 1989.

[4] H.-J. Kluge, "Precision measurements of masses of radioactive atoms using isolde and ion traps," *Physica Scripta*, vol. T22, pp. 85–89, 1 1988.

[5] K. Blaum, J. Dilling, and W. Nörtershäuser, "Precision atomic physics techniques for nuclear physics with radioactive beams," *Physica Scripta*, vol. 2013, no. T152, p. 014017, 2013.

[6] R. Neugart, J. Billowes, M. L. Bissell, K. Blaum, B. Cheal, K. T. Flanagan, G. Neyens, W. Nörtershäuser, and D. T. Yordanov, "Collinear laser spectroscopy at ISOLDE: new methods and highlights," *Journal of Physics G: Nuclear and Particle Physics*, vol. 44, p. 064002, apr 2017.

[7] J. Dilling, K. Blaum, M. Brodeur, and S. Eliseev, "Penning-trap mass measurements in atomic and nuclear physics," *Annual Review of Nuclear and Particle Science*, vol. 68, no. 1, pp. 45–74, 2018.

[8] W. R. Plaß, T. Dickel, U. Czok, H. Geissel, M. Petrick, K. Reinheimer, C. Scheidenberger, and M. I.Yavor, "Isobar separation by time-of-flight mass spectrometry for low-energy radioactive ion beam facilities," *Nuclear Instruments and Methods in Physics Research Section B: Beam Interactions with Materials and Atoms*, vol. 266, no. 19-20, pp. 4560 – 4564, 2008.

[9] A. Piechaczek, V. Shchepunov, H. K. Carter, J. C. Batchelder, E. F. Zganjar, S. N. Liddick, H. Wollnik, Y. Hu, and B. O. Griffith, "Development of a high resolution isobar separator for study of exotic decays," *Nuclear Instruments and Methods in Physics Research Section B: Beam Interactions with Materials and Atoms*, vol. 266, no. 19, pp. 4510–4514, 2008.

[10] P. Schury, K. Okada, S. Shchepunov, T. Sonoda, A. Takamine, M. Wada, H. Wollnik, and Y. Yamazaki, "Multi-reflection time-of-flight mass spectrograph for short-lived radioactive ions," *The European Physical Journal A*, vol. 42, no. 3, p. 343, 2009.

[11] R. Wolf, F. Wienholtz, D. Atanasov, D. Beck, K. Blaum, C. Borgmann, F. Herfurth, M. Kowalska, S. Kreim, Y. A. Litvinov, D. Lunney, V. Manea, D. Neidherr, M. Rosenbusch, L. Schweikhard, J. Stanja, and K. Zuber, "Isoltrap's multi-reflection time-of-flight mass separator/spectrometer," *International Journal of Mass Spectrometry*, vol. 349-350, pp. 123 – 133, 2013. 100 years of Mass Spectrometry.

[12] F. Wienholtz, D. Beck, K. Blaum, C. Borgmann, M. Breitenfeldt, R. B. Cakirli, S. George, F. Herfurth, J. D. Holt, M. Kowalska, S. Kreim, D. Lunney, V. Manea, J. Menéndez, D. Neidherr, M. Rosenbusch, L. Schweikhard, A. Schwenk, J. Simonis, J. Stanja, R. N. Wolf, and K. Zuber, "Masses of exotic calcium isotopes pin down nuclear forces," *Nature*, vol. 498, no. 7454, pp. 346–349, 2013.

[13] T. Dickel, W. Plaß, A. Becker, U. Czok, H. Geissel, E. Haettner, C. Jesch, W. Kinsel, M. Petrick, C. Scheidenberger, A. Simon, and M. Yavor, "A high-performance multiple-reflection time-of-flight mass spectrometer and isobar separator for the research with exotic nuclei," *Nuclear Instruments and Methods in Physics Research Section A: Accelerators, Spectrometers, Detectors and Associated Equipment*, vol. 777, pp. 172 – 188, 2015.

[14] C. Jesch, T. Dickel, W. R. Plaß, D. Short, S. Ayet San Andres, J. Dilling, H. Geissel, F. Greiner, J. Lang, K. G. Leach, W. Lippert, C. Scheidenberger, and M. I. Yavor, "The mr-tof-ms isobar separator for the titan facility at triumf," *Hyperfine Interactions*, vol. 235, no. 1, pp. 97–106, 2015.

[15] P. Chauveau, P. Delahaye, G. De France, S. El Abir, J. Lory, Y. Merrer, M. Rosenbusch, L. Schweikhard, and R. Wolf, "Pilgrim, a multi-reflection time-of-flight mass spectrometer for spiral2-s3 at ganil," *Nuclear Instruments and Methods in Physics Research Section B: Beam Interactions with Materials and Atoms*, vol. 376, pp. 211 – 215, 2016. Proceedings of the XVIIth International Conference on Electromagnetic Isotope Separators and Related Topics (EMIS2015), Grand Rapids, MI, U.S.A., 11-15 May 2015.

[16] B. Liu, M. Brodeur, D. Burdette, J. Kelly, T. Kim, J. Long, and P. O'Malley, "The performance of the commissioned notre dame multi-reflection time-of-flight mass spectrometer," *Nuclear Instruments and Methods in Physics Research Section A: Accelerators, Spectrometers, Detectors and Associated Equipment*, vol. 985, p. 164679, 2021.

[17] H. Wollnik and M. Przewloka, "Time-of-flight mass spectrometers with multiply reflected ion trajectories," *International Journal of Mass Spectrometry and Ion Processes*, vol. 96, no. 3, pp. 267 – 274, 1990.

[18] D. Zajfman, O. Heber, L. Vejby-Christensen, I. Ben-Itzhak, M. Rappaport, R. Fishman, and M. Dahan, "Electrostatic bottle for long-time storage of fast ion beams," *Phys. Rev. A*, vol. 55, pp. R1577–R1580, Mar 1997.

[19] W. H. Benner, "A gated electrostatic ion trap to repetitiously measure the charge and m/z of large electrospray ions," *Analytical Chemistry*, vol. 69, pp. 4162–4168, 10 1997.

[20] F. Wienholtz, D. Atanasov, S. Kreim, V. Manea, M. Rosenbusch, L. Schweikhard, A. Welker, and R. N. Wolf, "Towards ultrahigh-resolution multi-reflection time-of-flight mass spectrometry at isoltrap," in *Physica Scripta*, vol. 2015, p. 014068, IOP Publishing, 11 2015.

[21] T. Dickel, M. I. Yavor, J. Lang, W. R. Plaß, W. Lippert, H. Geissel, and C. Scheidenberger, "Dynamical time focus shift in multiple-reflection time-of-flight mass spectrometers," *International Journal of Mass Spectrometry*, vol. 412, pp. 1–7, 2017.

[22] E. Leistenschneider, M. P. Reiter, S. Ayet San Andrés, B. Kootte, J. D. Holt, P. Navrátil, C. Babcock, C. Barbieri, B. R. Barquest, J. Bergmann, J. Bollig, T. Brunner, E. Dunling, A. Finlay, H. Geissel, L. Graham, F. Greiner, H. Hergert, C. Hornung, C. Jesch, R. Klawitter, Y. Lan, D. Lascar, K. G. Leach, W. Lippert, J. E. McKay, S. F. Paul, A. Schwenk, D. Short, J. Simonis, V. Somà, R. Steinbrügge, S. R. Stroberg, R. Thompson, M. E. Wieser, C. Will, M. Yavor, C. Andreoiu, T. Dickel, I. Dillmann, G. Gwinner, W. R. Plaß, C. Scheidenberger, A. A. Kwiatkowski, and J. Dilling, "Dawning of the $n = 32$ shell closure seen through precision mass measurements of neutron-rich titanium isotopes," *Phys. Rev. Lett.*, vol. 120, p. 062503, Feb 2018.

[23] Y. Ito, P. Schury, M. Wada, F. Arai, H. Haba, Y. Hirayama, S. Ishizawa, D. Kaji, S. Kimura, H. Koura, M. MacCormick, H. Miyatake, J. Y. Moon, K. Morimoto, K. Morita, M. Mukai, I. Murray, T. Niwase, K. Okada, A. Ozawa, M. Rosenbusch, A. Takamine, T. Tanaka, Y. X. Watanabe, H. Wollnik, and S. Yamaki, "First direct mass measurements of nuclides around $z = 100$ with a multireflection time-of-flight mass spectrograph," *Phys. Rev. Lett.*, vol. 120, p. 152501, Apr 2018.

[24] S. Ayet San Andrés, C. Hornung, J. Ebert, W. R. Plaß, T. Dickel, H. Geissel, C. Scheidenberger, J. Bergmann, F. Greiner, E. Haettner, C. Jesch, W. Lippert, I. Mardor, I. Miskun, Z. Patyk, S. Pietri, A. Pihktelev, S. Purushothaman, M. P. Reiter, A.-K. Rink, H. Weick, M. I. Yavor, S. Bagchi, V. Charviakova, P. Constantin, M. Diwisch, A. Finlay, S. Kaur, R. Knöbel, J. Lang, B. Mei, I. D. Moore, J.-H. Otto, I. Pohjalainen, A. Prochazka, C. Rappold, M. Takechi, Y. K. Tanaka, J. S. Winfield, and X. Xu, "High-resolution, accurate multiple-reflection time-of-flight mass spectrometry for short-lived, exotic nuclei of a few events in their ground and low-lying isomeric states," *Phys. Rev. C*, vol. 99, p. 064313, Jun 2019.

[25] R. F. Garcia Ruiz, R. Berger, J. Billowes, C. L. Binnersley, M. L. Bissell, A. A. Breier, A. J. Brinson, K. Chrysalidis, T. E. Cocolios, B. S. Cooper, K. T. Flanagan, T. F. Giesen, R. P. de Groote, S. Franchoo, F. P. Gustafsson, T. A. Isaev, Á. Koszorús, G. Neyens, H. A. Perrett, C. M. Ricketts, S. Rothe, L. Schweikhard, A. R. Vernon, K. D. A. Wendt, F. Wienholtz, S. G. Wilkins, and X. F. Yang, "Spectroscopy of short-lived radioactive molecules," *Nature*, vol. 581, no. 7809, pp. 396–400, 2020.

[26] A. Gottberg, T. Mendonca, R. Luis, J. Ramos, C. Seiffert, S. Cimmino, S. Marzari, B. Crepieux, V. Manea, R. Wolf, F. Wienholtz, S. Kreim, V. Fedosseev, B. Marsh, S. Rothe, P. Vaz, J. Marques, and T. Stora, "Experimental tests of an advanced proton-to-neutron converter at isolde-cern," *Nuclear Instruments and Methods in Physics Research Section B: Beam Interactions with Materials and Atoms*, vol. 336, pp. 143–148, 2014.

[27] K. Chrysalidis, J. Ballof, C. E. Düllmann, V. N. Fedosseev, C. Granados, B. A. Marsh, Y. Martinez Palenzuela, J. P. Ramos, S. Rothe, T. Stora, and K. Wendt, "Developments towards the delivery of selenium ion beams at isolde," *The European Physical Journal A*, vol. 55, no. 10, p. 173, 2019.

[28] R. N. Wolf, D. Beck, K. Blaum, C. Böhm, C. Borgmann, M. Breitenfeldt, N. Chamel, S. Goriely, F. Herfurth, M. Kowalska, S. Kreim, D. Lunney, V. Manea, E. Minaya Ramirez, S. Naimi, D. Neidherr, M. Rosenbusch, L. Schweikhard, J. Stanja, F. Wienholtz, and K. Zuber, "Plumbing neutron stars to new depths with the binding energy of the exotic nuclide ^{82}Zn," *Phys. Rev. Lett.*, vol. 110, p. 041101, Jan 2013.

[29] B. A. Marsh, T. Day Goodacre, S. Sels, Y. Tsunoda, B. Andel, A. N. Andreyev, N. A. Althubiti, D. Atanasov, A. E. Barzakh, J. Billowes, K. Blaum, T. E. Cocolios, J. G. Cubiss, J. Dobaczewski, G. J. Farooq-Smith, D. V. Fedorov, V. N. Fedosseev, K. T. Flanagan, L. P. Gaffney, L. Ghys, M. Huyse, S. Kreim, D. Lunney, K. M. Lynch, V. Manea, Y. Martinez Palenzuela, P. L. Molkanov, T. Otsuka, A. Pastore, M. Rosenbusch, R. E. Rossel, S. Rothe, L. Schweikhard, M. D. Seliverstov, P. Spagnoletti, C. Van Beveren, P. Van Duppen, M. Veinhard, E. Verstraelen, A. Welker, K. Wendt, F. Wienholtz, R. N. Wolf, A. Zadvornaya, and K. Zuber, "Characterization of the shape-staggering effect in mercury nuclei," *Nature Physics*, vol. 14, no. 12, pp. 1163–1167, 2018.

[30] M. Rosenbusch, S. Kemnitz, R. Schneider, L. Schweikhard, R. Tschiersch, and R. N. Wolf, "Towards systematic investigations of space-charge phenomena in multi-reflection ion traps," *AIP Conference Proceedings*, vol. 1521, no. 1, pp. 53–62, 2013.

[31] M. Rosenbusch, P. Chauveau, P. Delahaye, G. Marx, L. Schweikhard, F. Wienholtz, and R. N. Wolf, "Delayed bunching for multi-reflection time-of-flight mass separation," *AIP Conference Proceedings*, vol. 1668, no. 1, p. 050001, 2015.

[32] F. M. Maier, P. Fischer, H. Heylen, V. Lagaki, S. Lechner, P. Plattner, S. Sels, F. Wienholtz, W. Nörtershäuser, L. Schweikhard, and S. Malbrunot-Ettenauer, "Simulations of a proof-of-principle experiment for collinear laser spectroscopy within a multi-reflection time-of-flight device," *Hyperfine Interactions*, vol. 240, no. 1, p. 54, 2019.

[33] S. Lechner, P. Fischer, H. Heylen, V. Lagaki, F. Maier, P. Plattner, M. Rosenbusch, S. Sels, F. Wienholtz, R. N. Wolf, W. Nörtershäuser, L. Schweikhard, and S. Malbrunot-Ettenauer, "Fluorescence detection as a new diagnostics tool for electrostatic ion beam traps," *Hyperfine Interactions*, vol. 240,

no. 1, p. 95, 2019.

[34] V. Lagaki, P. Fischer, H. Heylen, F. Hummer, S. Lechner, S. Sels, F. Maier, P. Plattner, M. Rosenbusch, F. Wienholtz, R. Wolf, W. Nörtershäuser, L. Schweikhard, and S. Malbrunot-Ettenauer, "Stray-light suppression for the miracls proof-of-principle experiment," *Acta Physica Polonica B*, vol. 51, pp. 571–576, (2020).

[35] S. Sels, P. Fischer, H. Heylen, V. Lagaki, S. Lechner, F. Maier, P. Plattner, M. Rosenbusch, F. Wienholtz, R. Wolf, W. Nörtershäuser, L. Schweikhard, and S. Malbrunot-Ettenauer, "First steps in the development of the multi ion reflection apparatus for collinear laser spectroscopy," *Nuclear Instruments and Methods in Physics Research Section B: Beam Interactions with Materials and Atoms*, vol. 463, pp. 310 – 314, 2020.

[36] T. Murböck, S. Schmidt, Z. Andelkovic, G. Birkl, W. Nörtershäuser, and M. Vogel, "A compact source for bunches of singly charged atomic ions," *Review of Scientific Instruments*, vol. 87, no. 4, p. 043302, 2016.

[37] K. Kreim, M. Bissell, J. Papuga, K. Blaum, M. D. Rydt, R. G. Ruiz, S. Goriely, H. Heylen, M. Kowalska, R. Neugart, G. Neyens, W. Nörtershäuser, M. Rajabali, R. S. Alarcón, H. Stroke, and D. Yordanov, "Nuclear charge radii of potassium isotopes beyond n=28," *Physics Letters B*, vol. 731, pp. 97 – 102, 2014.

[38] W. Gins, R. P. de Groote, M. L. Bissell, C. Granados Buitrago, R. Ferrer, K. M. Lynch, G. Neyens, and S. Sels, "Analysis of counting data: Development of the satlas python package," *Computer Physics Communications*, vol. 222, pp. 286–294, 2018.

[39] R. T. Birge, "The calculation of errors by the method of least squares," *Phys. Rev.*, vol. 40, pp. 207–227, Apr 1932.

[40] P. D. Group, P. A. Zyla, R. M. Barnett, J. Beringer, O. Dahl, D. A. Dwyer, D. E. Groom, C. J. Lin, K. S. Lugovsky, E. Pianori, D. J. Robinson, C. G. Wohl, W. M. Yao, K. Agashe, G. Aielli, B. C. Allanach, C. Amsler, M. Antonelli, E. C. Aschenauer, D. M. Asner, H. Baer, S. Banerjee, L. Baudis, C. W. Bauer, J. J. Beatty, V. I. Belousov, S. Bethke, A. Bettini, O. Biebel, K. M. Black, E. Blucher, O. Buchmuller, V. Burkert, M. A. Bychkov, R. N. Cahn, M. Carena, A. Ceccucci, A. Cerri, D. Chakraborty, R. S. Chivukula, G. Cowan, G. D'Ambrosio, T. Damour, D. de Florian, A. de Gouvêa, T. DeGrand, P. de Jong, G. Dissertori, B. A. Dobrescu, M. D'Onofrio, M. Doser, M. Drees, H. K. Dreiner, P. Eerola, U. Egede, S. Eidelman, J. Ellis, J. Erler, V. V. Ezhela, W. Fetscher, B. D. Fields, B. Foster, A. Freitas, H. Gallagher, L. Garren, H. J. Gerber, G. Gerbier, T. Gershon, Y. Gershtein, T. Gherghetta, A. A. Godizov, M. C. Gonzalez-Garcia, M. Goodman, C. Grab, A. V. Gritsan, C. Grojean, M. Grünewald, A. Gurtu, T. Gutsche, H. E. Haber, C. Hanhart, S. Hashimoto, Y. Hayato, A. Hebecker, S. Heinemeyer, B. Heltsley, J. J. Hernández-Rey, K. Hikasa, J. Hisano, A. Höcker, J. Holder, A. Holtkamp, J. Huston, T. Hyodo, K. F. Johnson, M. Kado, M. Karliner, U. F. Katz, M. Kenzie, V. A. Khoze, S. R. Klein, E. Klempt, R. V. Kowalewski, F. Krauss, M. Kreps, B. Krusche, Y. Kwon, O. Lahav, J. Laiho, L. P. Lellouch, J. Lesgourgues, A. R. Liddle, Z. Ligeti, C. Lippmann, T. M. Liss, L. Littenberg, C. Lourengo, S. B. Lugovsky, A. Lusiani, Y. Makida, F. Maltoni, T. Mannel, A. V. Manohar, W. J. Marciano, A. Masoni, J. Matthews, U. G. Meißner, M. Mikhasenko, D. J. Miller, D. Milstead, R. E. Mitchell, K. Mönig, P. Molaro, F. Moortgat, M. Moskovic, K. Nakamura, M. Narain, P. Nason, S. Navas, M. Neubert, P. Nevski, Y. Nir, K. A. Olive, C. Patrignani, J. A. Peacock, S. T. Petcov, V. A. Petrov, A. Pich, A. Piepke, A. Pomarol, S. Profumo, A. Quadt, K. Rabbertz, J. Rademacker, G. Raffelt, H. Ramani, M. Ramsey-Musolf, B. N. Ratcliff, P. Richardson, A. Ringwald, S. Roesler, S. Rolli, A. Romaniouk, L. J. Rosenberg, J. L. Rosner, G. Rybka, M. Ryskin, R. A. Ryutin, Y. Sakai, G. P. Salam, S. Sarkar, F. Sauli, O. Schneider, K. Scholberg, A. J. Schwartz, J. Schwiening, D. Scott, V. Sharma, S. R. Sharpe, T. Shutt,

M. Silari, T. Sjöstrand, P. Skands, T. Skwarnicki, G. F. Smoot, A. Soffer, M. S. Sozzi, S. Spanier, C. Spiering, A. Stahl, S. L. Stone, Y. Sumino, T. Sumiyoshi, M. J. Syphers, F. Takahashi, M. Tanabashi, J. Tanaka, M. Taševský, K. Terashi, J. Terning, U. Thoma, R. S. Thorne, L. Tiator, M. Titov, N. P. Tkachenko, D. R. Tovey, K. Trabelsi, P. Urquijo, G. Valencia, R. Van de Water, N. Varelas, G. Venanzoni, L. Verde, M. G. Vincter, P. Vogel, W. Vogelsang, A. Vogt, V. Vorobyev, S. P. Wakely, W. Walkowiak, C. W. Walter, D. Wands, M. O. Wascko, D. H. Weinberg, E. J. Weinberg, M. White, L. R. Wiencke, S. Willocq, C. L. Woody, R. L. Workman, M. Yokoyama, R. Yoshida, G. Zanderighi, G. P. Zeller, O. V. Zenin, R. Y. Zhu, S. L. Zhu, F. Zimmermann, J. Anderson, T. Basaglia, V. S. Lugovsky, P. Schaffner, and W. Zheng, "Review of Particle Physics," *Progress of Theoretical and Experimental Physics*, vol. 2020, 08 2020. 083C01.

[41] V. Batteiger, S. Knünz, M. Herrmann, G. Saathoff, H. A. Schüssler, B. Bernhardt, T. Wilken, R. Holzwarth, T. W. Hänsch, and T. Udem, "Precision spectroscopy of the $3s-3p$ fine-structure doublet in mg^+," *Phys. Rev. A*, vol. 80, p. 022503, Aug 2009.

[42] L. Fischer, "Bsc thesis," 2018.

[43] F. Hummer, "Bsc thesis," 2019.

[44] H. Frånberg, P. Delahaye, J. Billowes, K. Blaum, R. Catherall, F. Duval, O. Gianfrancesco, T. Giles, A. Jokinen, M. Lindroos, D. Lunney, E. Mane, and I. Podadera, "Off-line commissioning of the isolde cooler," *Nuclear Instruments and Methods in Physics Research Section B: Beam Interactions with Materials and Atoms*, vol. 266, no. 19, pp. 4502–4504, 2008. Proceedings of the XVth International Conference on Electromagnetic Isotope Separators and Techniques Related to their Applications.

[45] E. Mané, J. Billowes, K. Blaum, P. Campbell, B. Cheal, P. Delahaye, K. T. Flanagan, D. H. Forest, H. Franberg, C. Geppert, T. Giles, A. Jokinen, M. Kowalska, R. Neugart, G. Neyens, W. Nörtershäuser, I. Podadera, G. Tungate, P. Vingerhoets, and D. T. Yordanov, "An ion cooler-buncher for high-sensitivity collinear laser spectroscopy at isolde," *The European Physical Journal A*, vol. 42, no. 3, pp. 503–507, 2009.

[46] A. Koszorús, X. F. Yang, J. Billowes, C. L. Binnersley, M. L. Bissell, T. E. Cocolios, G. J. Farooq-Smith, R. P. de Groote, K. T. Flanagan, S. Franchoo, R. F. Garcia Ruiz, S. Geldhof, W. Gins, A. Kanellakopoulos, K. M. Lynch, G. Neyens, H. H. Stroke, A. R. Vernon, K. D. A. Wendt, and S. G. Wilkins, "Precision measurements of the charge radii of potassium isotopes," *Phys. Rev. C*, vol. 100, p. 034304, Sep 2019.

[47] Á. Koszorús, X. F. Yang, W. G. Jiang, S. J. Novario, S. W. Bai, J. Billowes, C. L. Binnersley, M. L. Bissell, T. E. Cocolios, B. S. Cooper, R. P. de Groote, A. Ekström, K. T. Flanagan, C. Forssén, S. Franchoo, R. F. G. Ruiz, F. P. Gustafsson, G. Hagen, G. R. Jansen, A. Kanellakopoulos, M. Kortelainen, W. Nazarewicz, G. Neyens, T. Papenbrock, P. G. Reinhard, C. M. Ricketts, B. K. Sahoo, A. R. Vernon, and S. G. Wilkins, "Charge radii of exotic potassium isotopes challenge nuclear theory and the magic character of n = 32," *Nature Physics*, 2021.

[48] M. Verlinde, K. Dockx, S. Geldhof, K. König, D. Studer, T. E. Cocolios, R. P. de Groote, R. Ferrer, Y. Kudryavtsev, T. Kieck, I. Moore, W. Nörtershäuser, S. Raeder, P. Van den Bergh, P. Van Duppen, and K. Wendt, "On the performance of wavelength meters: Part 1—consequences for medium-to-high-resolution laser spectroscopy," *Applied Physics B*, vol. 126, no. 5, p. 85, 2020.

[49] K. König, P. Imgram, J. Krämer, B. Maaß, K. Mohr, T. Ratajczyk, F. Sommer, and W. Nörtershäuser, "On the performance of wavelength meters: Part 2—frequency-comb based characterization for more accurate absolute wavelength determinations," *Applied Physics B*, vol. 126, no. 5, p. 86, 2020.

11

7.3 Stray-light suppression for the MIRACLS proof-of-principle experiment

STRAY-LIGHT SUPPRESSION FOR THE MIRACLS PROOF-OF-PRINCIPLE EXPERIMENT*

V. Lagaki[a,b], P. Fischer[b], H. Heylen[a], F. Hummer[c], S. Lechner[a,d]
S. Sels[a], F. Maier[c], P. Plattner[a,e], M. Rosenbusch[b,†]
F. Wienholtz[a,b,f], R.N. Wolf[b,‡], W. Nörtershäuser[f]
L. Schweikhard[b], S. Malbrunot-Ettenauer[a]

[a]ISOLDE, CERN, 1211 Geneve 23, Switzerland
[b]Institut für Physik, Universität Greifswald, 17487 Greifswald, Germany
[c]Johannes Kepler Universität Linz, Altenbergerstrasse 69, 4040 Linz, Austria
[d]Technische Universität Wien, Karlsplatz 13, 1040 Wien, Austria
[e]Universität Innsbruck, Innrain 52, 6020 Innsbruck, Austria
[f]Inst. f. Physik, TU Darmstadt, Schlossgartenstr. 9, 64289 Darmstadt, Germany

The Multi-Ion Reflection Apparatus for Collinear Laser Spectroscopy (MIRACLS), currently under development at ISOLDE/CERN, aims to combine the high resolution of fluorescence-based collinear laser spectroscopy (CLS) with a high sensitivity. This will be achieved by confining 30-keV ion bunches in a Multi-Reflection Time-of-Flight (MR-ToF) device which allows laser spectroscopic probing for several thousand times. An MR-ToF setup operating at $\sim 1.5\,\text{keV}$ beam energy has been adapted for a proof-of-principle experiment. Thus, efforts had to be undertaken to reduce the laser stray light as the leading source of background of this apparatus, not originally designed for CLS. These measures enabled CLS of $^{24,26}\text{Mg}^+$ ions in single-path mode, *i.e.* without ion trapping, which is the reference point to gauge the gain in sensitivity of the MIRACLS technique.

1. Introduction

Collinear laser spectroscopy (CLS) is a powerful tool to measure nuclear properties such as spins, electromagnetic moments and differences in mean-square charge radii of short-lived radionuclides via their hyperfine spectrum [1–4]. For these measurements, a narrow-band laser beam

---

* Presented at the XXXVI Mazurian Lakes Conference on Physics, Piaski, Poland, September 1–7, 2019.

† Present address: RIKEN Nishina Center, Wako, Saitama, Japan.

‡ Present address: Faculty of Science, University of Sydney, Australia.

is (anti-)collinearly overlapped with a fast beam of radionuclides. When the Doppler-shifted frequency of the laser beam matches the selected electronic transition frequency, the laser-excited atom or ion emits fluorescence light which can be monitored by photon detectors in an optical detection region.

In CLS, beam energies of $\geq 30\,\text{keV}$ are used to minimize the Doppler broadening, which provides high spectral resolution, approaching the natural linewidth of the optical transition [4]. In order to increase the signal-to-noise ratio, CLS is performed with bunched beams [5]. Nevertheless, its fluorescence-light detection limits the applicability to nuclides with yields of at least a few thousand ions/s, depending on the specific case and spectroscopic transitions. In fact, the "effective laser probing" and observation time for fluorescence lasts at most a few microseconds when the bunch of radionuclides passes the optical detection region. This is in contrast to the nuclides' half lives which range from milliseconds to seconds and longer at low-energy branches of radioactive ion beam (RIB) facilities.

Matching the observation time to the nuclides' lifetimes would extend the reach of CLS to the most exotic nuclides available at today's RIB facilities. To this end, the Multi-Ion Reflection Apparatus for CLS (MIRACLS) is currently under development at ISOLDE/CERN. By repeatedly reflecting the ion bunch between two electrostatic mirrors of a Multi-Reflection Time-of-Flight (MR-ToF) device, the laser beam probes the ions during each revolution. Compared to conventional CLS, the observation time is therefore multiplied by the number of revolutions as well.

To demonstrate the MIRACLS technique, a low-energy MR-ToF device [6] has been adapted for CLS [7–9]. In the following, we describe the measures taken to reduce the laser-induced stray light which dominates the background in the fluorescence signal. As a result, conventional CLS, *i.e.* without ion storage, has been performed with $^{24,26}\text{Mg}^+$ ions.

2. The proof-of-principle experimental setup for MIRACLS

As a more detailed discussion can be found in Ref. [7], the description of the experimental setup (see Fig. 1) is limited to aspects relevant for the present work. A continuous beam of $^{24-26}\text{Mg}^+$ ions is captured in a He-buffer-gas filled Paul trap which provides well-defined ion bunches of $\sim 464\,\text{eV}$ beam energy. After passing an electrostatic quadrupole bender, the ions enter the MR-ToF region. In order to establish conventional CLS, the ions are not stored in the MR-ToF device for the present measurements. Thus, the MR-ToF mirror electrodes are all grounded. Its central drift tube is biased to $-1010\,\text{V}$ for an ion beam energy of $\sim 1.474\,\text{keV}$ which is comparable to previous MR-ToF operation at this setup [7–9].
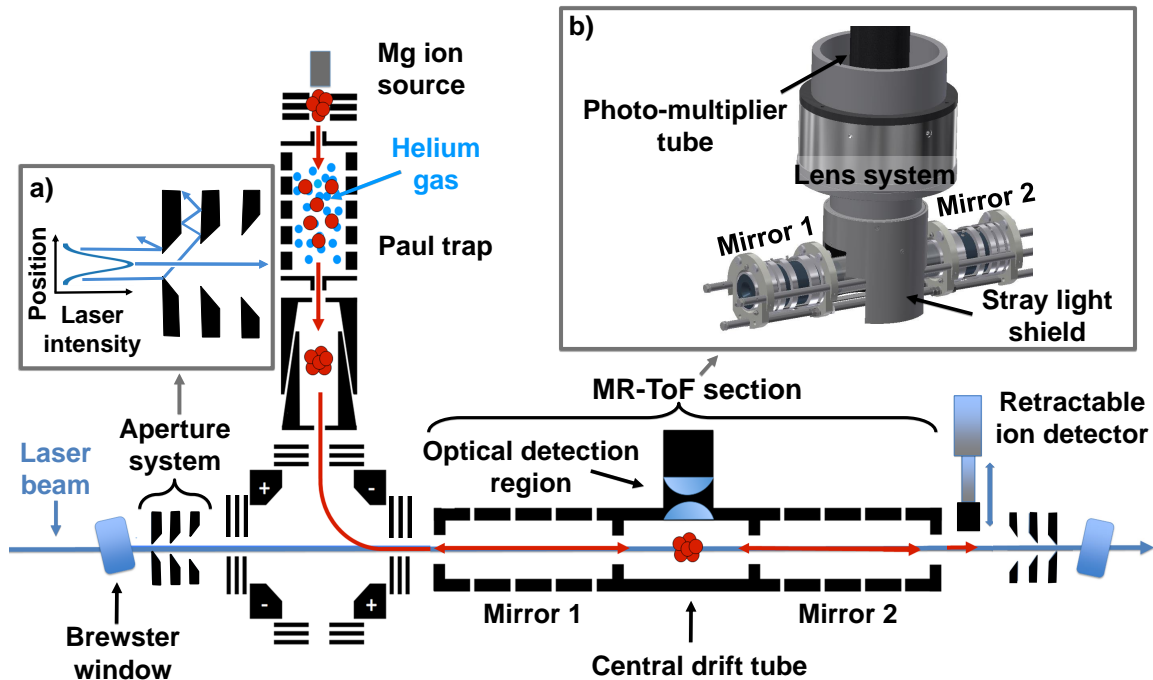
Fig. 1. Simplified schematics of the MIRACLS proof-of-principle experiment with close-up insets of the laser-entrance aperture system (a) and the stray light shield of the optical detection region (b). For details, see the text.

In the optical detection region located at the central drift tube, the fluorescent light is guided onto a photomultiplier tube by an optical lens system [10]. The photoexcitation of Mg^+ ions itself is achieved with a continuous-wave laser beam of $\sim 280\,nm$ wavelength [7] which enters the setup through a Brewster-angled quartz window to minimise reflections. The laser and ion beams are collinearly overlapped along the MR-ToF axis. A retractable ion detector is located downstream of the MR-ToF device for beam diagnostics and allows the estimation of the number of ions in an ion bunch [11].

3. Stray-light suppression

In order to perform efficient CLS with a high signal-to-noise ratio, the background-photon rate in the optical detection region has to be minimised. The leading source of this photon background is laser stray light, for example, light scattered off components in the beam line, which finds its way into the photodetector. Therefore, the photon background is reduced by decreasing the scattered laser light reaching the detector. In the MIRACLS proof-of-principle setup, this is achieved by a lens system in front of the photomultiplier tube, similar to what is used at the COLLAPS beamline at ISOLDE [10], and by a stray light shield around the optical detection region. These are designed to block out photons which are geometrically not originating from the ions in the optical detection region, while not reduc-

ing the signal of fluorescence light. Additionally, to prevent the tails of the laser-beam profile from scattering on elements inside the MR-ToF device, aperture sets are installed next to the laser entrance and exit windows. Each set consists of three apertures with inner diameters of 6, 8 and 10 mm. It is designed in such a way that laser light scattering from the first aperture hits the next apertures rather than propagating into the optical detection region (see Fig. 1 (a)). Since the diameters are smaller than the smallest diameter of any MR-ToF element (12 mm), the scattered light inside of the MR-ToF device is significantly reduced. Finally, scattered light is further minimized by reducing the reflectance of surfaces which are potentially hit by photons of the laser beam. Typically, this is achieved by coating the inside of the setup with a highly light-absorbing black paint. However, MR-ToF operation requires excellent UHV conditions which is often in conflict with outgassing rates of conventional black-coloured paints. As a compromise, surfaces with photon-absorbing black colour (*Tetenal* camera varnish spray) are introduced in the MIRACLS' proof-of-principle setup exclusively at the most critical places, *i.e.* the apertures and the stray light shield.

No degradation of the vacuum quality, in the range of 10^{-7} mbar, is observed at the vacuum gauges with the black color applied on the aforementioned components. As outgassing from the blackened surfaces may locally lead to higher pressures, we investigate the photon-background rate as a function of vacuum quality. This is achieved by turning the turbo pumps of the setup off until a prevacuum pressure is reached. Note that for higher pressures ($> 10^{-2}$ mbar), once the refractive index changes, the laser beam does not remain aligned with the MR-ToF axis. For MR-ToF operation at the best achievable vacuum quality, the detected photon rate is unrelated to the exact pressure. Only at pressure readings above 10^{-5} mbar an increase in the photon rate is observed.

The remaining amount of stray light at the optical detection region is quantified by sending a laser beam of ~ 0.6 mW and ~ 280 nm in wavelength through the apparatus. Under these conditions, a photon rate of typically 40–100 kHz depending, among others, on the laser-beam size is observed at the photo-multiplier tube (*ET Enterprises 9829QSA*). When the laser is blocked, this count-rate drops to a few kHz which is the detector's dark count-rate. Although the achieved photon rate is still more than an order of magnitude worse compared to the (almost) identical lens system at COLLAPS, it is sufficiently low to perform single-pass laser spectroscopy.

To demonstrate CLS at this setup, the laser wavelength is scanned without storing the ions in the MR-ToF device. The resulting resonance spectra of the D2 line of ^{24,26}Mg$^+$ ions are shown in Fig. 2 (a) and Fig. 2 (c). The ratio in the integrated signal intensities corresponds to the natural abundances of the magnesium isotopes. In the present study, a single-ion bunch consists

of a few thousand ^{24}Mg$^+$ ions per measurement cycle. Assuming that the width of the resonance is entirely due to Doppler broadening, the observed FWHM of 230(10) MHz corresponds at this beam energy to an energy spread of $\approx 1.7(1)$ eV. The photon intensity on resonance as a function of time is illustrated in Fig. 2 (b). Note the peak width of $\sim 0.5\,\mu$s which allows narrow gating in time of flight. Compared to typically a few microseconds as seen, for example, at the COLLAPS beam line at ISOLDE, this partially compensates for the higher stray-light photon rate in this work.
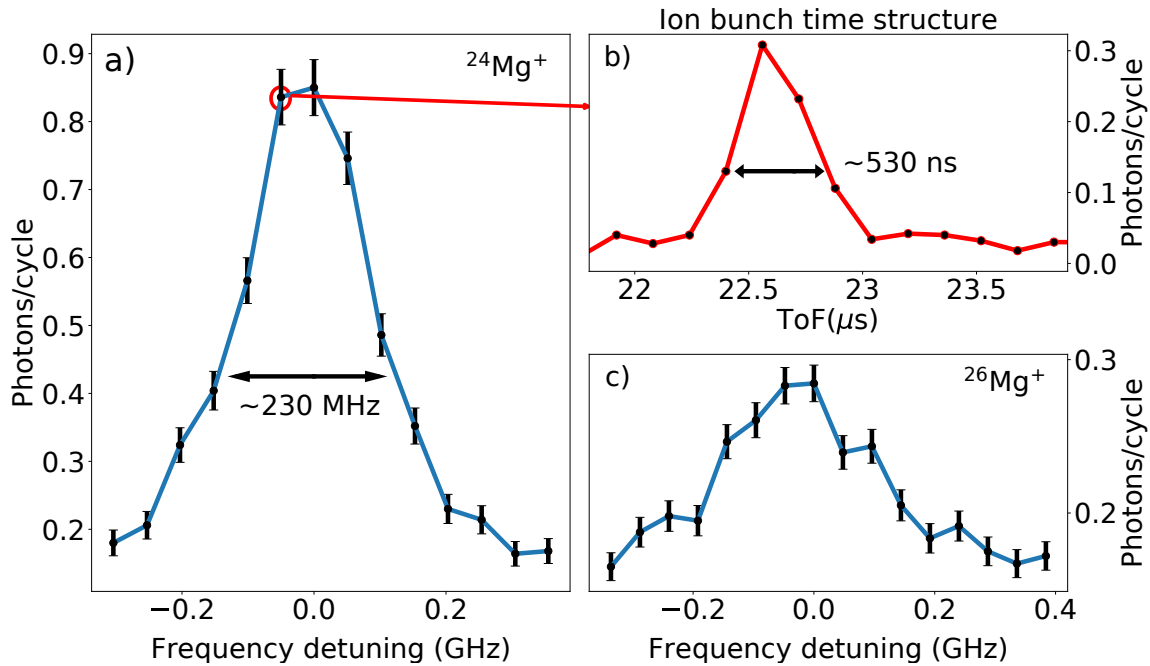
Fig. 2. (a) D2-line resonance of ^{24}Mg$^+$ ions averaged over 500 measurement cycles per frequency step. (b) Fluorescence signal over time of flight (ToF) for the resonance frequency of ^{24}Mg$^+$ ions. (c) Resonance of ^{26}Mg$^+$ ions averaged over 2 000 measurement cycles.

4. Conclusion and outlook

MIRACLS is a novel technique under development at ISOLDE/CERN which aims to combine the high resolution of conventional fluorescence-based collinear laser spectroscopy (CLS) with a high sensitivity by repeatedly probing the same ion bunch. Within a low-energy Multi-Reflection Time-of-Flight (MR-ToF) setup, conventional CLS has been performed on stable Mg$^+$ ions. This is achieved thanks to the implementation of aperture sets and a stray light shield around the optical detection region, all coated with highly absorbing black paint, resulting in a sufficiently low background of laser stray light for the purpose of the proof-of-principle experiment. Moreover, the advantages of short temporal ion bunches for background suppres-

sion have been illustrated. Both, this and the reduction of the longitudinal emittance in CLS, *i.e.* a simultaneous decrease of the energy spread, will be addressed at MIRACLS by a cryogenic Paul trap for optimal beam preparation in the future 30-keV setup. In the future, an adjustable aperture at the entrance of the MR-ToF device may further reduce the laser stray light and will facilitate better alignment of laser and ion beams. Finally, development is ongoing towards versatile UHV compatible and highly UV absorbing coatings for more advanced stray-light suppression.

REFERENCES

[1] K. Blaum *et al.*, *Phys. Scr.* **T152**, 014017 (2013).

[2] P. Campbell *et al.*, *Prog. Part. Nucl. Phys.* **86**, 127 (2016).

[3] R. Neugart *et al.*, *J. Phys. G: Nucl. Part. Phys.* **44**, 064002 (2017).

[4] S.L. Kaufman, *Opt. Commun.* **17**, 309 (1976).

[5] A. Nieminem *et al.*, *Phys. Rev. Lett.* **88**, 0948801 (2002).

[6] M. Rosenbusch *et al.*, *AIP Conf. Proc.* **1521**, 53 (2013).

[7] S. Sels *et al.*, *Nucl. Instrum. Methods Phys. Res. B* **463**, 310 (2020).

[8] F.M. Maier *et al.*, *Hyperfine Interact.* **240**, 54 (2019).

[9] S. Lechner *et al.*, *Hyperfine Interact.* **240**, 95 (2019).

[10] K. Kreim, Ph.D. Thesis, Ruprecht-Karls-Universität Heidelberg, 2013.

[11] F. Hummer, B.Sc. Thesis, Johannes Kepler University Linz, 2019.

7.4 First steps in the development of the Multi Ion Reflection Apparatus for Collinear Laser Spectroscopy
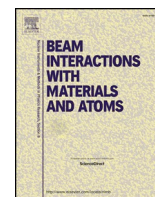
First steps in the development of the Multi Ion Reflection Apparatus for Collinear Laser Spectroscopy

S. Sels[a,*], P. Fischer[b], H. Heylen[a], V. Lagaki[a,b], S. Lechner[a,e], F.M. Maier[a,c], P. Plattner[a,f], M. Rosenbusch[b,1], F. Wienholtz[a,b], R.N. Wolf[b,2], W. Nörtershäuser[d], L. Schweikhard[b], S. Malbrunot-Ettenauer[a]

[a] ISOLDE, CERN Experimental Physics Department, CH-1211 Geneva 23, Switzerland
[b] Institut für Physik, Universität Greifswald, 17487 Greifswald, Germany
[c] Johannes Kepler University Linz, Altenbergerstrasse 69, 4040 Linz, Austria
[d] Technische Universität Darmstadt, Karolinenpl.5, 64289 Darmstadt, Germany
[e] Technische Universität Wien, Karlsplatz 13, 1040 Wien, Austria
[f] Universität Innsbruck, Innrain 52, 6020 Innsbruck, Austria

ARTICLE INFO

ABSTRACT

Collinear laser spectroscopy (CLS) has been combined with the multi-reflection time-of-flight (MR-ToF) technique. To this end, a photodetection system has been implemented at the drift region of a MR-ToF apparatus and a laser beam has been sent along the path of the ions that are stored between the two ion-optical mirrors. The main goal of the present proof-of-principle (PoP) experiments, is the confirmation of the expected increase in sensitivity compared to conventional fluorescence-based CLS due to the repeated probing of the trapped ion bunches. The novel method will be used for the precise measurement of nuclear ground- and isomeric-state properties of exotic nuclei with low production yields at radioactive ion-beam facilities. A significant sensitivity improvement of CLS is expected, depending on the half-life and mass of the nuclide of interest. The status of the PoP setup and future improvements are discussed.

1. Introduction

Collinear laser spectroscopy (CLS) is a well-established technique to measure ground- and isomeric-state properties of radioactive nuclides [1,2]. From the hyperfine splitting (HFS) and isotope shift (IS) of optical transitions for different isotopes in an isotopic chain, one can deduce the electromagnetic moments and mean-square charge-radii differences in a nuclear-model-independent way. In conventional, fluorescence-based CLS at radioactive ion-beam (RIB) facilities such as ISOLDE at CERN [3,4], beams of radioactive isotopes are produced and accelerated to an energy of several tens of keV. These beams of singly-charged ions or neutralized atoms are collinearly (or anticollinearly) overlapped with a narrow-band, continuous-wave laser that resonantly excites the optical transitions. Usually, the frequency observed by the atoms or ions is Doppler tuned by adjusting the ion-bunch acceleration

voltage, while keeping the laser-frequency fixed in the lab frame. Fluorescence photons emitted by the laser-excited ions or atoms passing an optical detection region (ODR) are observed by use of photomultiplier tubes. After passing the ODR only once, with an interaction time of only a few microseconds [5], the ion bunch is usually sent to a beam dump. However, ISOL facilities such as ISOLDE deliver radioactive nuclides with half-lives ranging from about a millisecond up to several years or even stable [6]. This causes a large mismatch between nuclear lifetime and observation time, which leaves room for improvement of the experimental sensitivity. Such an improvement is crucial if one wishes to extend high-resolution CLS measurements to exotic nuclides with very low production yields that are currently out of reach for conventional CLS.

The development of a Multi Ion Reflection Apparatus for Collinear Laser Spectroscopy (MIRACLS) at CERN aims to increase the sensitivity

of conventional CLS by addressing this mismatch between nuclear lifetime and observation time. By reflecting the ion bunches back and forth between the two electrostatic mirrors of a Multi-Reflection Time-of-Flight (MR-ToF) device [7–16], they can be probed by the laser beam during each revolution. At today's radioactive ion beam facilities, MR-ToF devices are mostly used for mass spectrometry or mass separation. By confining ion bunches for several thousand revolutions, their time-of-flight (ToF) is increased and even ion species with minute mass differences separate over time. MR-ToF devices reach mass-resolving powers $R = \frac{m}{\Delta m}$ of several hundred thousands in less than 30 ms [17–19].

To date, MR-ToF devices usually work at ion energies of $\approx 1–2$ keV [17,20,19,10]. However, in order to preserve the high spectroscopic resolution of conventional CLS, the final MIRALCS setup will operate at typical CLS-energies of $E \geqslant 30$ keV. This allows one to approach the natural line widths, as the Doppler line-width of the atomic transition δ_f scales with the ion-beam energy as $\delta_f \propto \delta_E / \sqrt{E}$, where δ_E represents the ions' energy spread [21]. In the current, first stage of the project, a proof-of-principle (PoP) setup has been assembled by adapting a low-energy MR-ToF device [22–24] for preliminary CLS tests. This PoP setup will be utilized to experimentally demonstrate the MIRACLS concept, further develop the technique, and benchmark simulations [25] that are employed to design the future 30-keV apparatus.

2. Proof-of-principle setup

A schematic of the offline PoP setup is shown in Fig. 1. An electron-impact ion source (adapted from [26]), floated to ≈ 250 V, provides a continuous ion beam of stable magnesium. The beam is focused into a helium-filled radio-frequency quadrupole (RFQ) cooler-buncher, where the ions are cooled and accumulated. After being released from the RFQ, the ion bunch is accelerated by a crown-shaped acceleration electrode and pulsed drift tube (PDT) to an energy of ≈ 2 keV, before it is deflected onto the MR-ToF axis by a $90°$ quadrupole bender. The ions enter the MR-ToF apparatus, where they are decelerated to ≈ 1.3 keV and captured using the in-trap-lift technique [27,28]. During the time the ion bunches are trapped, they perform multiple revolutions between the two electrostatic mirrors of the MR-ToF device. Each mirror consists of 4 cylindrical electrodes to which electric potentials are applied. These are optimized with respect to ion trapping and focusing, while keeping the central drift region of the instrument free of fringe fields [25]. This central drift section is fully surrounded by a mesh electrode that defines the electrical potential. This mesh electrode has a locally-adjusted wire-spacing which provides an enhanced photon transparency near the ODR. As part of the ODR, an optical lens system [29] and a photomultiplier tube are mounted above the mesh electrode to detect fluorescence photons of laser-excited Mg^+ ions. The in-trap lift

mechanism is also used to eject the ion bunches from the MR-ToF device [27,30]. The extracted bunches pass a second $90°$ quadrupole bender and can be recorded on a multi-channel plate detector (MCP) for monitoring and beam-tuning purposes.

The laser beam for photoexcitation enters the setup through a quartz, Brewster-angled window and is overlapped with the axis of the MR-ToF device. When the laser frequency is in resonance with a Doppler-shifted optical transition of the 1.3-keV ion bunch fluorescence photons are detected in the PMT. By scanning the laser frequency and monitoring the photon signal, the hyperfine-structure resonances of the trapped ions can be recorded. The improvement with respect to conventional CLS is obvious, as the ion bunches pass the ODR during every revolution in the MR-ToF device, thereby increasing the photon counts and thus the statistical significance of the data with every additional passing.

Stable magnesium ions will be used as an ideal test-case, since the even-even isotopes, $^{24,26}\text{Mg}$, have no hyperfine splitting of the fine-structure levels due to their $I = 0$ nuclear spin and the D_1 and D_2 transitions at about 280 nm both form a closed, two-level system. This avoids that, after several revolutions in the MR-ToF device, the population is optically pumped towards a hyperfine level or another fine-structure state which is not probed by the laser and which would therefore result in a decrease in photosignal. Repopulation techniques for more complicated ionic systems will be developed at a later stage of the project.

One of the major advances in CLS on radioactive ions was the introduction of bunched beams to increase the signal-to-noise ratio [31,32]. The reduction is due to the possibility of gating the data acquisition only on the time when the ion bunch passes the ODR. Besides bunching of the ion beam, several other measures are taken in order to further reduce the influence of background in MIRACLS' PoP setup, which, due to its history, was not designed to minimize sources of laser scattering as otherwise imperative for efficient CLS. Hence, a Brewster window and set of three apertures are mounted on either side of the setup as optical ports (see Fig. 1). Together with a stray-light shield painted in photon-absorbing black paint, placed around the ODR, these modifications reduce the laser-induced background by more than an order of magnitude, without noticeably affecting the quality of the vacuum. Indeed, a high vacuum better than 10^{-7} mbar is preferential to reduce the amount of stray-light scattering centers and collisional-induced excitation. Moreover, collisions with residual gas particles has been identified as a major reason for ion losses in the setup. The latter motivates a series of UHV upgrades foreseen for the near future, in particular the better separation of the vacuum section of the MR-ToF device from the buffer-gas filled cooler-buncher.

3. Laser setup

The laser beam at 280 nm, used to resonantly excite the D_2-like ($3\,^2S_{1/2} \rightarrow 3\,^2P_{3/2}$) transition in magnesium ions, is generated using the setup shown in Fig. 2. A Spectra Physics 20-W Millennia eV laser, produces the 532-nm laser light used to pump a Sirah MATISSE laser operated with Rhodamine 560 dye dissolved in ethylene glycol. The 560-nm output light is coupled into a high-power, large-mode-area optical fiber (LMA-15 single-mode 15 μm core fiber). Prior to the fiber coupling, a combination of a $\lambda/2$-plate and a polarizing beam splitter allows for a variable laser-beam intensity during the optimization of the fiber coupling. An optical isolator removes undesirable effects on the dye-laser locking caused by back reflections from the fiber coupler.

The approximately 25-m long optical fiber transports the laser light from the laser laboratory to the MR-ToF lab with a typical efficiency of 50–70%. The laser light leaving an optical fiber is usually randomly polarized. As unwanted circular polarization would lead to losses (at a second polarizing beam splitter cube further downstream) a quarter wave plate is installed behind the fiber to remove any undesired portion of the polarization. Then, the second-harmonic at 280 nm is generated
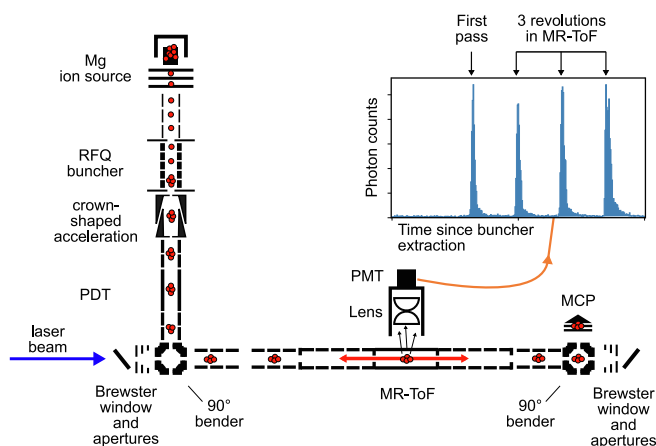

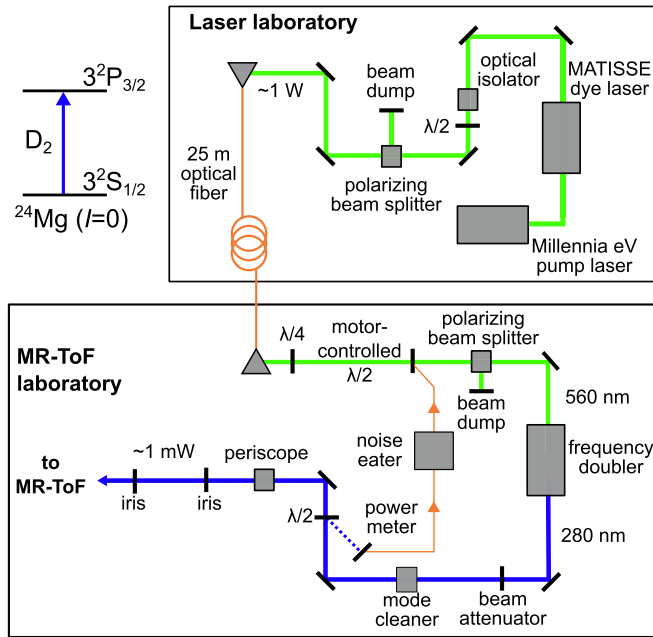**Fig. 1.** Schematic of the MIRACLS proof-of-principle setup. See text for details.

Fig. 2. Schematic of the laser setup at MIRACLS PoP experiment. See text for details.

in a BBO crystal by use of a Wavetrain frequency doubler. A mode cleaner with a 15-μm pinhole is used to remove side fringes originating from the second-harmonic generating process and to obtain a pure Gaussian TEM00 beam profile. This reduces significantly stray-light caused by spatially more extended mode contributions. The laser power introduced into the MR-ToF vacuum setup can be adjusted with a beam attenuator in front of the mode cleaner. The power level is additionally stabilized by guiding the back reflection of a $\lambda/2$-plate onto a power meter. Its output is used as the process variable of a PI feedback-loop that rotates a motor-controlled $\lambda/2$-plate in front of the frequency doubler (see Fig. 2).

Finally, the 2-mm diameter laser beam is guided through a periscope and two irises to the Brewster windows where it enters the vacuum chamber (see Fig. 1). The polarization is adjusted to minimize reflections from the Brewster windows using the previously mentioned $\lambda/2$-plate behind the mode cleaner.

To record the hyperfine structure of an isotope, the laser frequency is scanned across the relevant frequency range, while the laser is stabilized to a High-Finesse WSU-10 wavelength meter. The wavelength meter is regularly calibrated using a diode laser that is locked to the ^{87}Rb ($S_{1/2} \rightarrow P_{3/2}$) hyperfine transition at approximately 780 nm. The option of scanning the laser frequency rather than scanning the ion-bunch energy is preferred, since the latter would also change the ion trajectories inside the MR-ToF device.

4. First signals

To demonstrate that CLS can be performed within the MIRALCS PoP setup, a resonance spectrum of ^{24}Mg$^+$ ions passing through the ODR once, i.e. in the conventional collinear laser-spectroscopy mode without MR-ToF operation, is shown in Fig. 3. SIMION [33] simulations of the ion transport from the RFQ to the MR-ToF device show that Doppler broadening is the main contributing process to the total linewidth of the measured spectrum at energies of 1.3 keV [25] as the natural line width is only 42 MHz [34]. A total broadening of $\approx$370 MHz is expected, in accordance with the experimental observation of about 400 MHz as depicted in Fig. 3. This spectrum was obtained after tuning of parameters for the ion injection into the MR-ToF device and by working in a regime below the space-charge limit. This
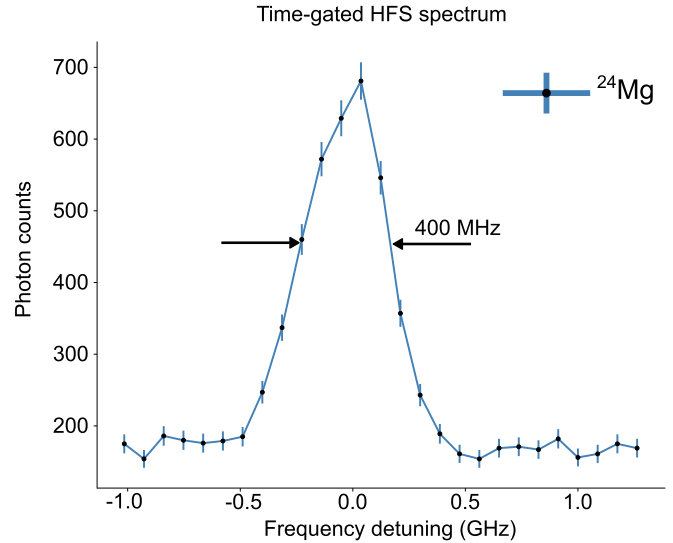

Fig. 3. Example of a resonance of ^{24}Mg$^+$ at a kinetic energy of $\sim$ 1.55 keV obtained for a single passage through the ODR in the center of the MR-ToF device. The photon counts of 300 ion bunches have been added for each probe frequency. The data for this spectrum was gated on the passage of the ion bunch as described in Section 2.

resonance shows a slight tailing at the low-frequency side. Most probably, this is related to the distribution of angles of the ion trajectories with respect to the optical axis due to the transversal ion-beam emittance. Each angular deviation α contributes to additional photon counts on the lower-energy tail of the observed spectrum due to the Doppler-shifted laser frequency f in the rest frame of the ions. This frequency f is described as

$$f = f_0 \frac{\sqrt{1 - \left(\frac{v}{c}\right)^2}}{1 - \frac{v_x}{c}},$$

where c represents the speed of light, v the total velocity of the ions, and $v_x = v \cos\alpha$ the velocity component along the MR-ToF axis.

Examples of the resonant fluorescence signal as a function of time are presented in Fig. 4, once for single-pass operation (blue line) as in conventional CLS and once for MR-ToF operation where the ions are trapped for three revolutions (orange line) and thus produce three further fluorescence signals when passing in front of the ODR. When the laser is detuned, the fluorescence signals disappear and only the
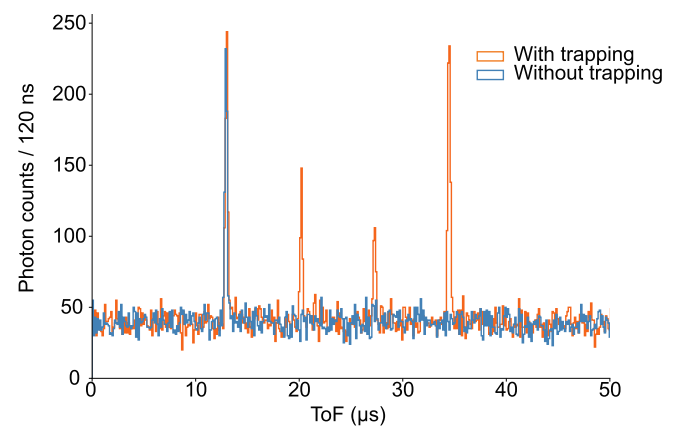

Fig. 4. Photomultiplier count rates as a function of time with trapping, i.e. MR-ToF operation (orange) and without (blue), i.e. single-pass mode. The laser frequency is tuned to resonance. This provides a direct comparison between sensitivity in conventional CLS and in the MIRACLS approach. The photon counts of 300 ion bunches have been added.
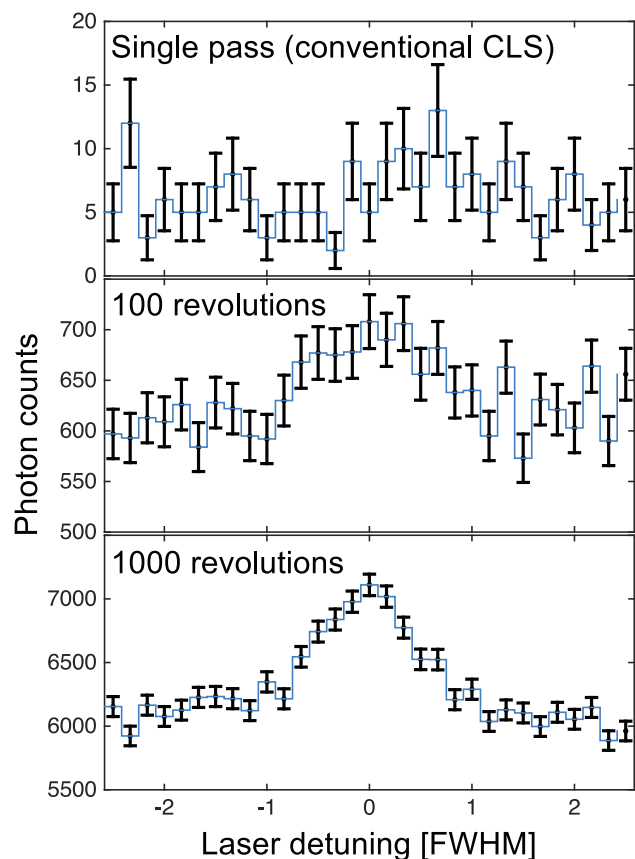
Fig. 5. Simulated photon counts for an ion bunch passing the ODR only once (top) and for 100 and 1000 revolutions in the MR-ToF device (middle and bottom, respectively). Ion losses from radioactive decay or trapping in the MR-ToF device are not included in this representation.

background level is left (not shown). Hence, the multiple passages of the ions through the ODR as enabled by the MIRACLS approach substantially increase the number of photon counts and thus the statistical significance of the collected data.

We note in passing that the fluorescence signal fluctuates during the first revolutions in the MR-ToF apparatus. While this phenomenon is out of the scope of the present study we have observed a stabilization of the signal at higher revolution numbers. The signal-height fluctuations during the first revolutions after ion injection depend very strongly on the injection parameters and similar observations are known from the ion signal as a function of revolution number at other MR-ToF devices [35]. From the recurrence of the peak intensity it can be deduced that the ion beam is not lost, but occasionally merely on a trajectory not overlapping with the laser beam. When the ion bunch is tuned into the MR-ToF device differently, this effect can be reduced, as shown for instance in the inset of Fig. 1, but it is difficult to eliminate this completely. Other than just the signal height, the evolution and control of other signal parameter are being studied as a function of revolution number in the PoP setup (e.g. signal-width) [36].

As conventional MR-ToF operation provides ion trapping for a few thousand revolutions [17], a significant increase in experimental sensitivity is anticipated for MIRACLS. It will make it possible to isolate the CLS signal even for exotic nuclides with low production yields, for which a conventional, i.e. single-pass, signal would be buried in the background. This is simulated in Fig. 5, for a case where single passage through the ODR cannot produce an identifiable signal (top), but where a signal-to-noise ratio of about 1 is reached after 100 revolutions (middle). Consequently, a clear signal with good statistics is obtained after about 1000 revolutions (bottom).

5. Outlook

The possibilities offered by the MIRACLS technique will be further explored in the future, first in the offline PoP setup described above, later in the 30-keV device that is currently being designed. Early anticipated advances include trapping of the ion bunches for several thousands of revolutions to increase the improvement factor of MIRACLS. The development of the centroid, spectral linewidth and signal strength with the number of revolution periods will be studied for these extended trapping times. As a first test case, the well-known isotope shifts of stable magnesium isotopes will be measured and compared to the literature values to investigate the accuracy that can be reached with the PoP apparatus of MIRACLS. It will later be extended to other elements. In its first stage, the technique would be most useful for closed, two-level transitions. In order to expand towards more general cases, research on the redistribution of excited states of the ion ensemble using additional lasers will be performed. Another advance could be the addition of a second laser to perform simultaneous collinear and anticollinear measurements as was recently demonstrated for beryllium isotopes [37,38] and applied at even higher accuracy for barium isotopes [39]. This removes the uncertainty in the isotope-shift measurements induced by the imperfect knowledge of the ion beam energy. Furthermore, the possibility of performing mass measurements or mass separation while simultaneously performing laser spectroscopy will be studied. It is expected that, besides CLS, also mass separation of rare isotopes will benefit from the enhanced, 30-keV beam energy envisioned in the future setup.

6. Conclusion

For the first time, collinear laser spectroscopy has been applied in a MR-ToF device. This new technique, under development within the MIRACLS project at ISOLDE, CERN, offers the potential of improving conventional fluorescence-based CLS significantly by trapping ion bunches for multiple revolutions. While first steps are being taking in a PoP setup at CERN, simulations and preparations are already under way to design a device operating at 30 keV.

References

[1] K. Blaum, J. Dilling, W. Nörtershäuser, Precision atomic physics techniques for nuclear physics with radioactive beams, Phys. Scr. T152 (2013) 014017 .

[2] P. Campbell, I. Moore, M. Pearson, Laser spectroscopy for nuclear structure physics, Prog. Part. Nucl. Phys. 86 (2016) 127–180.

[3] R. Neugart, et al., Collinear laser spectroscopy at isolde: new methods and highlights, J. Phys. G: Nucl. Part. Phys. 44 (6) (2017) 064002 .

[4] R. Catherall, et al., The isolde facility, J. Phys. G: Nucl. Part. Phys. 44 (9) (2017) 094002 .

[5] C. Babcock, et al., Quadrupole moments of odd-a 5363mn: onset of collectivity towards n = 40, Phys. Lett. B 760 (2016) 387–392.

[6] M.J.G. Borge, B. Jonson, Isolde past, present and future, J. Phys. G: Nucl. Part. Phys. 44 (4) (2017) 044011 .

[7] H. Wollnik, M. Przewloka, Time-of-flight mass spectrometers with multiply reflected ion trajectories, Int. J. Mass Spectrom. Ion Processes 96 (3) (1990) 267–274.

[8] D. Zajfman, et al., Electrostatic bottle for long-time storage of fast ion beams, Phys. Rev. A 55 (Mar 1997) R1577–R1580.

[9] W.H. Benner, A gated electrostatic ion trap to repetitiously measure the charge and m/z of large electrospray ions, Anal. Chem. 69 (20) (1997) 4162–4168.

[10] W. Plaß, et al., Isobar separation by time-of-flight mass spectrometry for low-energy radioactive ion beam facilities, Nucl. Instrum. Methods Phys. Res. Sect. B 266 (19) (2008) 4560–4564 Proceedings of the XVth International Conference on Electromagnetic Isotope Separators and Techniques Related to their Applications.

[11] A. Piechaczek, et al., Development of a high resolution isobar separator for study of exotic decays, Nucl. Instrum. Methods Phys. Res. Sect. B 266 (19) (2008) 4510–4514 Proceedings of the XVth International Conference on Electromagnetic Isotope Separators and Techniques Related to their Applications.

[12] P. Schury, et al., Multi-reflection time-of-flight mass spectrograph for short-lived radioactive ions, Eur. Phys. J. A 42 (Oct 2009) 343.

[13] J.D. Alexander, et al., Short pulse laser-induced dissociation of vibrationally cold, trapped molecular ions, J. Phys. B: At. Mol. Opt. Phys. 42 (15) (2009) 154027 .

[14] M. Lange, et al., A cryogenic electrostatic trap for long-time storage of kev ion beams, Rev. Sci. Instrum. 81 (5) (2010) 055105 .

[15] R. Wolf, et al., On-line separation of short-lived nuclei by a multi-reflection time-of-flight device, Nucl. Instrum. Methods Phys. Res. Sect. A 686 (2012) 82–90.

[16] F. Wienholtz, et al., Masses of exotic calcium isotopes pin down nuclear forces, Nature 498 (Jun 2013).

[17] R.N. Wolf, et al., Isoltraps multi-reflection time-of-flight mass separator/spectrometer, Int. J. Mass Spectrom. 349 (2013) 123–133.

[18] F. Wienholtz, et al., Towards ultrahigh-resolution multi-reflection time-of-flight mass spectrometry at isoltrap, Phys. Scr. 2015 (T166) (2015) 014068 .

[19] T. Dickel, et al., Dynamical time focus shift in multiple-reflection time-of-flight mass spectrometers, Int. J. Mass Spectrom. 412 (2017) 1–7.

[20] C. Jesch, The mr-tof-ms isobar separator for the titan facility at triumf, TCP 2014, Springer International Publishing, 2017, pp. 175–184.

[21] S. Kaufman, High-resolution laser spectroscopy in fast beams, Opt. Commun. 17 (3) (1976) 309–312.

[22] M. Rosenbusch, et al., Towards systematic investigations of space-charge phenomena in multi-reflection ion traps, AIP Conf. Proc. 1521 (1) (2013) 53–62.

[23] L. Schweikhard, M. Rosenbusch, F. Wienholtz, R. Wolf, Isobar separation and precision mass spectrometry of short-lived nuclides with a multi-reflection time-of-flight analyzer, Proceedings of Science (PoS), 2014. Proceedings of the Xth Latin Am. Sym. Nucl. Phys. Appl., Montevideo, Uruguay.

[24] M. Rosenbusch, et al., Delayed bunching for multi-reflection time-of-flight mass separation, AIP Conf. Proc. 1668 (1) (2015) 050001 .

[25] F.M. Maier, et al., Simulations of a proof-of-principle experiment for collinear laser spectroscopy with a multi-reflection time-of-flight device, Accepted in Hyperfine interactions, 2019.

[26] T. Murböck, et al., A compact source for bunches of singly charged atomic ions, Rev. Sci. Instrum. 87 (4) (2016) 043302 .

[27] R.N. Wolf, G. Marx, M. Rosenbusch, L. Schweikhard, Static-mirror ion capture and time focusing for electrostatic ion-beam traps and multi-reflection time-of-flight mass analyzers by use of an in-trap potential lift, Int. J. Mass Spectrom. 313 (2012) 8–14.

[28] M. Rosenbusch, et al., Towards systematic investigations of space-charge phenomena in multi-reflection ion traps, AIP Conf. Proc. 1521 (1) (2013) 53–62.

[29] K. Kreim, et al., Nuclear charge radii of potassium isotopes beyond n=28, Phys. Lett. B 731 (2014) 97–102.

[30] F. Wienholtz, S. Kreim, M. Rosenbusch, L. Schweikhard, R. Wolf, Mass-selective ion ejection from multi-reflection time-of-flight devices via a pulsed in-trap lift, Int. J. Mass Spectrom. 421 (2017) 285–293.

[31] A. Nieminen, et al., On-line ion cooling and bunching for collinear laser spectroscopy, Phys. Rev. Lett. 88 (2002) 094801 .

[32] E. Mané, et al., An ion cooler-buncher for high-sensitivity collinear laser spectroscopy at isolde, Eur. Phys. J. A 42 (2009) 503–507.

[33] D. Manura, D. Dahl, Simion (r) 8.1 user manual, 2013.

[34] W. Ansbacher, Y. Li, E. Pinnington, Precision lifetime measurement for the 3p levels of mg ii using frequency-doubled laser radiation to excite a fast ion beam, Phys. Lett. A 139 (3) (1989) 165–169.

[35] F. Wienholtz, Private Communications, 2018.

[36] S. Lechner, et al., Fluorescence detection as a new diagnostics tool for electrostatic ion beam traps, Submitted to Hyperfine interactions, 2019.

[37] W. Nörtershäuser, et al., Nuclear charge radii of ^{7,9,10}Be and the one-neutron halo nucleus ^{11}Be, Phys. Rev. Lett. 102 (Feb 2009) 062503 .

[38] A. Krieger, et al., Frequency-comb referenced collinear laser spectroscopy of be+ for nuclear structure investigations and many-body qed tests, Appl. Phys. B 123 (Dec 2016) 15.

[39] P. Imgram, et al., Phys Rev A, (2019) (in print).

8 Peer-reviewed publications

2020

7. **"Doubly-magic character of ^{132}Sn studied via electromagnetic moments of ^{133}Sn"**
Rodríguez, L. V., Balabanski D. L., Bissell M. L., Blaum K., Cheal B., De Gregorio G., Ekman, J., Garcia Ruiz R. F., Gargano, A., Georgiev G. ,Gins W., Gorges C., Heylen H., Kanellakopoulos A., Kaufmann S., Lagaki V., Lechner S., Maaß B., Malbrunot-Ettenauer S., Neugart R., Neyens G., Nörtershäuser W., Sailer S., Sánchez R., Schmidt S., Wehner L., Wraith C., Xie L., Xu Z. Y., Yang, X. F. and Yordanov D. T.
Phys. Rev. C, 102, 051-301 (2020),
https://link.aps.org/doi/10.1103/PhysRevC.102.051301

6. **"Structural trends in atomic nuclei from laser spectroscopy of tin"**
Deyan T. Yordanov, Liss V.Rodríguez, Dimiter L., Balabanski, Jacek Bieroń, Mark L. Bissell, Klaus Blaum, Bradley Cheal, JörgenEkman, Gediminas Gaigalas, Ronald F. Garcia Ruiz, Georgi Georgiev, Wouter Gins, Michel R. Godefroid, Christian Gorges, Zoltán Harman, Hanne Heylen, Per Jönsson, Anastasios Kanellakopoulos, Simon Kaufmann, Christoph H. Keitel, Varvara Lagaki, Simon Lechner, Bernhard Maaß, Stephan Malbrunot-Ettenauer, Witold Nazarewicz, Rainer Neugart, Gerda Neyens, Wilfried Nörtershäuser, Natalia S. Oreshkina, Asimina Papoulia, Pekka Pyykkö, Paul-Gerhard Reinhard, Stefan Sailer, Rodolfo Sánchez, Sacha Schiffmann, Stefan Schmidt, Laura Wehner, Calvin Wraith, Liang Xie, Zhengyu Xu and Xiaofei Yang
Commun Phys 3, 107 (2020),
https://doi.org/10.1038/s42005-020-0348-9

5. **"Stray-light suppression for the MIRACLS proof-of-principle experiment"**
V. Lagaki, P. Fischer, H. Heylen, F.Hummer, S. Lechner, F. Maier, P. Plattner, Marco Rosenbusch, M. Rosenbusch, S. Sels, F. Wienholtz, R.N. Wolf, W. Nörtershäuser, L. Schweikhard, S. Malbrunot-Ettenauer
Acta Physica Polonica B, 51, 571-576 (2020),
https://www.actaphys.uj.edu.pl/fulltext?series=Regvol=51page=571

2019

4. **"Fluorescence detection as a new diagnostics tool for electrostatic ion beam traps"**
S. Lechner, P. Fischer, H. Heylen, V. Lagaki, F. M. Maier, P. Plattner, M. Rosenbusch, S. Sels, F. Wienholtz, R. N. Wolf, W. Nörtershäuser, L. Schweikhard, and S. Malbrunot-Ettenauer

Hyperfine Interact. 240, 95 (2019),
https://doi.org/10.1007/s10751-019-1628-1

3. **Simulations of a proof-of-principle experiment for collinear laser spectroscopy within a multi-reflection time-of-flight device**
F. M. Maier, P. Fischer, H. Heylen, V. Lagaki, S. Lechner, P. Plattner, S. Sels, F. Wienholtz, W. Nörtershäuser, L. Schweikhard, and S. Malbrunot-Ettenauer
Hyperfine Interact. 240, 54 (2019),
https://doi.org/10.1007/s10751-019-1575-x

2. **"First steps in the development of the Multi Ion Reflection Apparatus for Collinear Laser Spectroscopy"**
S. Sels, P. Fischer, H. Heylen, V. Lagaki , S. Lechner, F.M. Maier, P. Plattner, M. Rosenbusch, F. Wienholtz, R.N. Wolf, W. Nörtershäuser, L. Schweikhard, S. Malbrunot-Ettenauer
Nucl. Instr. Methods B, 463, 310-314 (2019),
https://doi.org/10.1016/j.nimb.2019.04.076

1. **"Laser spectroscopy of neutron-rich tin isotopes: A discontinuity in charge radii acrossthe N=82 shell closure"**
C. Gorges, L. V. Rodríguez, D. L. Balabanski, M. L. Bissel, K. Blaum, R. F. Garcia Ruiz, G. Georgiev, W. Gins, H. Heylen, T. Kanellakopoulos, S. Kaufmann, M. Kowalska, V. Lagaki, S. Lechner, B. Maass, S. Malbrunot-Ettenauer, W. Nazarewicz, R. Neugart, G. Neyens, W. Nörtershäuser, P.-G. Reinhard, S. Sailer, R. Sánchez, S. Schmidt, L. Wehner, C. Wraith, Z. Y. Xu, X.F. Yang and D. T. Yordanov
Phys. Rev. Lett. 122, 192-502 (2019),
https://doi.org/10.1103/PhysRevLett.122.192502

9 Acknowledgments

Foremost, I would like to express my sincere gratitude to my CERN supervisor Dr . Stephan Malbrunot-Ettenauer for giving me the opportunity to join an exciting project like MIRACLS and live the experience to be part of CERN, one of the largest nuclear research organization in the world. In addition, I would like to express my deep sense of thanks to him for his guidance at every stage of my Ph.D study and for all the knowledge that I gained from him regarding the experimental physics.

Besides my CERN supervisor, I would like to express my warm appreciation to Prof. Dr. Lutz Schweikhard for his continued help, support and advice whenever I needed it as well as for his helpful comments and suggestions to my manuscripts even within a single day.

Furthermore, I would like to thank the entire MIRACLS team for their help in the laboratory and to the entire collaboration, which I am glad to be a part of it. Especially, I would like to thank Peter Plattner for his great help in the last measurements for my Ph.D study that I performed alone due to the Covid-19 restrictions. Also, during my work at MIRACLS team, I had the chance to collaborate with Dr. Paul Fischer and I would like to express my thanks to him for his kind help and the nice cooperation that we had throughout my study period.

My special thanks go to my good friend Tassos for his unreserved and wholehearted support during my Ph.D period. Also, for his patience and understanding in moments that I really needed it. I am having a lot of happy memories with him during my physics journey. Thank you for everything!

My deepest gratitude goes to my family, who unconditionally support me in everything that I have done so far and especially their support to my big decision to move abroad in order to fulfill my dreams.

Last but not least, my most precious thank you goes to the most special person in my life - my beloved fiancé Manolis. This journey would not be possible without his support, his endlessness energy and enthusiasm which were giving me motivation to continue. You helped me to develop myself. *Σε ευχαριστω για την στηριξη σου ολα αυτα τα χρονια*!